FULL WAVE SYNTHETIC ACOUSTIC LOGS IN SATURATED POROUS MEDIA PART II: SIMPLE CONFIGURATION

by

D.P. Schmitt

Earth Resources Laboratory
Department of Earth, Atmospheric, and Planetary Sciences
Massachusetts Institute of Technology
Cambridge, MA 02139

Abstract

The discrete wavenumber method is used to compute synthetic full waveform acoustic logs in an axisymmetric fluid-filled borehole surrounded by a porous medium. The two phase formation is modeled following Biot's theory. It is modified by the introduction of an unified definition of the coupling coefficients related to the pore shape in accordance with homogenization theory. Both permeable and impermeable borehole walls are considered. The study focuses on the permeabilty, source center frequency and radius effects on guided modes and especially the Stoneley wave for various types of formations and saturant fluids. Comparison is made with homogeneous elastic formations. Plots of the spectral energy density in the frequency axial wavenumber domain allow the recognition and identification of the different wave types.

When the pores are occluded at the borehole wall, the wavefield behavior is nearly equivalent to that of an elastic formation (with body wave attenuation added). The Stoneley wave is only very slightly affected.

When the fluid flow is free, the distortions are more important because of the relative motion between the two phases at the borehole wall. With increasing permeability, Stoneley wave absolute and relative energy decreases and is relegated to a narrower low frequency band. It is then associated with a phase velocity lower than the "tube" wave velocity in an elastic formation. Its dispersion increases, especially in the low frequency range. Its attenuation correspondingly increases, reinforced by an increase of the shear wave attenuation. Due to an apparent increase of the borehole radius, the low cut-off frequencies of the pseudo-Rayleigh modes are shifted toward lower frequencies. The P to guided wave amplitude ratio is enhanced. For a given permeability, porosity and pore geometry, these characteristics are enhanced when the saturant fluid mobility increases and/or when the borehole radius decreases.

INTRODUCTION

There are at least two ways to model two phase media:

- a solid elastic matrix with randomly distributed occluded pores which are partially or completely saturated, and
- a solid elastic matrix with open pores or cracks saturated with fluid and interconnected so that the liquid phase is continuous.

In fact, real rocks include these two types of models. Numerous theoretical formulations have been developed to study these complex lithologies. They all assume that the seismic wavelength is long compared to the characteristic pore dimension but differ on the model implemented.

Laboratory experiments have shown qualitative relationships between the P and S wave velocity ratio (α / β) and lithology. The aim is then to solve the inverse problem: knowing this ratio (or, equivalently, the travel time ratio in a given stratigraphic unit) obtain a lithologic identification of the rocks. The velocities must then be corrected for the effects of parameters such as saturation conditions, saturant fluid and pore geometry. The most quoted formulation has been developed by Kuster and Toksöz (1974 a, b), Toksöz et al. (1976) and Cheng and Toksöz (1978) and is usually referred to as the Toksöz et al. model. The aggregate is composed of a solid elastic matrix with ellipsoidal inclusions characterized by only one parameter, the aspect ratio, which is the length of the minor axis divided by that of the major axis. Based on diffraction theory, it relates the effective elastic coefficients and the seismic velocities to the elastic parameters of the matrix and inclusions. Multiple diffraction being neglected, the model is limited to media where the pore concentration is not too high. The main results are:

- Although making up a small fraction of the porosity, the thin pores strongly affect the elastic modulii and the velocities (this is because their surface is large compared to their volume),
- A rise in pressure can be quantified: the thin pores rapidly close in contrast to the larger ones,
- The effects of the clay content can be analyzed.

With a similar goal in mind, Mavko and Nur (1978) have studied the possible effects of cracks. Winkler and Nur (1982) have analyzed the effects of frictional sliding. For a more complete discussion, the reader is referred to Tatham (1982).

The second approach, which is the main concern of this paper, allows the calculation of the total wavefield. The porous formations are modeled following Biot's theory as

described in Part I. The presence of the compressional wave of the second kind modifies the wavefield. At any kind of interface (fluid-porous, elastic-porous and porous-porous), supplementary phenomena will then occur when the waves are transmitted or reflected.

The studies essentially split into two categories: body wave (transmission and reflection) or surface and interface waves (dispersion and attenuation). Rasolofossaon (1984) presented a bibliographic study of the different works initiated by Deresiewickz around the sixties. Whatever the waves are, the greatest variations occur when the porous formations are permeable (Dutta and Odé, 1983; Rasolofossaon, 1984; Bonnet 1985 for example). In the presence of a free surface, modifications of the surface wave dispersion characteristics are strongly dependent upon the critical frequency value (Boutin, 1983; Pal, 1983).

At the present time few synthetic records have been calculated. Rosenbaum (1974) considered the situation of a plane fluid-porous interface and also the well logging configuration. He showed a correlation between the formation permeability and the Stoneley wave attenuation when the formation is permeable. However, the source spectrum used is too wide band and too high frequency for the synthetic microseismograms to correspond to real data. White (1983) and Mathieu (1984) also analyzed Stoneley wave characteristics as a function of the permeability and fracture degree of a formation. Their studies refer to the low frequency domain and the Stoneley wave is considered as a plane wave. On the other hand, Feng and Johnson (1983a, b) considered the situation of a plane fluid-porous interface when all three body waves are propagative (i.e., at very high frequencies). Depending on the permeable character of the formation, they pointed out the existence of a pseudo-Stoneley mode related to the slow compressional P_2 wave. Their results have been recently confirmed by laboratory experiments (Mayes et al., 1986). Cheng et al. (this issue) computed Stoneley wave dispersion curves in the well logging configuration.

In the present study, the theoretical formulation of two phase media as described in Part I is first presented applied to an axisymmetric configuration. After writing the continuity equations at the interface, either permeable or impermeable, between the borehole fluid and the porous formation, synthetic microseismograms are computed using the discrete wavenumber method. Frequency axial wavenumber analysis of the radiated wavefield is simultaneously performed. The study focuses on the permeability effects, especially on Stoneley wave characteristics, as a function of the saturant fluid, the source center frequency, the borehole radius, the porosity and the velocities of the formation.

THEORY

In a cylindrical coordinate system (r,θ,z), an axisymmetric fluid-filled borehole extending to infinity in the z direction is considered. The surrounding porous medium is radially semi-infinite. (u, w) and (σ , τ) will denote the radial and tangential components of the displacement $\vec{u}$ and of the stress (traction) vector $\vec{\sigma}$ in the solid phase. $\tilde{\phi}$ is the porosity, U the radial component of the displacement $\vec{U}$ in the liquid phase and s the tension in the liquid phase which is related to the pressure p in the pore fluid by $s = -\tilde{\phi}p$.

Subscripts 1 and 2 will denote the bore fluid and the porous medium, respectively. The scalar potentials Φ (and associated quantities) relative to the compressional waves of the first and second kind (see Part I) will be distinguished by supplementary subscripts 1 and 2.

Because of the axial symmetry, only the azimuthal component of the vector potential $\vec{\Psi}$ is non zero. The potentials verify Helmholtz type equations (see equ. (54), (57) and (58) of Part I). Particular solutions are then similar to those of the elastic case, i.e.:

$$\begin{cases} \Phi_{jl} &= \{\Gamma_{jl} I_0(kp_{jl}\, r) + B_{jl} K_0(kp_{jl}\, r)\}\ e^{i(kz+\omega t)} \quad l=1,2 \\ \Psi_2 &= \{C\, I_1(ks_2\, r) + D_2\, K_1(ks_2\, r)\}\ e^{i(kz+\omega t)} \end{cases} \tag{1}$$

where

- I_n and K_n are,respectively, the modified Bessel functions of the first and second kind of the n-th order,
- $kp_{jl}^2 = k^2 - \omega^2/\alpha_{jl}^2$
- $ks_2^2 = k^2 - \omega^2/\beta_2^2$
  are the radial wavenumbers relative to the compressional and shear waves whose velocities are α_{jl} and β_2.
- Γ_{jl}, B_{jl}, C_2 and D_2 are functions of the axial wavenumber k and the angular frequency ω.

The general solutions can be expressed as a double integral of the solutions (1) over k and ω.

The radiation conditions specify that the potentials have to remain finite when:

- r tends to infinity, so that $\Gamma_{21} = \Gamma_{22} = C_2 = 0$ for the porous medium,
- r tends to zero, so that $B_1 = 0$ for the bore fluid.

The expressions of the stress and displacements of a porous medium deduced from the equations (15) and (59) of Part I, may be written in a cylindrical coordinate system:

$$\begin{cases} u_2 = \sum_{l=1}^{2} \frac{\partial \Phi_{2l}}{\partial r} - \frac{\partial \Psi_2}{\partial z} \\ w_2 = \sum_{l=1}^{2} \frac{\partial \Phi_{2l}}{\partial z} + \frac{1}{r}\Psi_2 + \frac{\partial \Psi_2}{\partial r} \\ U_2 = \sum_{l=1}^{2} \xi_{2l} \frac{\partial \Phi_{2l}}{\partial r} - \chi_2 \frac{\partial \Psi_2}{\partial r} \\ p_2 = -\frac{1}{\tilde{\phi}_2} s_2 = \sum_{l=1}^{2} \left[\frac{\omega^2}{\tilde{\phi}_2 \alpha_{2l}^2} (Q_2 + \tilde{R}_2 \xi_{2l}) \Phi_{2l} \right] \\ \sigma_2 + s_2 = 2N_2 \left[\sum_{l=1}^{2} \frac{\partial^2 \Phi_{2l}}{\partial r^2} - \frac{\partial^2 \Psi_2}{\partial r \partial z} \right] - \sum_{l=1}^{2} \frac{\omega^2}{\alpha_{2l}^2} \left\{ A_2 + Q_2 + (Q_2 + \tilde{R}_2) \xi_{2l} \right\} \Phi_{2l} \\ \tau_2 = -\frac{\omega^2}{\beta_2^2} N_2 \Psi_2 + 2N_2 \left[\sum_{l=1}^{2} \frac{\partial^2 \Phi_{2l}}{\partial r \partial z} - \frac{\partial^2 \Psi_2}{\partial z^2} \right] \end{cases} \tag{2}$$

where

- A_2, N_2, Q_2, $\tilde{R}_2$ are the elastic coefficients of the porous medium (see equation (16) of Part I). They are complex and frequency dependent if intrinsic attenuation is taken into account.
- ξ_{2l} and χ_2 are complex frequency dependent factors which characterize the influence of one phase on the other due to dynamic and viscous forces (see equations (56) and (57) of Part I, respectively).

In the case of a permeable interface, the continuity equations at the borehole wall (i.e., at $r = R$) are:

$$\begin{cases} 1) \quad U_1 = u_2 + \tilde{\phi}_2 (U_2 - u_2) \\ 2) \quad \sigma_1 = \sigma_2 + s_2 \\ 3) \quad 0 = \tau_2 \\ 4) \quad p_1 = p_2 \end{cases} \tag{3}$$

The first equation ensures the balance of the fluid volume. These equations may be obtained through the general principles of mechanics applied to the porous medium considered as a mixture (Truesdell and Toupin, 1960, see Part I). The continuity of the fluid pressure has been shown using homogenization theory (Auriault, 1985, personal communication). As a matter of fact, the system (3) is identical to the ones used by Rosenbaum (1974) and Feng and Johnson (1983a, b).

In the case of an impermeable interface, there is no relative motion between the two phases at the borehole wall. Thus, the fluid pressure is not continuous. The equations are:

$$\begin{cases} 1) & U_1 = u_2 \\ 2) & \sigma_1 = \sigma_2 + s_2 \\ 3) & 0 = \tau_2 \\ 4) & U_2 = u_2 \end{cases} \tag{4}$$

This system of equations corresponds to those obtained by Rosenbaum (1974) with an infinite resistance factor (see Part I). It corresponds to the presence of a zero thickness elastic layer close to the borehole wall. It does not mimic the effects related to the presence of a mudcake whose properties are almost unknown (see Schmitt, 1985 for discussion).

Considering a point source located at the origin of the axis, the systems to be solved deduced from equations (2), (3) and (4) may be written in a matrix form, respectively:

$$\underline{\mathbf{M}}^{(1)}\,\underline{N}^{(1)} = \underline{P}^{(1)} \tag{5}$$

$$\underline{\mathbf{M}}^{(2)}\,\underline{N}^{(2)} = \underline{P}^{(2)} \tag{6}$$

where

- $\underline{\mathbf{M}}^{(1)}$ and $\underline{\mathbf{M}}^{(2)}$ are 4x4 complex matrices whose elements are given in Appendix A,
- $\underline{N}^{(1)} = \underline{N}^{(2)} = (\Gamma_1, , B_{21}, B_{22}, D_2)^T$
- $\underline{P}^{(1)} = (-u_s, -\sigma_s, 0, -\sigma_s)^T$
- $\underline{P}^{(2)} = (-u_s, -\sigma_s, 0, 0)^T$

u_s and σ_s are the displacement and the stress radiated by the source at the borehole wall (i.e., at r = R):

$$u_s = -kp_1\,K_0(kp_1\,R)e^{i(kz+\omega t)}\,;\quad \sigma_s = -\rho_1\omega^2 K_0(kp_1\,R)e^{i(kz+\omega t)}$$

The total pressure in the borehole, which corresponds to the sum of the source term and the scattered wavefield, is, in both cases, given by:

$$P(r,z,t) = \int_{-\infty}^{+\infty}\int_{-\infty}^{-\infty} \{K_0(kp_1\,r) + \Gamma_1 I_0(kp_1\,r)\}\,S(\omega)\,e^{ikz}\,e^{i\omega t}\,dk\,d\omega \tag{7}$$

where

- $S(\omega)$ denotes the source spectrum,

- $K_0(kp_1\, r)$ is the source contribution.

From the theoretical point of view, it has to be noted that the scattered (reflected) wavefields exhibit a branch cut related to the bore fluid velocity. Similarly to the elastic case (Kurkjian, 1985), this fluid branch cut precisely cancels the direct arrival from the source, whatever the boundary conditions (Schmitt, 1985).

The integration is performed using the discrete wavenumber method (Bouchon and Aki, 1977; Cheng and Toksoz, 1981; Tubman et al., 1984; Schmitt and Bouchon, 1985). The compressional wave of the second kind cannot be critically refracted at the borehole wall. It is associated with a low phase velocity and it is inhomogeneous in most of the cases studied. Compared to the other body waves, it may then not correspond to a branch point located on the real wavenumber axis, especially at low frequencies. In the frequency axial wavenumber domain, its energy is then not localized around its phase velocity. It is "diffuse", distributed over a wide range of wavenumber values for a given frequency.

NUMERICAL EXAMPLES

In order to analyze the effects of the various parameters, the microseismograms obtained in the porous cases will be compared with those relative to an "equivalent" elastic formation. Its velocities are equal to those of the porous media in the low frequency range (see Part I). Its density ρ_2 is equal to:

$$\rho_2 = \rho^{(1)} + \rho^{(2)} = (1 - \tilde{\phi}_2)\rho_s + \tilde{\phi}_2\rho_f \tag{8}$$

where ρ_s and ρ_f are the intrinsic densities of the constitutive grains and of the saturant fluid.

The zero frequency limit of the Stoneley wave phase velocity in the presence of such a radially semi-infinite elastic formation is (using the zero frequency limit of the shear wave, see Part I):

$$\lim_{\omega \to 0} c_{ST} = \alpha_1 \left(1 + \frac{\rho_1 \alpha_1^2}{(1 - \tilde{\phi}_2)\rho_s \beta_m^2}\right)^{-\frac{1}{2}} \tag{9}$$

where β_m is the dry rock shear wave velocity.
For given constitutive grains and porosity, the zero frequency limit of the Stoneley wave phase velocity is then independent of the saturant fluid. This property is still valid in the presence of a rigid tool or a given elastic tool (Schmitt, 1985).

All the microseismograms are evaluated in the frequency range [0.- 21.] kHz and are computed at 256 points in time. The source waveform is a non-zero phase Ricker wavelet whose center frequency is denoted by f_s. Each wavetrain is normalized with respect to its own maximum. The scaling coefficient at the upper left gives the relative value compared to the maximum of the whole series denoted by 1.00. For a given source center frequency, the axial attenuation will be quantified by the variations of the maxima of amplitude. Although Kurkjian (1985), using the pole and branch cut contribution process, stated that the shear wave events are pseudo-Rayleigh (trapped) mode contributions near cut-off frequency, the term shear wave will be used in the following. It will refer to energy radiated in the borehole which propagates with the shear wave velocity. For elastic formations, nearly no energy is carried out by the pseudo-Rayleigh modes close to their cut-off frequency (Schmitt and Bouchon, 1985). They are then believed to belong to two different phenomena.

The spectral energy density calculations are performed with 64 frequencies ranging from 0. to 31.5 kHZ. The axial wavenumber step is the same ($2\ \pi\ /\ 10\ \mathrm{m}^{-1}$) regardless of the formation. Each diagram is normalized with respect to its own maximum (given by max), the zero frequency being omitted. Because the source term $K_0(kp_1\, r)$ becomes infinite at r = 0, the diagrams at the borehole center represent the scattered wavefield only. At the borehole wall, the source term is included and the diagrams display the total wavefield. ST denotes the Stoneley wave and PR_i the pseudo-Rayleigh modes. P and S indicate the refracted body waves and W the bore fluid velocity. As in Part I, the

pores are modeled as cylindrical ducts with a undirectional flow. The critical frequency for which the viscous and inertial forces are of the same order of magnitude is then given by:

$$f_{ci} = \frac{3}{4} \frac{\eta \tilde{\phi}}{2\pi \tilde{k} \rho_f}$$

Tables 1 and 2 give the physical parameters of the formations and saturant fluids used in this study. Table 3 presents the parameters of the equivalent elastic formations.

Permeability and saturant fluid effects

The formation used throughout this section is a Berea sandstone whose physical parameters are taken from Rosenbaum (1974) (see Table 1). The porosity is equal to 19%. Successive permeability values equal to 2 md, 32.5 md, 200 md, 500md, 1 darcy and 1.5 darcy are considered. The coupling coefficients as well as the body wave velocities and attenuations are then shown by the Figures (4a, b, c, d) and (5a, b, c, d) of Part I in the cases of water and gas saturation, respectively.

The borehole radius is taken to be 12 cm, the borehole fluid being water. No intrinsic attenuation is taken into account. The microseismograms are compared for a fixed offset of 5.25 m unless specified otherwise. The permeability increases from the top to the bottom, the case (1) corresponding to the elastic case.

A permeability increase emphasizes the two phase behavior of the porous medium. The critical frequency decreases as well as the static value of the viscous coupling coefficient. At the same time, the saturant fluid mobility ($\tilde{k}/\eta$) and the pore radius increase. The low frequency range velocities of the P_1 and S waves remain unchanged. Only their attenuation and dispersion are affected. These are shifted toward lower frequencies relative to the critical frequency. Attenuation thus increases only in the low frequency range relative to the highest permeability.

Impermeable borehole wall

Water saturation

Figures 1 and 2 show the wavetrains obtained at the center and at the wall of the borehole when the saturant fluid is water. The dispersion of the P_1 and S wave velocities is relatively weak. It can barely be detected.

The increase of low frequency shear wave attenuation with permeability is emphasized, whatever the source center frequency is, by:

- a continuous decrease of the maxima of amplitude,

- a continuous evolution of the microseismograms' internal dynamics. The relative amplitude of the low and high frequency components of the pseudo-Rayleigh wave decreases compared to the Stoneley wave pulse. At the opposite, the relative amplitude of the P wave and associated leaky modes increases compared to the entire wavetrain.

The axial attenuation curves (Figures 3 A,B) illustrate these observations: the higher the center source frequency, the greater the axial attenuation. This is because more energy relative to the pseudo-Rayleigh modes is taken into account. The Stoneley wave is little affected. The Figures 4 A, B show the spectral energy density diagrams relative to the elastic (A) case and to the permeability of 200 md (B), at the center of the borehole. As previously indicated, one can notice for the porous case a slight decrease of energy for each pseudo-Rayleigh mode, especially in the high frequency range (the critical frequency is equal to 114.9 kHz). On the other hand, the low frequency Stoneley wave energy remains almost unchanged, as well as its phase and group velocities. This corresponds to the attenuation variations of the S wave. Furthermore, the proper resonances of the borehole which lead to the excitation of the pseudo-Rayleigh modes (Schmitt and Bouchon, 1985) occur at the same frequency and present the same sharpness.

Gas saturation

In the gas saturation situation, the shape of the wavetrains obtained at the center of the borehole with a 7.5 kHz source center frequency (Figure 5) present very little difference from one another. The shear wave attenuation is less than in the presence of water. Nearly no internal dynamics changes can be noticed. The amplitude maxima decrease continuously, inversely proportional to the permeability, only up to 200 md. Beyond this value, they increase again. This phenomenon emphasizes the importance of the critical frequency. It is equal to 7.23 kHz, 3.62 kHz and 2.41 kHz for the permeabilities 500 md, 1.0 darcy and 1.5 darcy, respectively. Thus, for the high frequency energies relative to the pseudo-Rayleigh modes, the shear wave attenuations vary proportionally to $f^{-\frac{1}{2}}$ and $f^{\frac{1}{2}}$ instead of f and f^2, respectively. This is the same for the P_1 wave.

When the source center frequency is equal to 2.5 kHz, on the contrary, the maxima continuously decrease. Little energy relative to the pseudo-Rayleigh modes is taken into account, so that the wavetrains show the increasing distribution of the P_1 and S wave attenuations in the "low" frequency range. The same phenomenon can be observed at the borehole wall (Figure 6). The variations of the maxima of amplitude (Figure 7) show that the attenuation is rather weak. In the spectral domain (Figure 8 B, where k = 200 md), the high frequency energy is very little affected.

The comparison with the water saturation case emphasizes the effect of Poisson's ratio as in elastic formations (Cheng and Toksöz, 1981). Whatever the radial position of

observation is, the relative and absolute amplitude of the P wave and associated leaky modes is less for gas than for water because Poisson's ratio is lower (the difference of attenuation being taken into account).

These examples show that in the presence of an impermeable borehole wall, the reliability of the permeability determination may strongly depend upon the source center frequency. This is because of the critical frequency of the porous medium. The Stoneley wave, which is the principal component of the low frequency microseismograms, is then a more stable criterion. It has to be mentioned that in such a situation, the intrinsic attenuations of both the bore fluid and the matrix may, however, supersede the attenuation due only to the permeability.

Permeable borehole wall

Water saturation

The evolution of the waveforms in water saturated sandstone at the borehole center (Figure 9) is quite different from the impermeable wall situation. The decrease of the maxima is greater. This is especially true at the borehole wall where the Stoneley wave is predominant (Figure 10). With a 7.5 kHz source center frequency, as the permeabilty increases:

- The Stoneley wave relative amplitude decreases compared to the low frequency part of the pseudo-Rayleigh wave,
- The Airy phase is strongly reduced,
- The P wave and associated leaky modes increase in relative amplitude.

When the source center frequency is equal to 2.5 kHz, the Stoneley wave pulse has a much longer period for the highest permeabilities. Its attenuation increases and it exhibits a slight time delay.

In addition to the body wave attenuations, the second physical phenomenon involved is the fluid flow which takes place at the interface. It is related to the relative movement between the two phases. It increases with the permeability as the critical frequency decreases and the pore radius increases. Correlatively, the slow P_2 wave is less attenuated. The distribution of the energy transmitted to the three body waves of the porous medium is modified. For instance, the energy transmitted to the slow P_2 wave is more important than in the sealed pores case as this wave is associated with an out of phase motion between the two phases (Biot, 1956a, b). Its energy may, however, be not entirely utilized in the coupling phenomenon which leads to the Stoneley wave generation. It depends on the critical frequency value.

The behavior of the total wavefield is emphasized in the spectral domain. The frequency axial wavenumber diagrams relative to the 200 md and 1 darcy permeabilities obtained at the center of the borehole are displayed in Figures 11 A, B. Compared to the elastic and sealed pore cases (Figures 4 A,B), and with increasing permeability, Stoneley wave absolute energy decreases and is relegated to a narrower low frequency band. In addition, it is associated with a gradually lowered phase velocity. For example, it is equal to 1354 m/s and 1260 m/s at 500 Hz for the 2 md and 1.5 d permeabilities. (The "tube" wave velocity (equation (9)) is equal to 1357 m/s). At 2.5 kHz these are equal to 1350 m/s and 1337 m/s, respectively, decreasing the difference. Thus, the dispersion increases with permeability especially in the low frequency range. This result is also shown by Burns and Cheng (this issue) and may be somewhat surprising. Simply, it comes from the fact that the interface wave energy is concentrated in the low frequency domain.

As a result of the flow, the borehole wall is less rigid. The shear wave is then more attenuated. It becomes more inhomogeneous in the sense that the difference between the equiphase and equiamplitude planes increases. The proper resonances are then smoother. The flow also leads to an apparent increase of the borehole radius. The resonances and associated low cut-off frequencies of the pseudo-Rayleigh modes are thus slightly shifted toward lower frequencies. This explains the "stagnation" of the maxima of amplitude curves with larger offsets (Figure 12).

Introducing attenuation in the matrix and/or in the borehole fluid using Q values (equations (16), (17) and (18) of Part I) will result in a greater Stoneley wave attenuation (Schmitt, 1985; Burns and Cheng, this issue). The examples displayed by Figure 13 ($\tilde{k}$ = 1 darcy, for Q values see Table 4), show that the energy dissipation mechanisms are superimposed. Stoneley wave dispersion remains unchanged. The reliability of the permeability determination then needs measurements of both the (phase) velocity and the attenuation of the Stoneley wave, and preferably in the low frequency range.

Gas saturation

Compared to water, gas has a very low viscosity and is very compressible, (see Table 2), which results in a high mobility ($\tilde{k}/\eta$). The flow phenomenon is then reinforced by the difference in the mobility of the two fluids present. This allows the borehole fluid to drive the gas efficiently. The spectral energy density diagrams obtained at the center of the borehole with permeabilities equal to 2 md (A), 32.5 md (B), 200 md (C) and 1 darcy (D) (Figure 14) clearly show the results of such an enhancement of the fluid flow. Compared to the elastic case (Figure 8), even for the lowest permeability despite a high critical frequency value (= 1808 kHz):

- The Stoneley wave exhibits less energy which is relegated to a narrower low frequency band. It corresponds to a phase velocity lower than the "tube" wave

velocity (TU_{ST}) whatever the permeability is, contrary to the water saturation case. When $\tilde{k} = 2$ md, it is equal to 90% TU_{ST} at 500 Hz.

- The proper resonances of the borehole and the associated low cut-off frequencies of the pseudo-Rayleigh modes are shifted toward lower frequencies. Considering that for a given borehole fluid and formation the ratio $f_c R/\alpha_1$ (where f_c is the cut-off frequency) is a constant, the apparent radii in the four cases are successively equal to 13, 15, 17 and 21 cm.
- The energy ratio between the pseudo-Rayleigh modes and the Stoneley wave grows considerably. This explains the apparent sharpness of the resonances.

In spite of these modifications, the general dispersion characteristics of the wavefields remain unchanged. The Stoneley wave exhibits a reverse dispersion with phase velocity converging to the bore fluid velocity. However, it is more pronounced in the low frequency range (see Figure 15A where the calculation has been performed in the frequency range [0.- 5.5] kHz with an axial wavenumber step ten times smaller than usual. $\tilde{k} = 200$ md.). The pseudo-Rayleigh modes are highly dispersive. Their phase velocities range from the porous formation shear wave velocity to the bore fluid velocity (W). Furthermore, as in the elastic case, the Stoneley wave amplitude increases from the center to the wall of the borehole. The reverse situation occurs, in an oscillatory manner, for the pseudo-Rayleigh modes (see Figure 15 B where $r = R$ and $\tilde{k} = 200$ md).

The high source center frequency microseismograms (Figures 16, 17) bear little resemblance to those of the corresponding elastic and sealed pore cases. The Stoneley wave cannot be picked. This is true even at the borehole wall where the maxima of amplitude are much less than at the center, in contrast to the elastic case. The evolution of the waveforms essentially represents the shift toward lower frequencies of the low cut-off frequencies of the pseudo-Rayleigh modes. It is only for a low source center frequency that the Stoneley wave can be detected, and only for low permeability values. It exhibits a time delay corresponding to a phase velocity of 1329 m/s and a small amplitude (see also the evolution of the maxima of amplitude, Figure 18). This is because its phase velocity is so much reduced that the time window is too short for this offset when the permeability increases. Figures 19 and 20 present the microseismograms relative to a 1.25 m distance. Even with such a short spacing, the Stoneley wave pulse is detectable only at the borehole wall. Again, it exhibits a long period and a large time delay for the highest permeabilities.

For equal porosity and close mobilities ($\tilde{k}/\eta$), the comparison between the water saturation (with $\tilde{k} = 1.5$ d) and the gas saturation (with $\tilde{k} = 32.5$ md) situations emphasizes the importance of the saturant fluid compressibility, despite the difference in the mass coupling coefficients.

Gaseous water saturation

The presence of saturant fluids resulting from liquid-gas mixtures will lead to wavefields for wich the modifications will be mostly due (in frequency bands where the porous medium behavior is equivalent to the one with homogeneous fluids) to:

- the shear wave attenuation when the pores are sealed (occluded),
- the saturant fluid mobility when the fluid flow is free. The effects will be all the more pronounced that the bore fluid will be able to drive the saturant fluid.

Only the straightforward consequence of a partial gas saturation, namely, a decrease in the fluid velocity, is considered. Furthermore, in order to emphasize the saturant fluid compressibility effects, the gaseous water taken into account has a velocity equal to 800 ms^{-1}, all other parameters being equal in other respects (see Table 2).

The P_1 and P_2 wave velocities of the porous sandstones are lower compared to the pure water saturation case. On the other hand, the density and the shear wave velocity remain unchanged (see Figures 3 of Part I).

The microseismograms obtained with permeability values equal to 200 md and 1 darcy at the center of the borehole are displayed on Figure 21. Only the open pore situation is presented and compared with the pure water saturation case. Despite a Poisson's ratio decrease and a greater P_1 wave attenuation, the relative amplitude of the P-wave and associated leaky modes is of the same order of magnitude for both saturant fluids. The shear wave attenuation is identical in both cases, this is due to the Stoneley wave behavior. The spectral energy densities evaluated at the center of the borehole (Figure 22) clearly point out that its energy is weaker and contained in a narrower frequency band (see Figure 12). Its phase velocity is also reduced although to a small extent. At 500 Hz, it is equal to 96% of the pure water saturation case when $\tilde{k} = 1$d. The apparent increase in the borehole radius, although small, is more important. With 1 darcy permeability, the relative and absolute energy of each pseudo-Rayleigh mode is less than in the presence of pure water. These results emphasize the permeability and saturant fluid compressibility effects on the coupling phenomena which generate the Stoneley wave and the pseudo-Rayleigh modes.

Oil saturation

Just as the compressibility, the viscosity of the saturant fluid is an important parameter. It directly affects the viscous coupling coefficient and the mobility of the liquid. For a given permeability and porosity, the higher the viscosity, the higher the critical frequency. This result is shown by considering a heavy oil saturation case (i.e. $\eta = 180$ cp. See Figures 2 of Part I).

In this example, the permeability and the porosity are respectively equal to 200 md and 19 %. The critical frequency is then equal to 23.520 MHz. Figure 23 displays the synthetic microseismograms obtained at the center (at the wall) of the borehole. The numbers 1, 2, 3 (4, 5, 6) refer to the "equivalent" elastic formation, the porous formation with an impermeable borehole wall and with a permeable wall respectively.

Whatever the source center frequency and the radial position of observation, the wavetrains are nearly identical. Only a slight global scale change can be noticed. This is confirmed by the variations of the maxima of amplitude with spacing (Figure 24). The free fluid flow leads only to a global shift downward of the curves. In the spectral domain (Figure 25), the repartition of energy among the different wave types is practically identical for the elastic and permeable formations (the difference does not exceed 1 %). In addition, as well as in the sealed pores case, the proper resonances of the borehole occur at the same frequencies and exhibit the same sharpness.

The mobility of heavy oil is too small for any significant fluid flow to take place at the interface whatever the permeability.

Permeability and radius effects

A decrease in the borehole radius leads to an increase of the energy incident on the borehole wall and to a variation of the "apparent" curvature for the source.

In an elastic formation, this results in an increase in Stoneley wave energy. Its "useful" part is also contained in a broader frequency band. At the same time, the proper resonances of the borehole and associated low cut-off frequencies of each pseudo-Rayleigh mode are shifted toward higher frequencies (Cheng and Toksöz, 1981; Schmitt and Bouchon, 1985). Finally, the absolute amplitudes of the P and S waves decrease (Zhang and Cheng, 1984).

In the following, the borehole radius is equal to 7cm. The formation is still the Berea sandstone (Table 1). No intrinsic attenuation is taken into account.

Water saturation

The comparison is made between the elastic case and porous formations whose permeabilities are equal to 200 md and 1 darcy.

When the pores are sealed (Figure 26), the differences between the wavetrains are the same as for a larger radius, although more pronounced (Figures 1 and 2). In the spectral domain (Figure 27, where $\tilde{k} = 200$ md), only the high frequency shear wave attenuation is characterized. It explains the decrease of the pseudo-Rayleigh wavetrain amplitude.

In the case of a free fluid flow at the borehole wall (Figure 28), the modifications of wavetrains due to a reduced radius are important but of varied kinds. Whatever the source center frequency is, the maxima of amplitude are strongly reduced. This corresponds to a greater axial attenuation (Figure 29, where 2, 3 and 4, 5 are respectively relative to the impermeable and permeable interface. Compare with Figures 3 and 11). This variation leads to a new distribution of the relative amplitudes. The P wave and associated leaky modes, as well as the low frequency part of the pseudo-Rayleigh wave, are much more developed when the "shear" arrival is weaker. In addition *the Stoneley wave is more attenuated and exhibits a greater time delay than previously.*

In the spectral domain (Figure 30. $\tilde{k} = 200$ md), Stoneley wave absolute energy is less, compared to the elastic case, than when $R = 12$ cm (84 % instead of 90 %). At the same time, it is relegated to a narrower low frequency band and associated with a phase velocity lowered all the more that the permeability is high. For example, when $\tilde{k} = 1$ d, the ratio of the phase velocities relative to the small and large radii increases from 95.5% to 97.5% in the frequency range [0.5,2.5] kHz. On the other hand, it is almost constant and equal to 98% when $\tilde{k} = 200$ md. Despite this behavior, the relative shift of the resonances related to only the borehole radius decrease is nearly the same as that for the elastic formation. According to this criterion, the fluid flow at the borehole wall is only slightly enhanced but the dissipated energy is much greater.

In order to get more insight into this complex phenomenon, the radial behavior of the wavefield is analyzed when $\tilde{k} = 200$ md. Whatever the borehole radius R is (12 cm or 7 cm), the same relative radial positions of observation are considered and the following "functions" have been computed:

1) $P_1(r = 0)$
2) $P_1(r = R)$
3) $-\{\sigma_2(r = R) + s_2(r = R)\}$
4) $-\{\sigma_2(r = R + 6\,\text{cm}) + s_2(r = R + 6\,\text{cm})\}$
5) $-\{\sigma_2(r = R + 12\,\text{cm}) + s_2(r = R + 12\,\text{cm})\}$
6) $-s_2(r = R)/\tilde{\phi}_2$
7) $-s_2(r = R + 6\,\text{cm})/\tilde{\phi}_2$
8) $-s_2(r = R + 12\,\text{cm})/\tilde{\phi}_2$

Those calculations will also emphasize the influence of the continuity equations (cf. equations (3) and (4)) on the saturant fluid pressure.

The results obtained with the impermeable interface are displayed by the Figures 31 and 32 for $R = 12$ cm and $R = 7$ cm respectively. The radial evolution of the porous medium total stress wavetrain shape corresponds to that which may be obtained with an elastic formation.

Whatever the source center frequency, one can notice for the smaller radius that, *in relative values*:

- the radial attenuation of the total stress is more pronounced (contrary to the elastic case),
- the saturant fluid pressure energy is weaker,
- the radial attenuation of the interstitial pressure is greater.

Figures 33 and 34 show the same calculations when the interfaces are permeable. Although the saturant fluid pressure contains more energy, its radial attenuation is again more important for the smaller radius.

In the presence of water, a decrease in the borehole radius does not lead to an important increase of the fluid flow. For the mechanical behavior of the permeable porous formation, it implies that few modifications occur. The *relative* motion between the two phases has varied little. However, because of the incident energy, this motion has been amplified in *absolute* values. This is also true for the saturant fluid pressure at the borehole wall. Thus, for the propagating waves, the ratio of the "useful" energy and the dissipated energy is decreased. The energy transmitted to each of the three body waves is greater. But, on the other hand, the energy dissipation by each of them, as well as the coupling phenomena, do not follow this increase linearly. This should correspond to an apparent higher frequency excitation when the radius is smaller. The Stoneley wave is then more affected; its phase velocity is lowered while its attenuation increases.

Gas saturation

The comparison is made between the elastic case and porous formations whose permeabilities are equal to 2 md and 200 md. Only the situation of open pores is considered.

The spectral energy density diagrams (Figure 35, where $\tilde{k} = 200$ md) show the same results as previously. Stoneley wave energy is reduced more by a radius decrease than in the equivalent elastic case (11.6% instead of 19%). However, compared to the water saturation situation, the relative variation of the energy from one radius to another is

less: only 54% instead of 36%. This is because of low characteristic frequencies. On the other hand, the decrease in the phase velocity is more important than it is for the water.

According to the first resonance, the apparent borehole radius is equal to 10 cm. The ratio of the apparent radii (10/17 = 0.588) is only slightly different from that of the real ratio (7/12 = 0.583). Thus, as for the water, the absolute increase of the pressure leads *essentially* to a decrease in the ratio of the dissipated and total energies. The fluid flow is only slightly affected.

Because of the Stoneley wave phase velocity decrease, this is only for short spacings that the pulse can be seen with a 6.05 ms long time window for a 200 md permeability (Figures 36 and 37 where z=1.25 m and 5.25 m respectively). In order to emphasize this phenomenon, the microseismograms have been computed with a 12.1 ms long time window. The frequency step is identical to the one previously used because 256 frequencies have been considered. The wavetrains obtained with a 7.5 kHz source center frequency are displayed in Figure 38. The spacing varies from 1.25 m to 3.75 m by steps of 0.5 m. Whatever the radial position of observation is, the Stoneley wave cannot be detected for offsets larger than 1.25 m. It contains no significant amount of energy at such a high frequency. It is, however, clearly present with a 0.5 kHz source center frequency (Figure 39). It exhibits a long period characteristic of an important attenuation contribution and a greater time delay compared to the elastic case (the "tube" wave velocity is equal to 1357 m/s).

When the permeability is equal to 2 millidarcies, the borehole radius still plays a part despite the very high critical frequency of the porous material (Figure 37). Figure 40 displays the microseismograms relative to a 5.25 m offset when the source varies from 1.5 kHz to 7.5 kHz by steps of 750 Hz from top to bottom. Case A refers to a borehole radius equal to 12 cm while case B refers to a 7 cm borehole radius. These calculations again emphasize:

- the Stoneley wave phase velocity decrease. For the lowest frequency, it is respectively equal to 1283 m/s and 1230 m/s for cases A and B. This difference increases with lower frequency. At 500 Hz, the respective velocities are 1222 m/s and 1149 m/s.
- the Stoneley wave attenuation increase. The smaller the radius, the longer the period of the associated pulse.
- the importance of the shift toward lower frequencies of the cut-off frequencies of the pseudo-Rayleigh.

When the saturant fluid is as viscous as heavy oil, the effects of the borehole radius are similar to the ones observed in the presence of an elastic formation. The examples

of water and gas show that, from a practical point of view, permeability estimations should take into account smooth variations of the borehole radius to be more reliable.

The effects of the presence of a rigid or elastic tool at the center of the borehole are analogous to the ones observed when the formation is elastic (Schmitt, 1985). In such a configuration, the source "sees" a large radius. In order to model real data with the present formulation, the effective radius to be considered should be only slightly smaller than the real radius (the difference should be less than for an elastic or impermeable interface).

Porosity effects

When the dry rock ("frame") velocities are identical, the P_1 and S wave velocities decrease inversely with the porosity, but not at the same rate. For a given permeability, their attenuations increase (see Part I). In the quasi-static domain of porous medium behavior, shear wave attenuation variations are rather weak.

For a constant permeability, the critical frequency and the coupling coefficients increase with increasing porosity. The attenuation coefficient of the slow P_2 wave is then greater. At the same time, the moving fluid volume increases as well as the relative motion between the two phases ($= \tilde{\phi}(\dot{u} - \dot{U})$). The porous medium is more biphase although the pore radius decreases.

In addition to these complex variations, the mechanical parameters (velocities and density) of the waveguide are modified. For an elastic formation, the greater they are the more important the relative energies of the pseudo-Rayleigh modes because of the efficiency of the waveguide. Furthermore, the Poisson's ratio variations affect the wavetrain internal dynamics (Cheng and Toksöz, 1981). Despite these observations, the two phase character of a porous formation with a permeable interface may be identified through the Stoneley wave behavior.

The calculations are made with porosity values equal to 1%, 5%, 8%, 19% and 30%. Permeability is equal to 200 md and the borehole radius is equal to 12 cm. The formation is still Berea sandstone so that the porous formation coupling coefficients and velocities are shown by Figures 6 a, b , c, d of Part I when the saturant fluid is water. Whatever the saturant fluid is, the "equivalent" elastic formation tube wave velocities for the extreme porosities do not differ by more than 4%. The synthetic microseismograms are displayed for spacings equal to 1.25 m and 3.75 m with a 7.5 kHz source center frequency. The parameter "fac" denotes the relative value of the maxima of amplitude compared to the 19% "equivalent" elastic formation.

Figure 41 A shows the wavetrains obtained at the center of the borehole when the saturant fluid is water. With increasing porosity, Stoneley wave relative amplitude decreases compared to the low frequency part of the pseudo-Rayleigh wave although

less energy is contained in the pseudo-Rayleigh wave. Moreover, despite a continuous decrease in Poisson's ratio and an increasing P_1 wave attenuation, the relative amplitude of the P wavetrain is almost identical from one example to another. At the borehole wall (Figure 40 B), the axial attenuation, mostly related to the Stoneley wave, continuously increases. The difference between each phase velocity and the corresponding elastic formation velocity also increases.

Because of gas characteristics, porosity affects the density more than the P_1 and S wave velocities, as well as the Poisson's ratio, of the gas saturated porous formation (see Table 3). The evolution of the synthetic microseismograms displayed in Figure 42 clearly shows the increasing two phase character of the formations. This assumption is reinforced by the spectral energy density diagram relative to a porosity equal to 1% (Figure 43). It looks much more like an elastic formation than when the porosity is equal to 19% (Figure 14 C) despite a very low critical frequency (0.952 kHz). The biphase character of the porous medium is again emphasized by a decrease in Stoneley wave phase velocity. At 500 Hz, it is equal to 86% of the corresponding "tube" wave velocity. When the porosity increases, this difference increases. For instance, the same ratio at the same frequency is only equal to 53% and 49% respectively for porosities equal to 19% and 30%.

An increase in porosity leads to the same kind of modifications for the wavefield as a permeability increase. The physical reasons are however very different. One must only invoke an increase in the moving fluid volume. Small variations of this parameter have then to be taken into account for the interpretation of real data.

"Dry rock velocity effects"

This last part is in fact a complement to the previous sections. It allows the generalization of the previous results for any type of saturated porous formation.

Low porosity fast formation

The formation is a Fox-Hill sandstone (see Table 1) whose porosity is equal to 7.4%. Only small permeability values are considered: $\tilde{k}$ = 1 md, 10 md and 32.5 md. As with the Berea sandstone, the synthetic microseismograms are compared for a given offset (5.25 m) with the first corresponding to the "equivalent" elastic formation. The permeability increases from top to bottom. The borehole radius is equal to 10 cm. No intrinsic attenuation is taken into account.

Water saturation

When the saturant fluid is water, the critical frequencies relative to the different permeabilities are very high. They are equal to 8950 kHz, 985 kHz and 275 kHz respectively. The body wave attenuation, on the other hand, is relatively weak.

In the presence of an impermeable interface (Figure 44), the amplitude variations are small compared to the elastic case as well as from one permeability to another. The axial attenuation is only slightly modified (Figure 45), whatever the source center frequency and the radial position of observation.

Figure 46 shows the synthetic microseismograms with a free fluid flow condition at the borehole wall. Because of the high critical frequencies, only a few modifications in the internal dynamics can be detected. The wavetrains differ essentially from one another through an important decrease of amplitude and a noticeable increase of the axial attenuation (Figure 47) even for the lower source center frequency. Stoneley wave phase velocity remains almost unchanged. The difference from the elastic case does not exceed 1%, whatever the frequency.

Gas saturation

In the presence of gas, the critical frequencies are lowered to 1408 kHz, 141 kHz and 43 kHz. Then, the limit between the quasi-static and the dynamic behavior of the porous medium is almost reached for the two highest permeabilities.

Despite these characteristics, the waveforms obtained when the pores are sealed (Figure 48) are very similar. This is also true for the axial attenuation (Figure 49). It corresponds to a low shear wave attenuation.

The saturant fluid mobility and compressiblity associated with a high incident energy ($R = 10$ cm) lead to strongly modified wavefields when the interfaces are permeable. Even for the lowest permeability value, one can easily notice (Figure 50):

- a global amplitude decrease associated with an important increase of the axial attenuation (Figure 51);
- an obvious time delay for the Stoneley wave pulse;
- a decrease in the relative and absolute amplitude of the interface wave;
- a relegation of Stoneley wave energy towards the low frequencies. The associated pulse can only be detected with difficulty for the highest permeabilities when the source center frequency is equal to 7.5 kHz. With a 2.5 kHz source center frequency it exhibits the extended period characteristics of large attenuation. At

such a frequency, the difference between its phase velocity and the one relative to the elastic case increases from 4% to 17% with increasing permeability. At 500 Hz, it reaches even higher values (6% and 25%),

- a progressive disappearance of the Airy phase. It is related to a less rigid borehole wall, despite an apparent increase in the borehole radius.

These variations are also shown in the spectral domain. Figure 52 displays the spectral energy densities obtained at the borehole center in the presence of an elastic formation (A), the porous formation with an impermeable interface (B, $\tilde{k} = 32.5$ md) and with a permeable interface (C, $\tilde{k} = 32.5$ md). According to the first resonance, the apparent borehole radius increases to 12 cm when the fluid flow is free (C). This example points out how much the "driving" phenomenon coupled with a low radius can affect the propagation of the guided modes even with a low porosity material.

Slow formation

The last type of formation presented in this study is a high porosity ($\tilde{\phi} = 30\%$) and high permeability ($\tilde{k} = 1$ darcy) slow formation (see Table 1). The borehole radius is equal to 12 cm. The synthetic microseismograms are compared for 3.25 m long offset. From top to bottom of the figures, they are successively relative to the elastic formation (1 (4)), the porous formation with an impermeable interface (2 (5)) and with a permeable interface (3 (6)) computed at the center (the wall) of the borehole.

Water saturation

For the elastic formation equivalent to the water saturated medium, the tube wave velocity is equal to 109% of the shear wave velocity (see Table 3). The Stoneley wave is then attenuated in the low frequency domain due to energy radiation into the formation (Cheng and Toksöz, 1982).

The associated spectral energy density diagram (Figure 53 A) shows that Stoneley wave energy is still present, with its energy concentrated at low frequencies. It exhibits the normal dispersion characteristics of slow formations. Because of the high Poisson's ratio value (0.388), the leaky modes associated with the P wave and the proper resonances of the borehole contain a large amount of energy. These characteristics still hold in the presence of the permeable formation (Figure 53 B). The modifications of the wavefield are analogous, although less pronounced, to the ones described for the fast formations.

The associated microseismograms are displayed in Figure 54. At the borehole center and with a high source center frequency, the wavetrain of the leaky modes is predominant. The similarity of the waveforms emphasizes the small effect of the boundary

conditions on the compressional wave of the first kind. The amplitude maximum is relevant to the permeable situation because of the slight increase in the borehole radius. On the other hand, the internal dynamics characterize the increasing dissipation of energy with changing formation properties. It is only for a low source center frequency that Stoneley wave can be easily detected. Its phase (and group) velocity is however less affected than when the formation is fast. The difference with that of the elastic formation is only equal to 1% and reaches 5% at 500 Hz.

These examples clearly point out that the branch cut associated with the borehole fluid velocity in the scattered wavefield precisely cancels the direct arrival whatever the boundary conditions are.

Gas saturation

Compared to the water saturation case, the "equivalent" gas saturated elastic formation has a much lower Poisson's ratio (0.127) (see Table 3). It corresponds to an important decrease in the P_1 wave velocity and to a greater shear wave velocity. The latter is still less than the "tube" wave velocity.

In the spectral domain, the energy of the "elastic" Stoneley wave (Figure 55 A) is equivalent to that of the water saturated formation. This is also true when the interface is impermeable. The decrease in Poisson's ratio results in much less important P wave leaky modes while the decrease in the density leads to less pronounced proper resonances of the borehole. When the fluid flow is free, the borehole fluid drives the saturant fluid as in the presence of a fast formation. According to the first resonance, the apparent borehole radius is equal to 22 cm. The relegation of Stoneley wave energy, associated with a lowered phase velocity, in a narrower low frequency band leads to an inverse ratio of the different component energies.

The synthetic microseismograms displayed in Figure 56 confirm those observations. When the borehole wall is permeable, the Stoneley wave pulse cannot be detected whatever the source center frequency and the radial position of observation. With a low center source frequency, it is not the Stoneley wave which occurs, but some kinds of a pseudo-mode possibly related to the shear wave. Kurkjian (1985) demonstrated that the shear wave corresponds to a branch cut even in the presence of an elastic slow formation. It contains very little energy in the presence of the elastic formation and when the interface is impermeable. It may play a role when the flow is free because the time window is too short for the Stoneley wave to be present. The latter can be only detected with a short spacing and a low source center frequency as displayed by Figure 57, where it varies in the range [.7, 3.5] kHz from the top to the bottom. Even so, the time window is so short that the dispersion of the interface wave is apparently reversed.

CONCLUSION

The combined calculations of synthetic microseismograms and spectral energy density diagrams, using the discrete wavenumber method, allow a better understanding of wave propagation when logging in saturated porous formations.

Two attenuation phenomena, attributed to fluid flow, take place in such a configuration: the viscous and inertial forces between the two phases of the porous formation and the fluid flow at the borehole wall when unobstructed.

When the pores are sealed at the borehole wall, only the viscous and inertial forces play a part. The modifications of the wavetrains are then essentially due to shear wave attenuation, which is the principal component of both Stoneley and pseudo-Rayleigh waves. The wavefield behavior is practically identical to that of an elastic formation. Stoneley wave phase velocity is only slightly affected. The slow P_2 wave has no noticeable effect.

The scattered wavefield is more affected by the flux at the interface between the borehole fluid and the porous material. For a given formation of any type (i.e., fast or slow), a given pore geometry, a given porosity and a given saturant fluid, the Stoneley wave behavior emphasizes permeability variations. With increasing permeability and for a given borehole radius:

- Stonely wave absolute energy decreases and is relegated to a narrower low frequency band,
- its phase velocity decreases so as to be less than the "tube" wave velocity in an "equivalent" elastic formation. Its dispersion increases, especially in the low frequency domain and in the presence of a fast formation,
- its attenuation increases, reinforced by an increase of the shear wave attenuation related to a less rigid borehole wall.

These effects will be all the more pronounced when the saturant fluid is of low viscosity and high compressibility. The critical frequency may not then play a predominant role, because the borehole fluid "drives" the saturant fluid efficiently. When the viscosities are nearly equal, the more compressible saturant fluid (in absolute values and compared to the borehole fluid) will lead to the most important modifications of the wavefield. When the saturant fluid is as viscous as water, the changes will be all the more pronounced when the dynamic behavior of the saturated porous formation is approached (i.e., the critical frequency is low). However, porosity also enhances the permeability effects through an increase in the moving fluid volume.

Due to an apparent increase in the borehole radius, the proper resonances of the borehole and associated low cut-off frequencies of the pseudo-Rayleigh modes are shifted

toward lower frequencies. The Airy phases are more attenuated. In the presence of a movable and compressible saturant fluid, the energy distribution among the interface wave and the trapped modes may then be reversed. When the formation is slow, the P wave leaky modes are enhanced.

Any intrinsic attenuation relative either to the borehole fluid or the matrix of the formation is superimposed on the other attenuation mechanisms which may then be superseeded, especially when the permeability is low.

The Stoneley wave appears to be an excellent evaluation criterion for the permeability of a formation. Contrary to what was stated by Rosenbaum (1974), its increasing decay rate is not the only indication. Its phase (and group) velocity also contains a lot of information. Furthermore, the use of a high frequency band pass tool is unsuitable. Actually, the tool should not cut off the low frequencies since most of the useful and easily extractable information is found there.

These results are in good agreement with the observations from real data made by Williams et al. (1984) and those of Burns and Cheng (this issue). They, however, pose the problem of the reliability of the indirect shear wave velocity determination through Stoneley wave characteristics, such as when logging in transversely isotropic formations (Chen and Willen, 1984; Liu, 1984). In addition, the measurements have to be corrected for the intrinsic attenuation of both the bore fluid and the matrix (see also Burns and Cheng, this issue).

For a given permeability, a decrease in the borehole radius only slightly enhances the relative motion between the two phases of the porous medium. It leads however to a much greater dissipation of energy. The wave propagation is also changed. The shear wave becomes more inhomogeneous while the slow P_2 wave plays a more "efficient" part. The modifications of the Stoneley wave characteristics (velocity and attenuation) previously described are then enhanced for a given permeability. This amplification will be all the more important when the permeability is high. From a practical point of view, the reliability of an absolute permeability determination will need to take into account the "slow" (long period) borehole radius variations and not only washouts.

ACKNOWLEDGEMENTS

I am indebted to Dr. M. Bouchon and Dr. G. Bonnet of the University of Grenoble for many valuable and helpful discussions. I would like to thank Prof. M. N. Toksöz, Dr. C. H. Cheng and Dr. R.H. Wilkens of ERL for constructive and stimulating comments on this manuscript. This work was supported by the Société Nationale Elf Aquitaine (Production) and the Centre de Calcul Vectoriel pour la Recherche.

REFERENCES

Biot, M.A., 1956a, Theory of propagation of elastic waves in a fluid saturated porous solid. I. Low frequency range. J. Acoust. Soc. Am., 28, 168-178.

———, 1956b, Theory of propagation of elastic waves in a fluid saturated porous solid. II. Higher frequency range. J. Acoust. Soc. Am., 28, 179-191.

Bonnet, G., 1985, Contribution a l'étude des milieux poreux saturés en régime dynamique. Thèse d'Etat. Montpellier Univ.

Borne, L., 1983, Contribution a l'étude du comportement dynamique des milieux poreux saturés deformables. Etude de la loi de filtration dynamique. These D.I. Grenoble Univ.

Bouchon, M., and Aki, K., 1977, Discrete wavenumber representation of seismic source wavefields. Bull. Seism. Soc. Am., 67, 259-277.

Boutin, C., 1983, Contribution a l'étude du comportement dynamique des milieux poreux. D.E.A. Grenoble Univ.

Burns, D.R., and Cheng, C.H., 1986, Determination of in-situ permeability from tube wave velocity and attenuation. This issue.

Chen, S.T., and Willen, D.E., 1984, Shear wave logging in slow formations. 25th SPWLA meeting, paper DD.

Cheng, C.H., and Toksöz, M.N., 1978, Inversion of seismic velocities for the pore aspect ratio spectrum of a rock. J. Geophys. Res., 84, 7533-7543.

Cheng, C.H., and Toksöz, M.N., 1981, Elastic wave propagation in a fluid filled borehole and synthetic acoustic logs, Geophysics, 46, 1042-1053.

Cheng, C.H., and Toksöz, M.N, 1982, Generation, propagation and analysis of tube waves in a borehole, 23 rd SPWLA meeting.

Dutta, N.C., and Odé, H., 1983, Seismic reflections from a gas water contact. Geophysics, 48, 148-162.

Feng, S., and Johnson, D.L., 1983a, High frequency acoustic properties of a fluid/porous interface. I. New surface mode. J. Acoust. Soc. Am., 74, 906-914.

———————, 1983b, High frequency acoustic properties of a fluid/porous interface. II. The 2D reflection Green's function. J. Acoust. Soc. Am., 74, 915-925.

Kurkjian, A.L, 1985, Numerical computation of individual far field arrivals excited by an acoustic source in a borehole. Geophysics, 50, 852-866

Kuster, G.T., and Toksöz, M.N., 1974a, Velocity and attenuation of seismic waves in two phase media. I. Theoretical formulation. Geophysics, 39, 587-606.

————————————, 1974b, Velocity and attenuation of seismic waves in two phase media. II. Experimental results. Geophysics, 39, 607-618.

Liu, O.Y., 1984, Stoneley wave derived Δ t shear log. 25th SPWLA meeting Paper ZZ.

Mathieu, F., 1984, Application of full waveform acoustic logging data to the estimation of reservoir permeability. MS thesis. M.I.T.

Mayes, M.J., Nagy, P.B., and Adler, L., 1986, Excitation of surface waves of different modes at fluid-porous solid interface, J. Acoust. Soc. Am.,79, 249-252.

Mavko, G.M, and Nur, A., 1978, The effect of non elliptical cracks on the compressibility of rocks, J. Geophys. Res., 83, 4459-4468.

Pal, P.C., 1983, On the disturbance produced by an impulsive shearing stress on the surface of a semi-infinite poro-elastic medium. J. Acoust. Soc. Am., 74, 586-590.

Rasolofossaon, N.J.P., 1984, Propagation des ondes dans les milieux poreux saturés. Effets des discontinuités. Ondes Réfléchies. Ondes transmises. Ondes d'interface. Rapport IFP/SNEA(P).

Rosenbaum, J.H., 1974, Synthetic microseismograms: logging in porous formations. Geophysics, 39, 14-32.

Schmitt, D.P, and Bouchon, M., 1985, Full wave acoustic logging: synthetic microseismograms and frequency wavenumber analysis, Geophysics, 50, 1756-1778.

Schmitt, D.P, 1985, Simulation numérique de diagraphies acoustiques. Propagation d'ondes dans des formations cylindriques axisymétriques radialement stratifiées incluant des milieux élastiques et/ou poreux saturés. Ph.D. thesis. Univ. Grenoble.

Schmitt, D.P., 1986, Full wave synthetic acoustic logs in saturated porous media Part I: a review of Biot's theory. This issue.

Tatham, R.H., 1982, V_p/V_s and lithology. Geophysics, 47, 326-334.

Toksöz, M.N., Cheng, C.H., and Timur, A., 1976, Velocities of seismic waves in porous rocks. Geophysics, 41, 621-645.

Truesdell, C., and Toupin, R., 1960, Handbuck der Physick; vol. III/1, Springler Verlag. Ed. Berlin.

Tubman, K.M., Cheng, C.H., and Toksöz, M.N., 1984, Synthetic full waveform acoustic logs in cased boreholes. Geophysics, 49, 1051-1059.

White, J.E., 1983, Underground Sound, Elsevier, Amsterdam.

Williams, D.M., Zemanek, J., Angona, F.A., Dennis, C.L., and Caldwell, R.L., 1984, The long spaced acoustic logging tool. 25th SPWLA meeting. Paper T.

Winkler, K.M., and Nur, A., 1982, Seismic attenuation: effect of pore fluids and frictional sliding, Geophysics, 47, 1-15.

Zhang, J., and Cheng, C.H., 1984, Numerical studies of body wave amplitudes in full waveform acoustic logs, 9th Int. Form. Ev. Conf., SAIS, Paper 14.

APPENDIX

Elements of the $\underline{\mathbf{M}}^{(1)}$ and $\underline{\mathbf{M}}^{(2)}$ matrices

The term $e^{i(kz+\omega t)}$ is omitted.

$$
\begin{aligned}
M_{11}^{(1)} &= kp_1\, I_1(kp_1\, R) \\
M_{12}^{(1)} &= kp_{21}\, K_1(kp_{21}\, R)\, \left[1-\tilde{\phi}_2(1-\xi_{21})\right] \\
M_{13}^{(1)} &= kp_{22}\, K_1(kp_{22}\, R)\, \left[1-\tilde{\phi}_2(1-\xi_{22})\right] \\
M_{14}^{(1)} &= i\,k\, K_1(ks_2\, R)\, \left[1-\tilde{\phi}_2(1-\chi_2)\right]
\end{aligned}
$$

$$
\begin{aligned}
M_{21}^{(1)} &= \rho_1\omega^2\, I_0(kp_1\, R) \\
M_{22}^{(1)} &= -2\,N_2\,kp_{21}^2\, \left[K_0(kp_{21}\, R)+\frac{1}{kp_{21}\, R}K_1(kp_21\, R)\right] \\
&\quad +\frac{\omega^2}{\alpha_{21}^2}\left[A_2+Q_2+(Q_2+\tilde{R}_2)\xi_{21}\right]\, K_0(kp_{21}\, R) \\
M_{23}^{(1)} &= -2\,N_2\,kp_{22}^2\, \left[K_0(kp_{22}\, R)+\frac{1}{kp_{22}\, R}K_1(kp_{22}\, R)\right] \\
&\quad +\frac{\omega^2}{\alpha_{22}^2}\left[A_2+Q_2+(Q_2+\tilde{R}_2)\xi_{22}\right]\, K_0(kp_{22}\, R) \\
M_{24}^{(1)} &= -2\,N_2\,k\,ks_2\, \left[K_0(ks_2\, R)+\frac{1}{ks_2\, R}K_1(ks_2\, R)\right] \\
M_{31}^{(1)} &= 0 \\
M_{32}^{(1)} &= -2\,i\,N_2\,k\,kp_{21}\, K_1(kp_{21}\, R) \\
M_{33}^{(1)} &= -2\,i\,N_2\,k\,kp_{22}\, K_1(kp_{22}\, R) \\
M_{34}^{(1)} &= N_2\, \left[2k^2-\frac{\omega^2}{\beta_2^2}\, K_1(ks_2\, R)\right]
\end{aligned}
$$

$$
\begin{aligned}
M_{41}^{(1)} &= \rho_1\omega^2\, I_0(kp_1\, R) \\
M_{42}^{(1)} &= \frac{\omega^2}{\tilde{\phi}_2\alpha_{21}^2}\left[Q_2+\tilde{R}_2\xi_{21}\right]\, K_0(kp_{21}\, R) \\
M_{43}^{(1)} &= \frac{\omega^2}{\tilde{\phi}_2\alpha_{22}^2}\left[Q_2+\tilde{R}_2\xi_{22}\right]\, K_0(kp_{22}\, R) \\
M_{44}^{(1)} &= 0
\end{aligned}
$$

$$
\begin{aligned}
M_{11}^{(2)} &= M_{11}^{(1)} \\
M_{12}^{(2)} &= kp_{21}\, K_1(kp_{21}\, R) \\
M_{13}^{(2)} &= -kp_{22}\, K_1(kp_{22}\, R) \\
M_{14}^{(2)} &= i\, k\, K_1(ks_2\, R) \\
M_{21}^{(2)} &= M_{21}^{(1)} \\
M_{22}^{(2)} &= M_{22}^{(1)} \\
M_{23}^{(2)} &= M_{23}^{(1)} \\
M_{24}^{(2)} &= M_{24}^{(1)} \\
M_{31}^{(2)} &= M_{31}^{(1)} \\
M_{32}^{(2)} &= M_{32}^{(1)} \\
M_{33}^{(2)} &= M_{33}^{(1)} \\
M_{34}^{(2)} &= M_{34}^{(1)} \\
M_{41}^{(2)} &= 0 \\
M_{42}^{(2)} &= kp_{21}\, [\, \xi_{21} - 1\,]\, K_1(kp_{21}\, R) \\
M_{43}^{(2)} &= kp_{22}\, [\, \xi_{22} - 1\,]\, K_1(kp_{22}\, R) \\
M_{44}^{(2)} &= i\, k\, [\, \chi_2 - 1]\, K_1(ks_2\, R)
\end{aligned}
$$

TABLE 1

Formation parameters

Name	K_s (Pa)	ρ_s (kg m^{-3})	α_m (ms^{-1})	β_m (ms^{-1})	$\tilde{\phi}$ (%)	$\tilde{k}$ (Darcy)
Berea Sandstone [1]	3.79 10^{10}	2650	3670	2170	19	0.2
Fox Hill sandstone [1]	3.79 10^{10}	2650	4450	2515	7.4	10^{-3},10^{-2}, 0.0325
Slow formation [2]	3.5 10^{10}	2600	1500	1000	30	1

[1] From Rosenbaum (1974)
[2] From Dutta and Odé (1983)

TABLE 2

Saturant fluid parameters

Name	α_f (ms^{-1})	ρ_f (kg m^{-3})	η (cp)
Water	1500	1000	1.
Gaseous water [1]	800	1000	1.
Heavy oil 2	1455.4	879.4	180.
Gas [3]	629.7	139.8	0.022

[1] see text
[2] From Kuster and Toksöz (1974b)
[3] From Rosenbaum (1974)

TABLE 3

Equivalent elastic formation parameters

Formation	Fluid	$\tilde{\phi}$ %	α (ms^{-1})	β (ms^{-1})	ρ ($kg\ m^{-3}$)	ν
Berea sandstone	Oil	19	3702.8	2090.2	2313.6	0.269
	Water	1	4348.9	2165.9	2633.5	0.335
		5	4033.7	2148.8	2567.7	0.302
		8	3930.6	2135.3	2518.0	0.291
		10	3882.2	2126.0	2485.0	0.286
		19	3735.8	2080.0	2336.5	0.275
		30	3600.0	2013.0	2155.0	0.273
	$Water_G$	19	3586.6	2080.0	2336.5	0.247
	Gas	1	3736.1	2169.0	2624.9	0.246
		5	3681.0	2167.0	2524.5	0.235
		8	3672.7	2165.1	2422.7	0.234
		10	3669.0	2164.0	2399.0	0.233
		19	3654.0	2156.7	2173.1	0.233
		30	3639.9	2145.9	1896.9	0.233
Fox Hill sandstone	Water	7.4	4466.0	2477.9	2527.9	0.278
	Gas	7.4	4443.0	2509.7	2464.2	0.266
Slow formation	Water	30	2168.2	927.8	2155.0	0.388
	Gas	30	1512.7	988.8	1896.9	0.127

ν denotes Poisson's ratio
$Water_G$ denotes the gaseous water of Table 2

TABLE 4

Q values used in Figure 13

Q_{α_1} denotes the bore fluid quality factor
Q_{α_m} and Q_{β_m} are the matrix quality factors

Example	Q_{α_1}	Q_{α_m}	Q_{β_m}
1	∞	∞	∞
2	∞	60	60
3	∞	∞	∞
4	∞	60	60
5	∞	100	50
6	∞	∞	∞
7	20	60	60
8	20	20	10
9	∞	∞	∞
10	∞	20	10

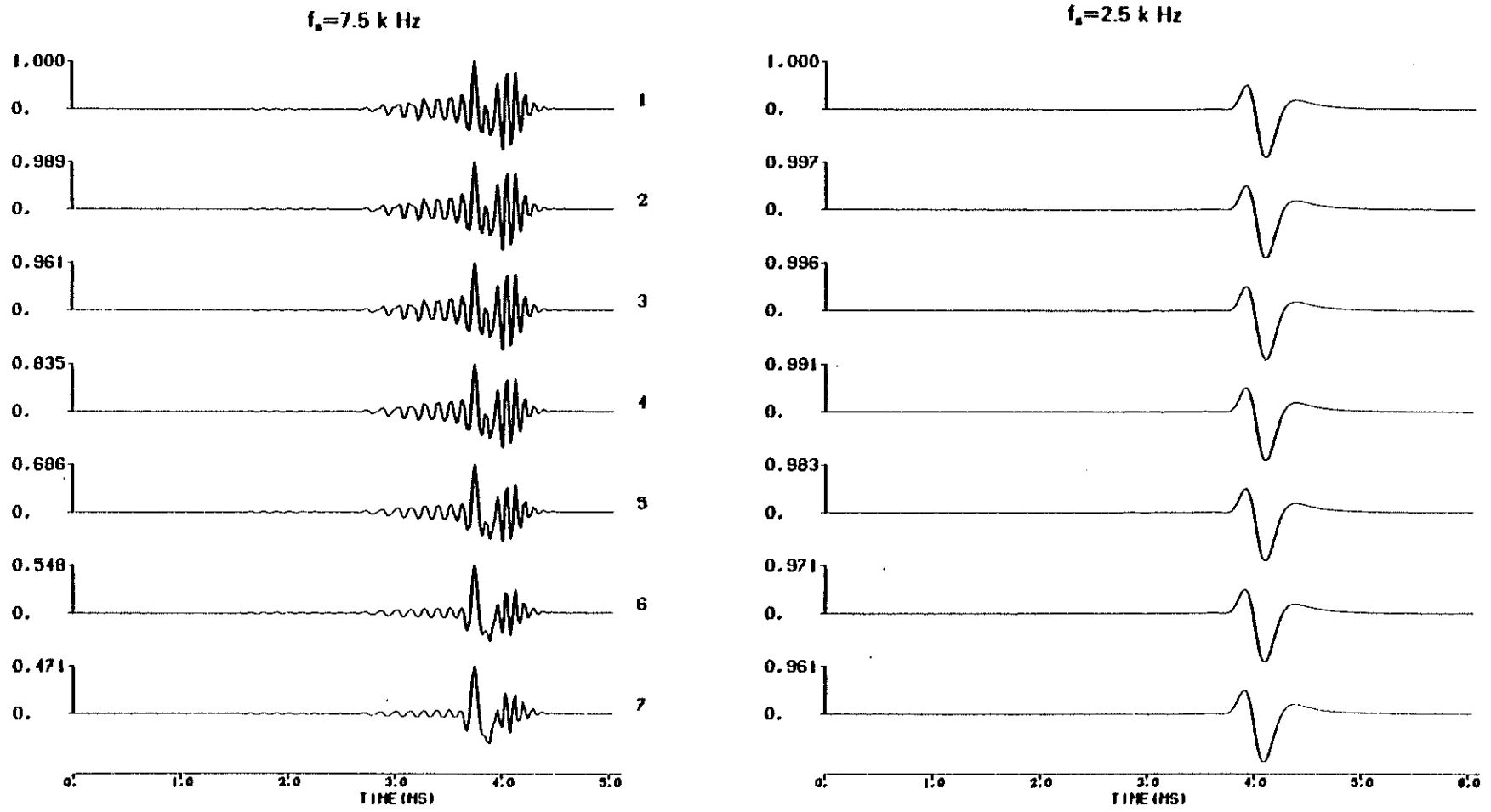

Figure 1: Impermeable interface. Permeability effects in the presence of water saturated Berea sandstone ($\tilde{\phi}$ =19%, R = 12 cm). Iso-offset (5.25 m) comparison of the synthetic microseismograms obtained at the borehole center. f_s denotes the source center frequency. Each series is normalized with respect to its own maximum (1.00). The permeability increases from top to bottom. 1: Elastic, 2: $\tilde{k}$ = 2 md, 3: $\tilde{k}$ = 32.5 md, 4: $\tilde{k}$ = 200 md, 5: $\tilde{k}$ = 500 md, 6: $\tilde{k}$ = 1 darcy, 7: $\tilde{k}$ = 1.5 darcy.

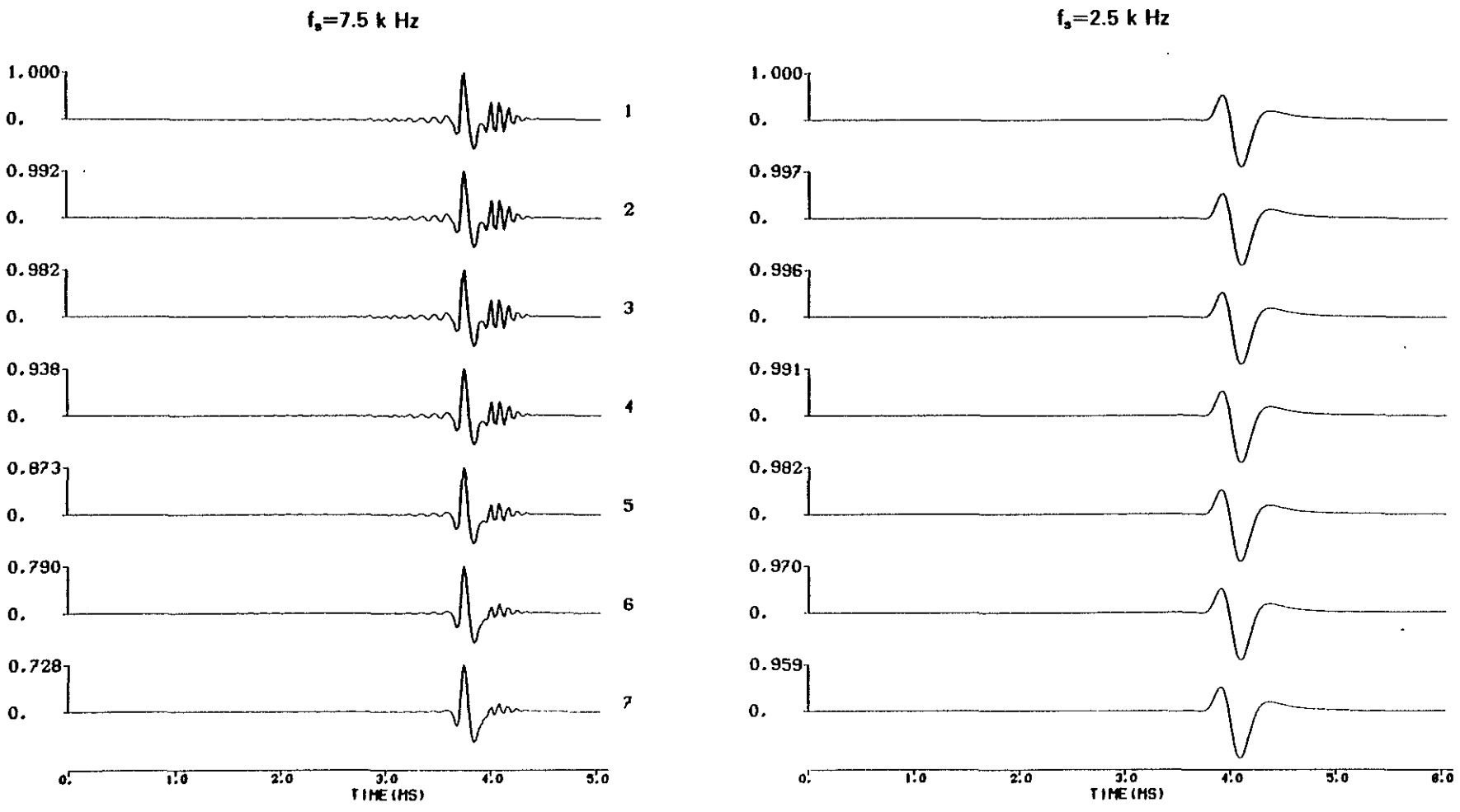

Figure 2: Same as Figure 1 at the borehole wall.

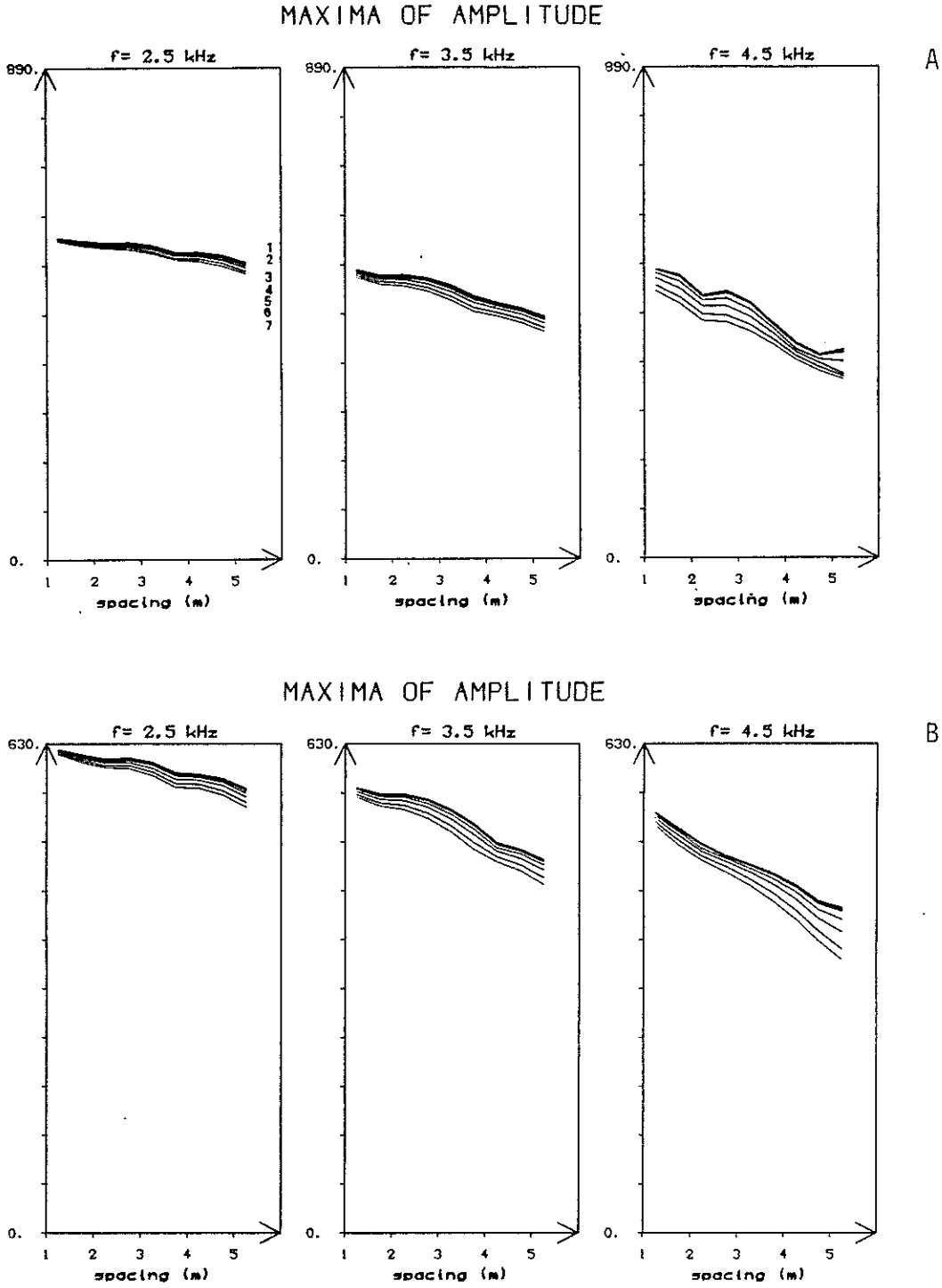

Figure 3: Variation of the maxima of amplitude as a function of the offset of the synthetic microseismograms relative to Figure 1 (A) and Figure 2 (B). f denotes the source center frequency.

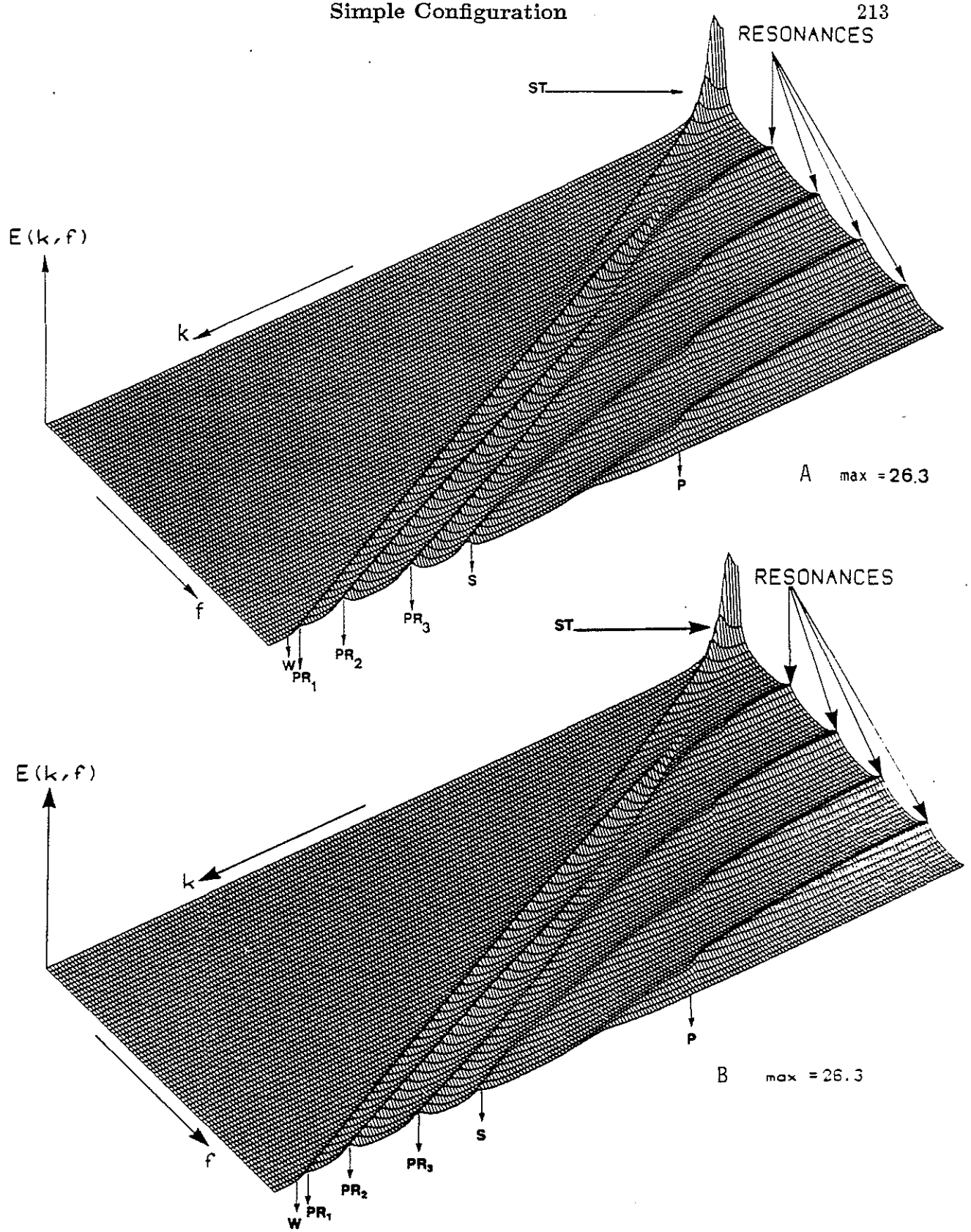

Figure 4: Spectral energy density diagrams obtained at the center of the borehole (R = 12 cm) in the presence of the equivalent elastic formation (see Table 3) (A) and of water saturated Berea sandstone ($\tilde{\phi}$ = 19% , $\tilde{k}$ = 200 md) when the interface is impermeable (B). Each diagram is normalized with respect to its own maximum indicated by max.

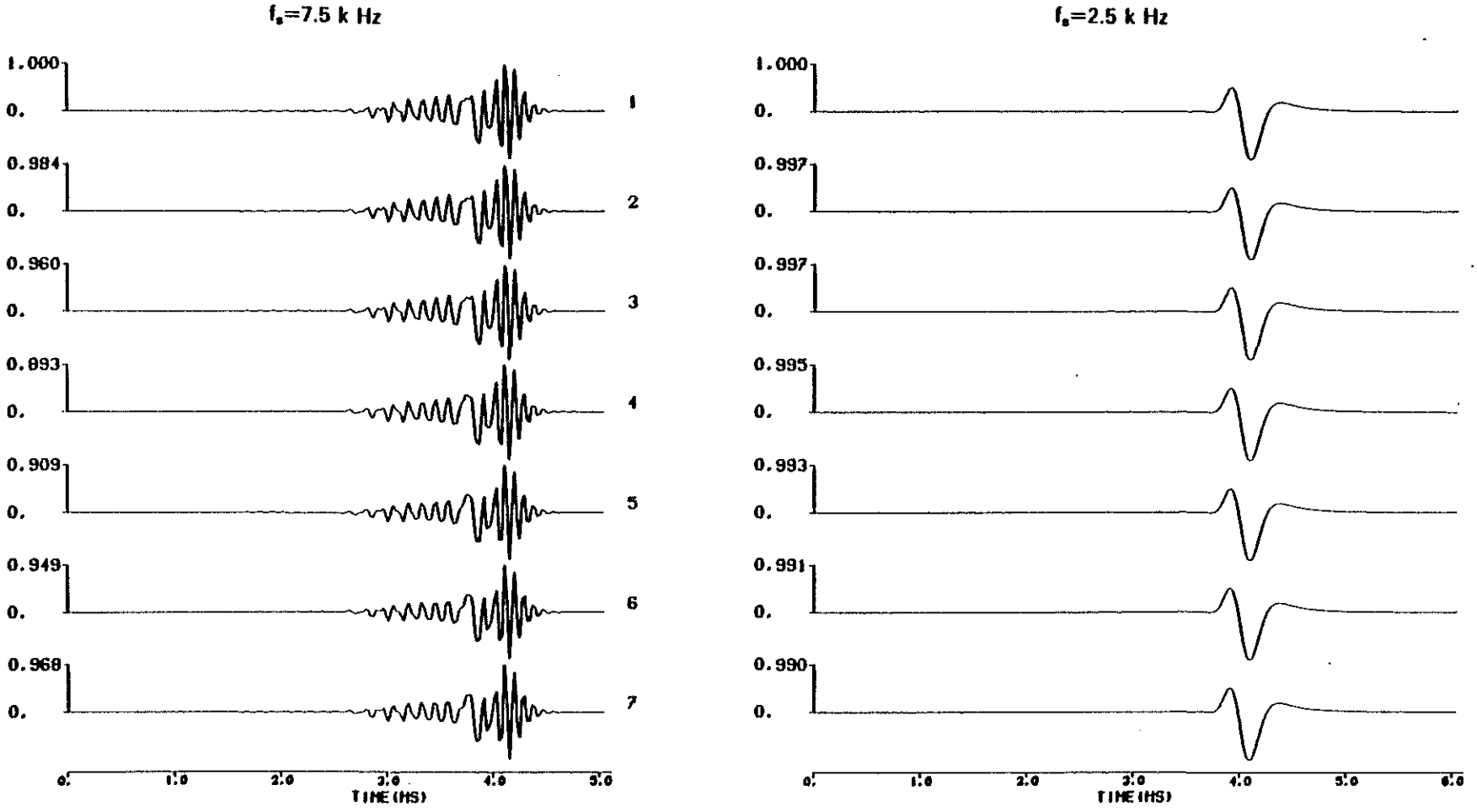

Figure 5: Impermeable interface. Permeability effects in the presence of the gas saturated Berea sandstone ($\tilde{\phi}$ =19%, R = 12 cm). Iso-offset (5.25 m) comparison of the synthetic microseismograms obtained at the borehole center. f_s denotes the source center frequency. Each series is normalized with respect to its own maximum (1.00). The permeability increases from top to bottom. 1: Elastic, 2: $\tilde{k}$ = 2 md, 3: $\tilde{k}$ = 32.5 md, 4: $\tilde{k}$ = 200 md, 5: $\tilde{k}$ = 500 md, 6: $\tilde{k}$ = 1 darcy, 7: $\tilde{k}$ = 1.5 darcy.

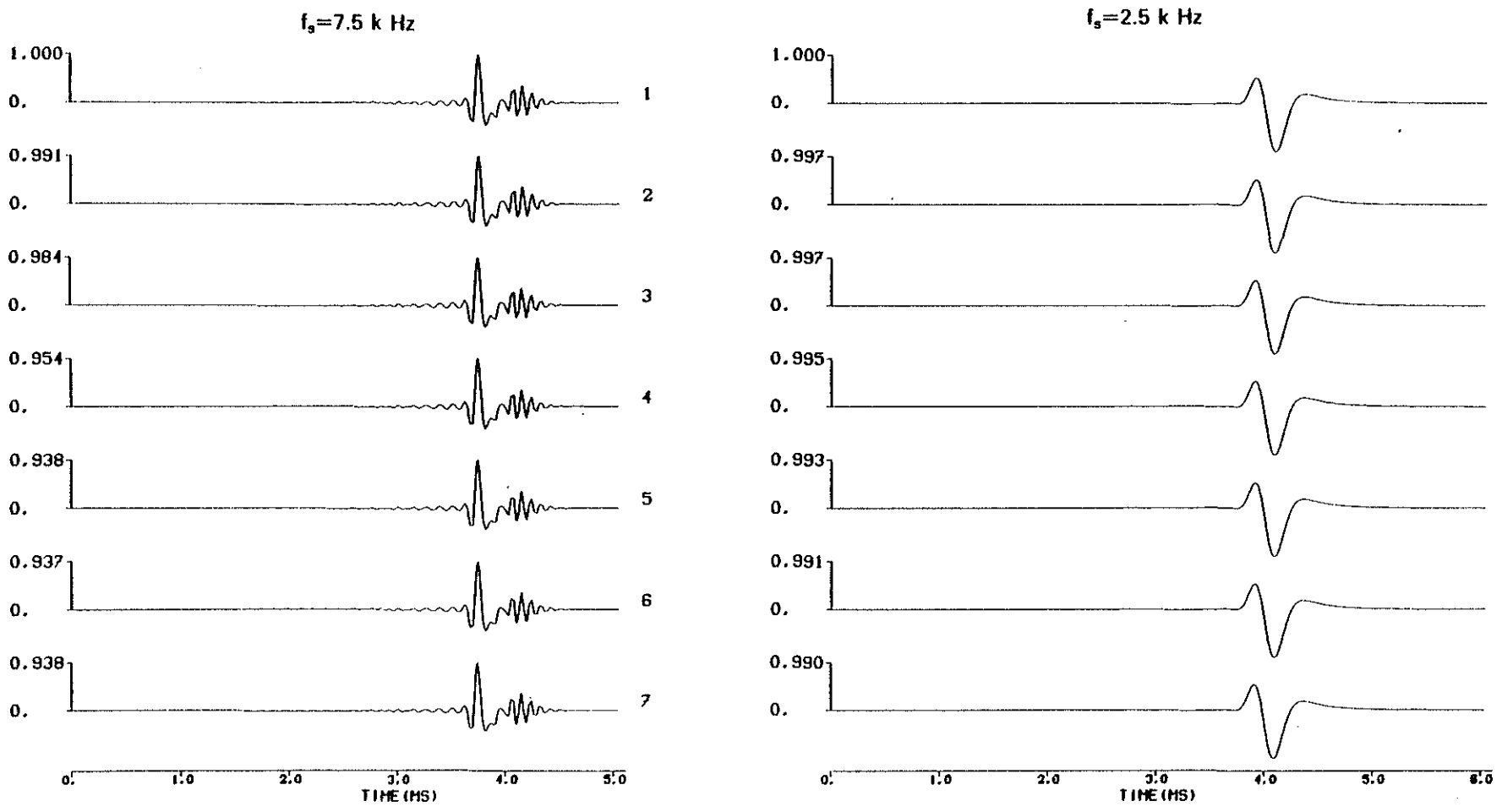

Figure 6: Same as Figure 5 at the borehole wall.

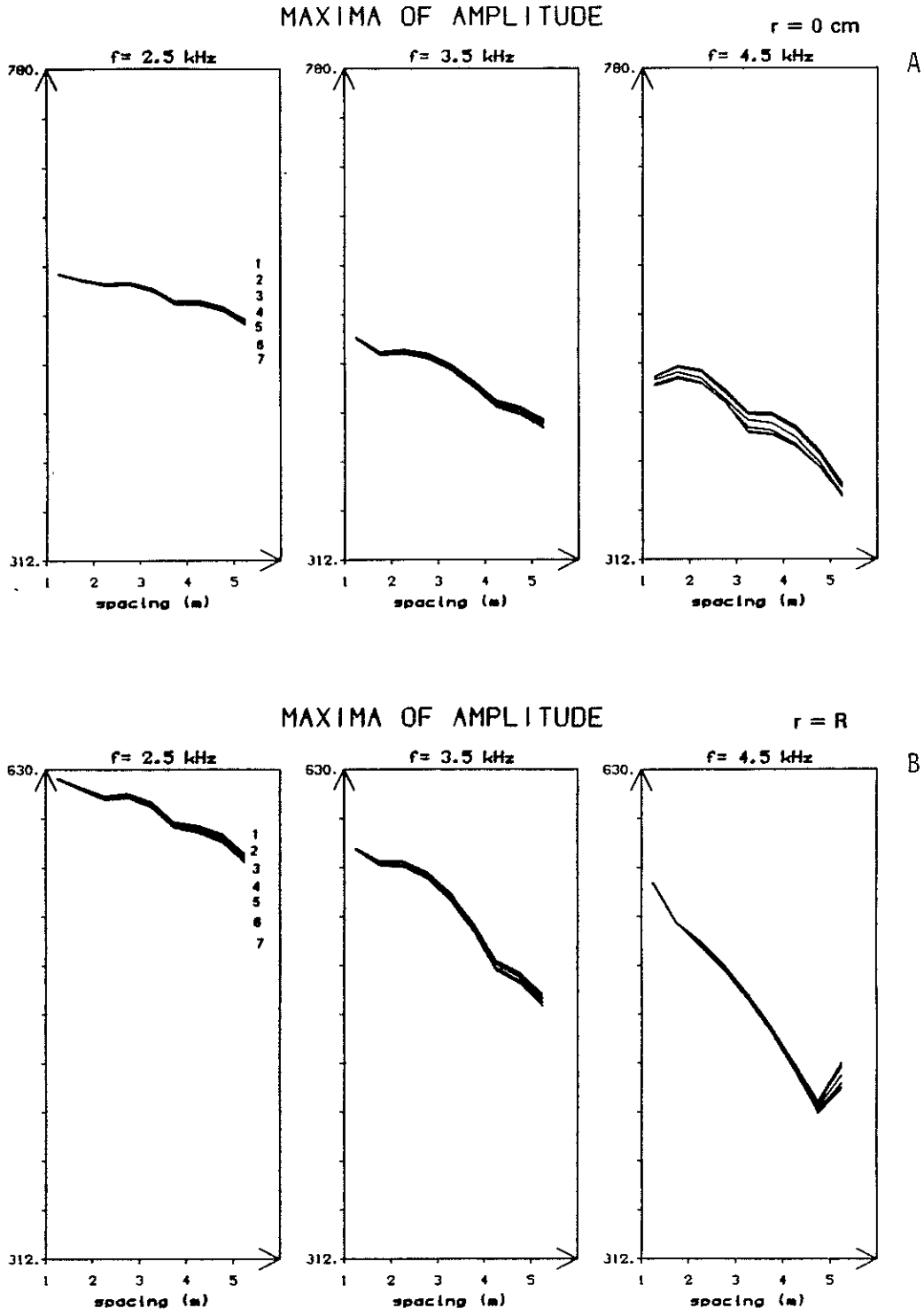

Figure 7: Variation of the maxima of amplitude as a function of the offset of the synthetic microseismograms relative to Figure 5 (A) and Figure 6 (B). f denotes the source center frequency.

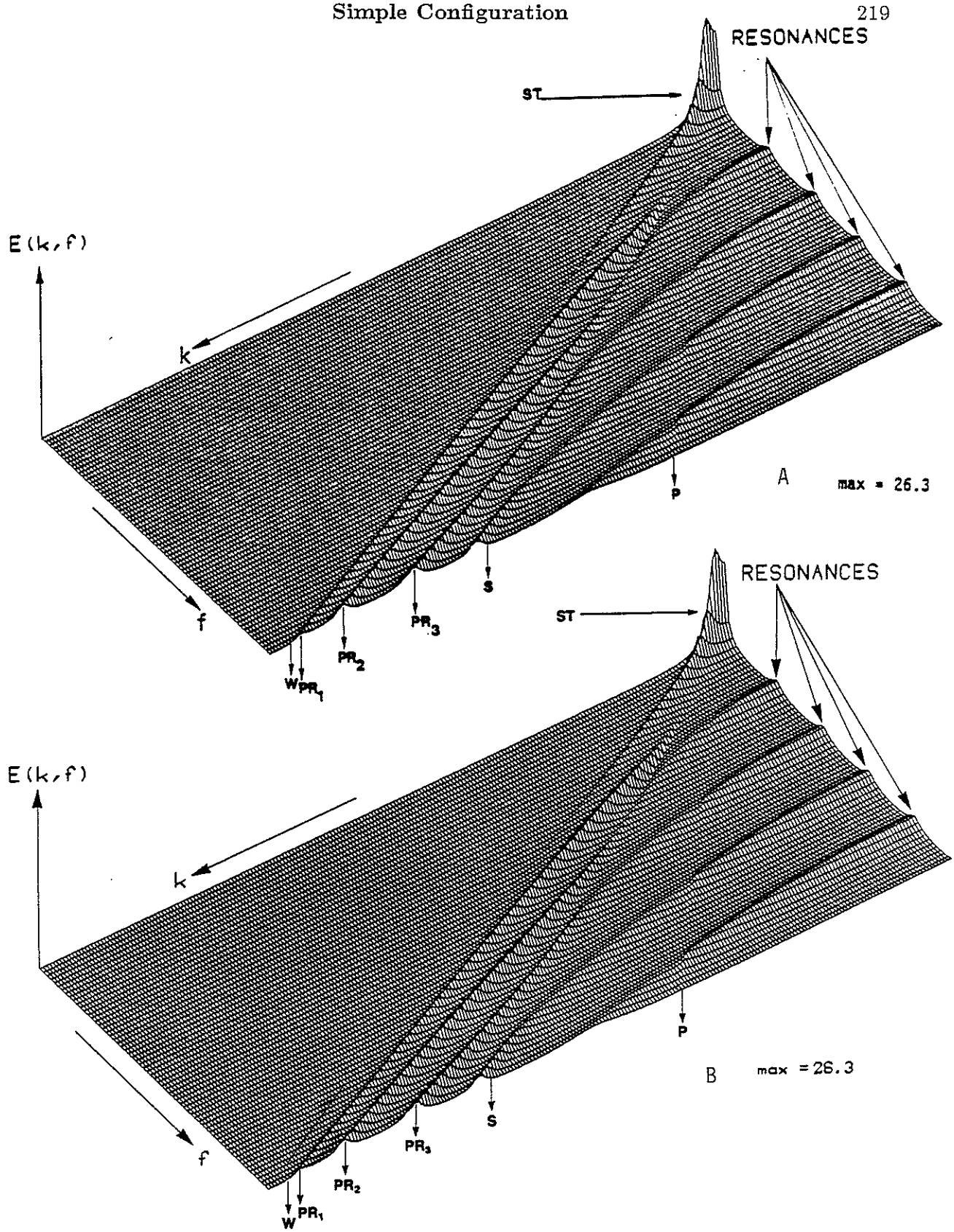

Figure 8: Spectral energy density diagrams obtained at the center of the borehole (R = 12 cm) in the presence of the equivalent elastic formation (see Table 3) (A) and of gas saturated Berea sandstone ($\tilde{\phi} = 19\%$, $\tilde{k} = 200$ md) when the interface is impermeable. Each diagram is normalized with respect to its own maximum indicated by max.

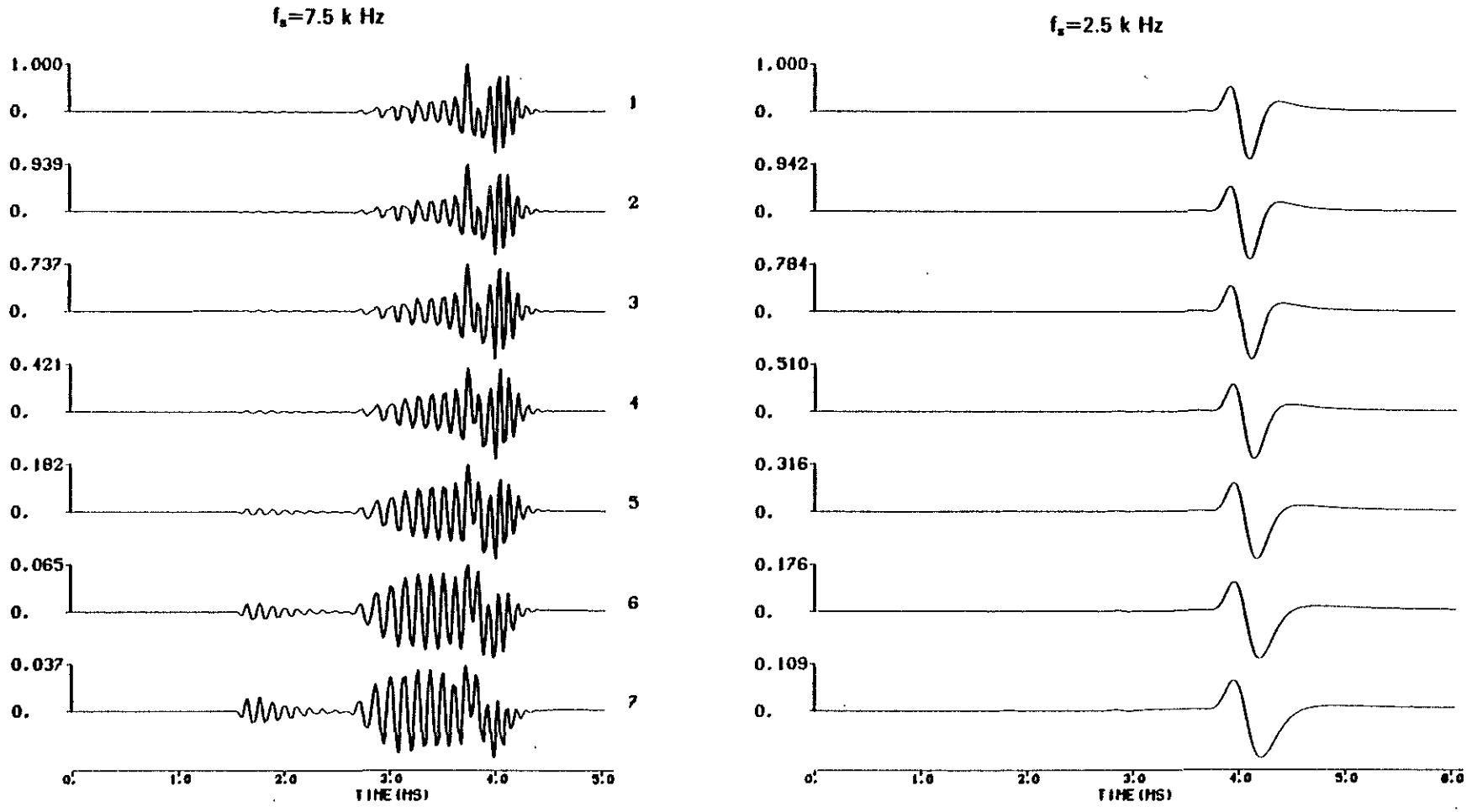

Figure 9: Permeable interface. Permeability effects in the presence of water saturated Berea sandstone ($\tilde{\phi}$ =19%, R = 12 cm). Iso-offset (5.25 m) comparison of the synthetic microseismograms obtained at the borehole center. f_s denotes the source center frequency. Each series is normalized with respect to its own maximum (1.00). The permeability increases from top to bottom. 1: Elastic, 2: $\tilde{k}$ = 2 md, 3: $\tilde{k}$ = 32.5 md, 4: $\tilde{k}$ = 200 md, 5: $\tilde{k}$ = 500 md, 6: $\tilde{k}$ = 1 darcy, 7: $\tilde{k}$ = 1.5 darcy. Compare with Figure 1.

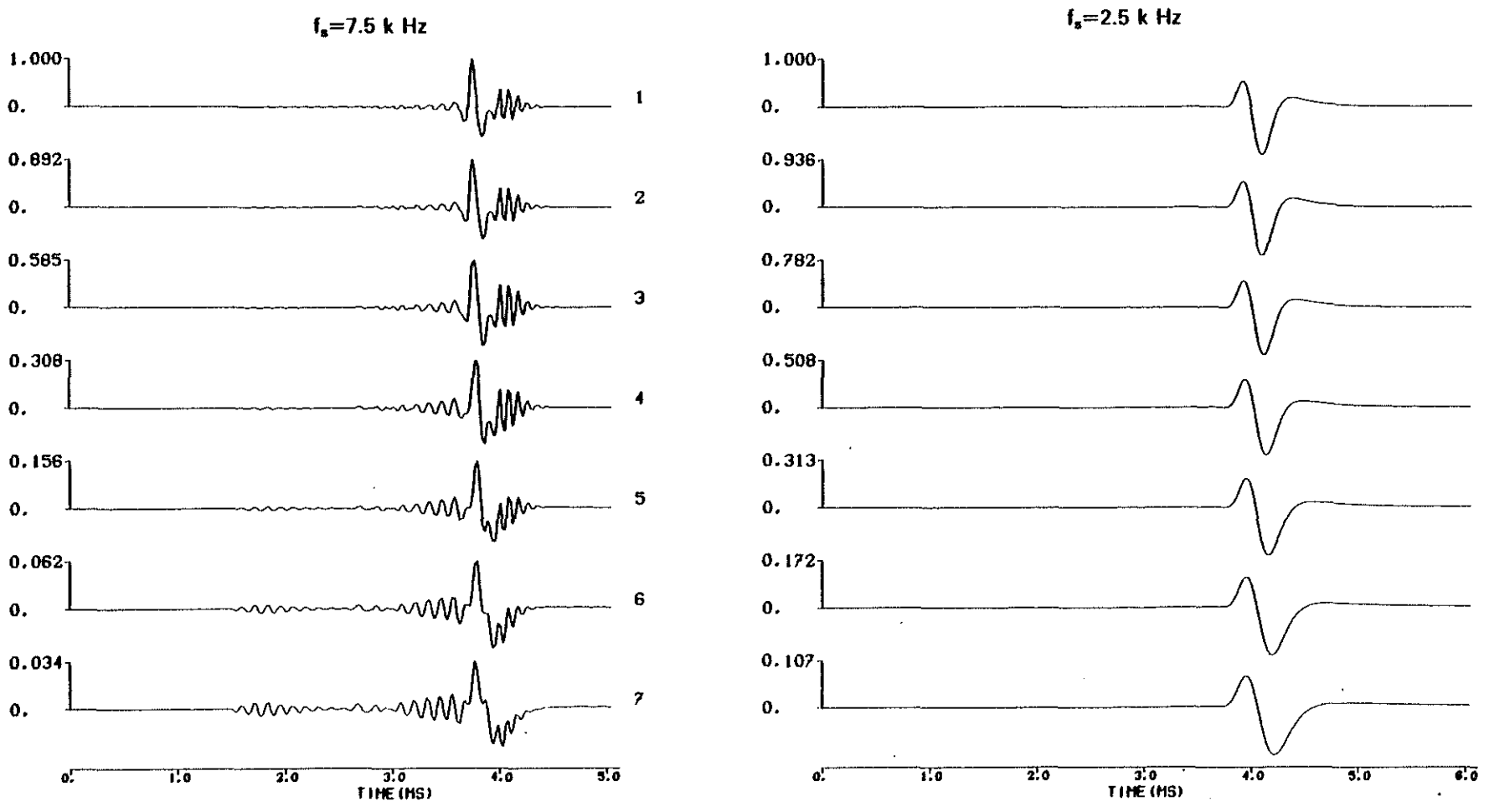

Figure 10: Same as Figure 9 at the borehole wall. Compare with Figure 2.

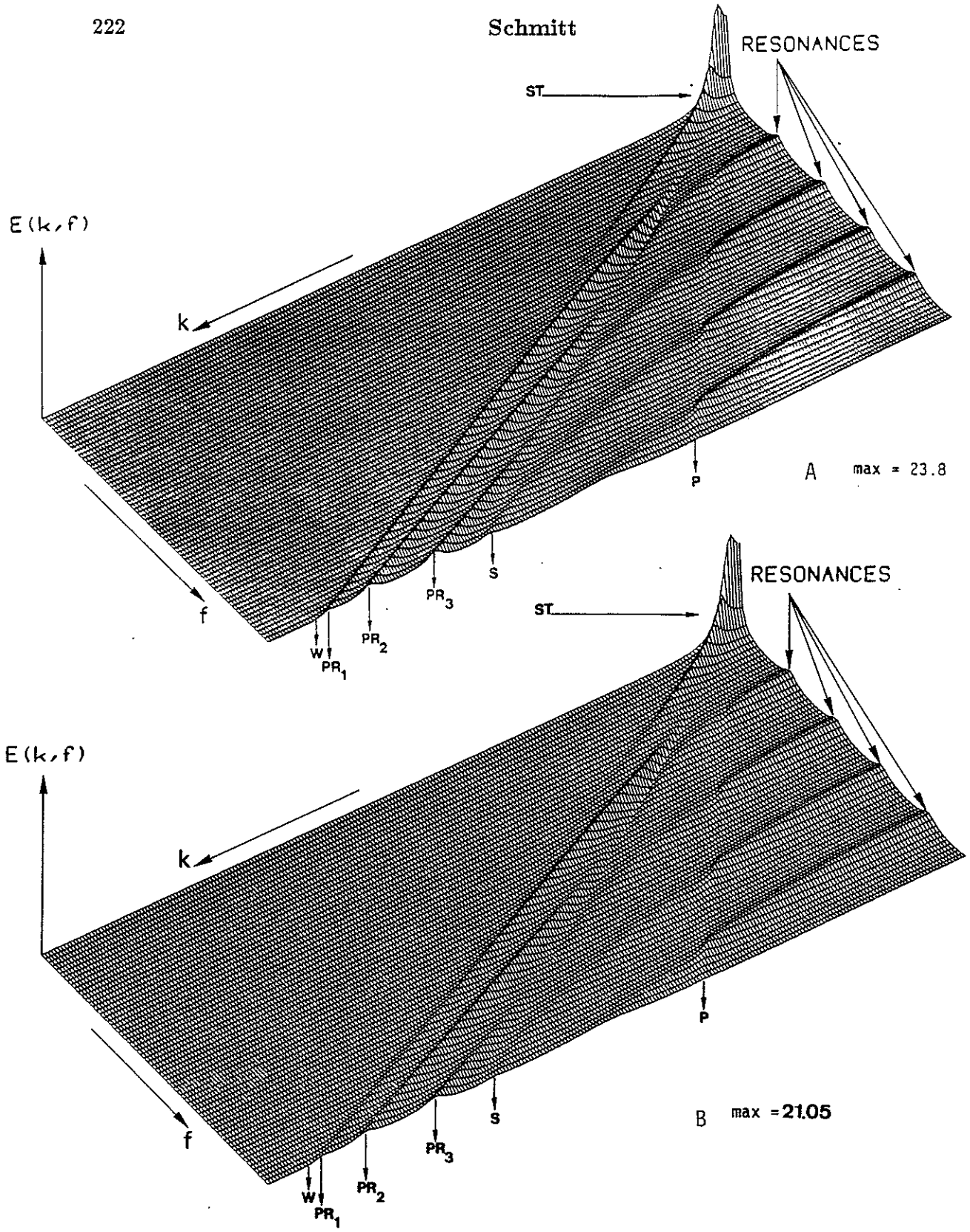

Figure 11: Permeable interface. Spectral energy density diagrams obtained at the borehole center (R = 12 cm) in the presence of water saturated Berea sandstone ($\tilde{\phi}$ = 19%. The permeability is equal to 200 md (A) and 1 darcy (B). Each diagram is normalized with respect to its own maximum indicated by max. Compare with Figures 4 A, B.

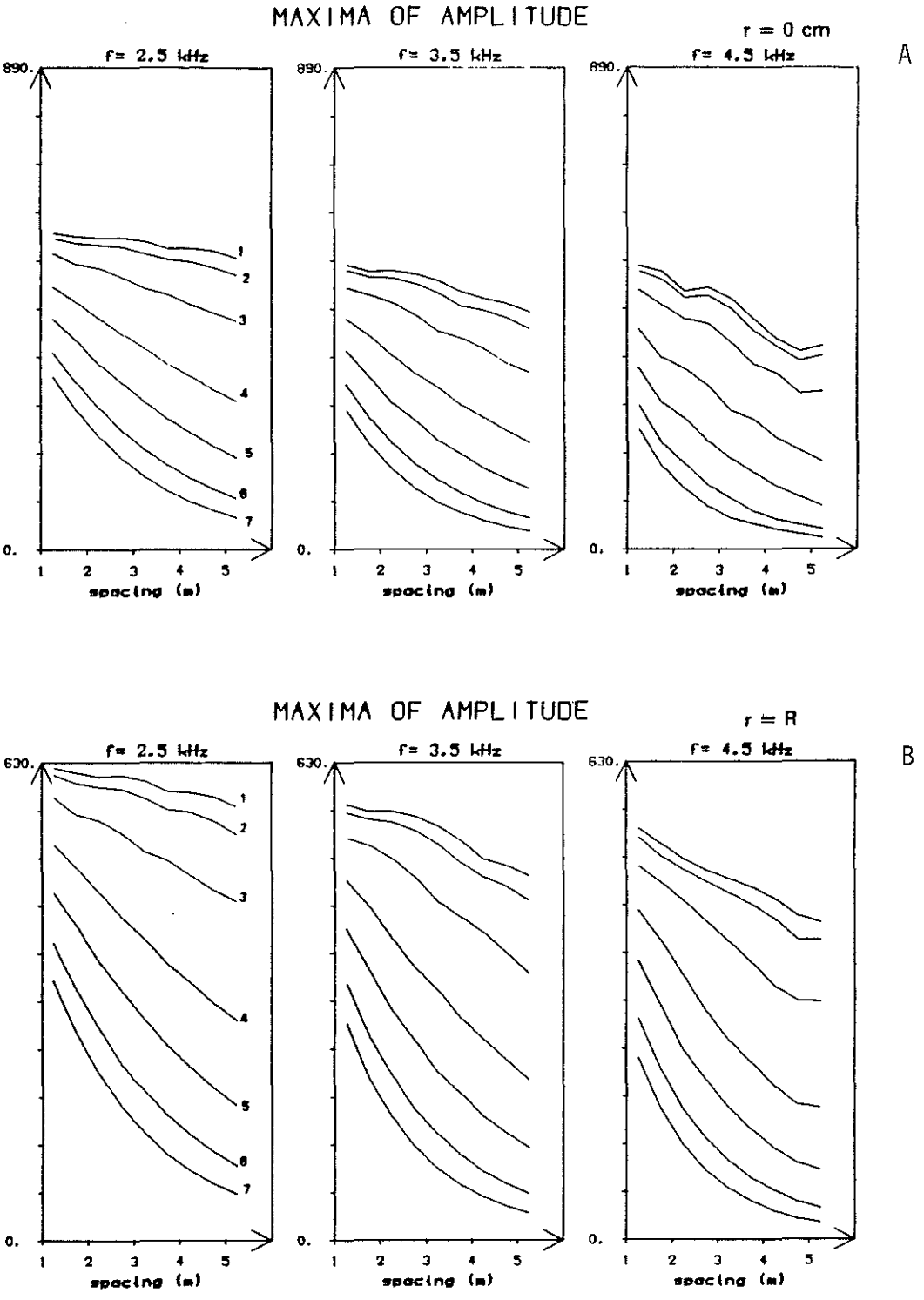

Figure 12: Variation of the maxima of amplitude as a function of the offset of the synthetic microseismograms relative to Figure 9 (A) and Figure 10 (B). f denotes the source center frequency.

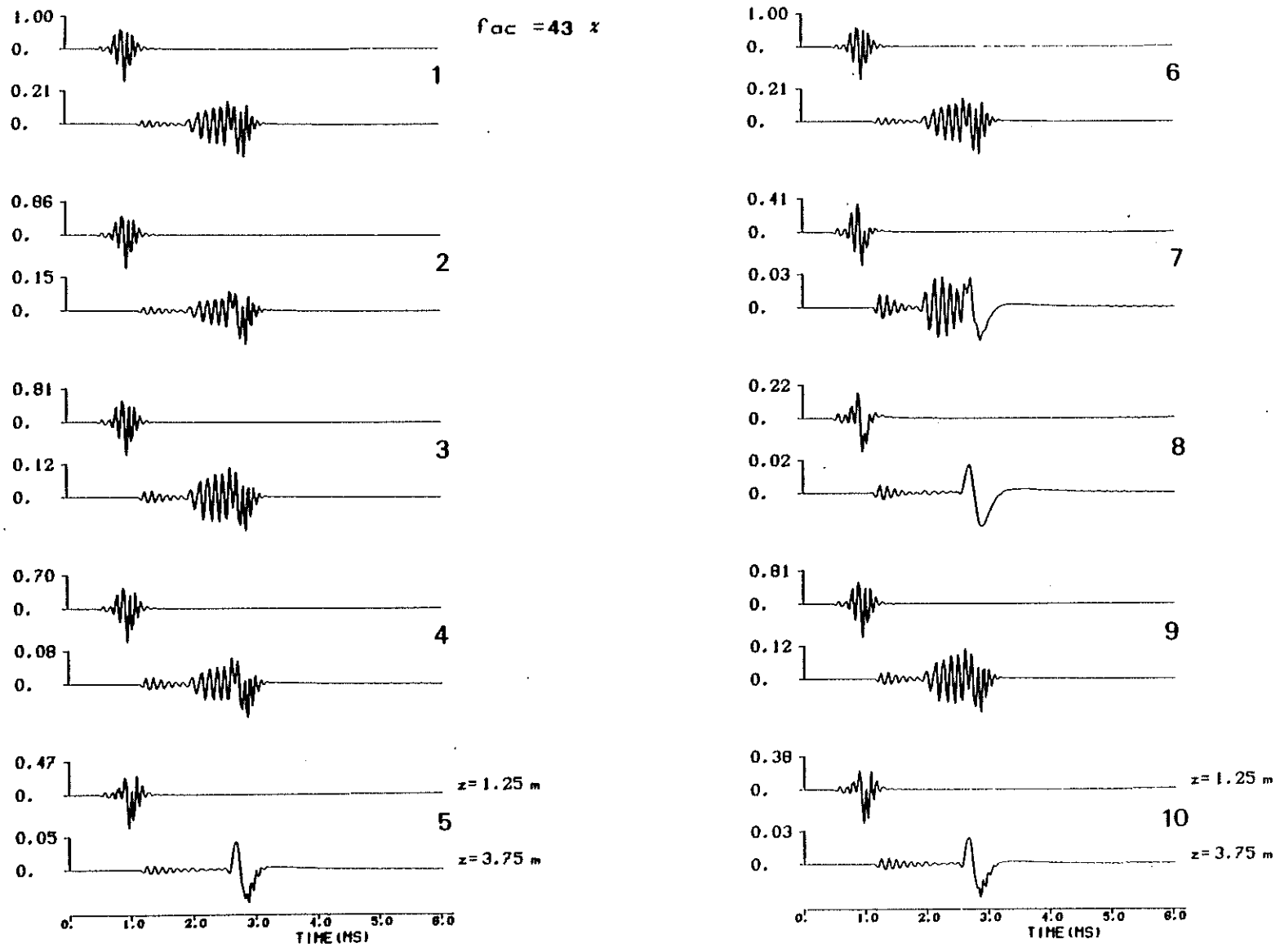

Figure 13: Permeable interface. Effects of intrinsic attenuation in the bore fluid and/or in the matrix in the presence of water saturated Berea sandstone ($\tilde{\phi} = 19\%$, $\tilde{k} = 1$ darcy). The Q values are listed in Table 4. The source center frequency is equal to 7.5 kHz.

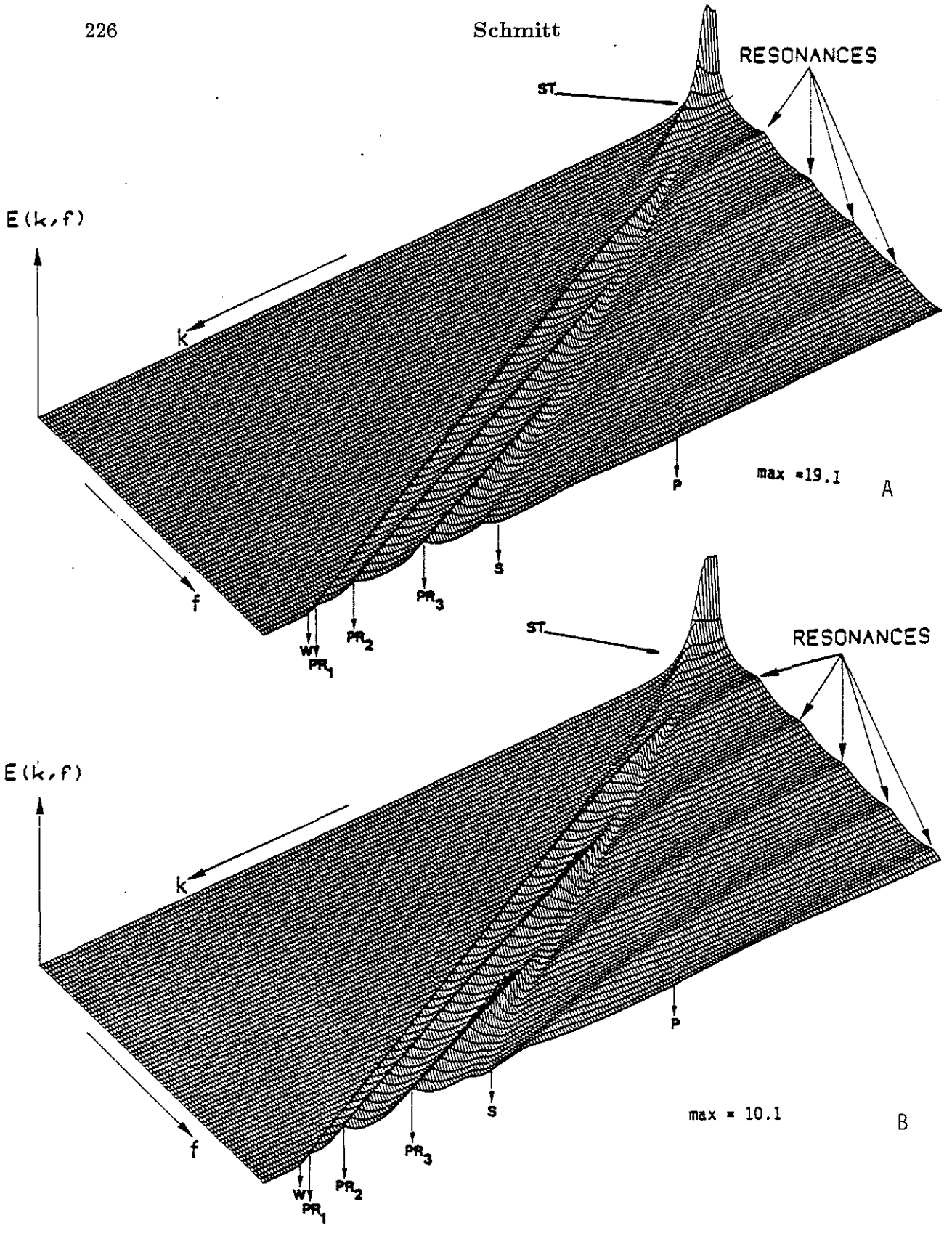

Figure 14: Permeable interface. Spectral energy density diagrams obtained at the center of the borehole (R = 12 cm) in the presence of gas saturated Berea sandstone ($\tilde{\phi} = 19\%$). The permeability is equal to A: 2 md; B: 32.5 md. Each diagram is normalized with respect to its own maximum indicated by max. Compare with Figures 8 A, B.

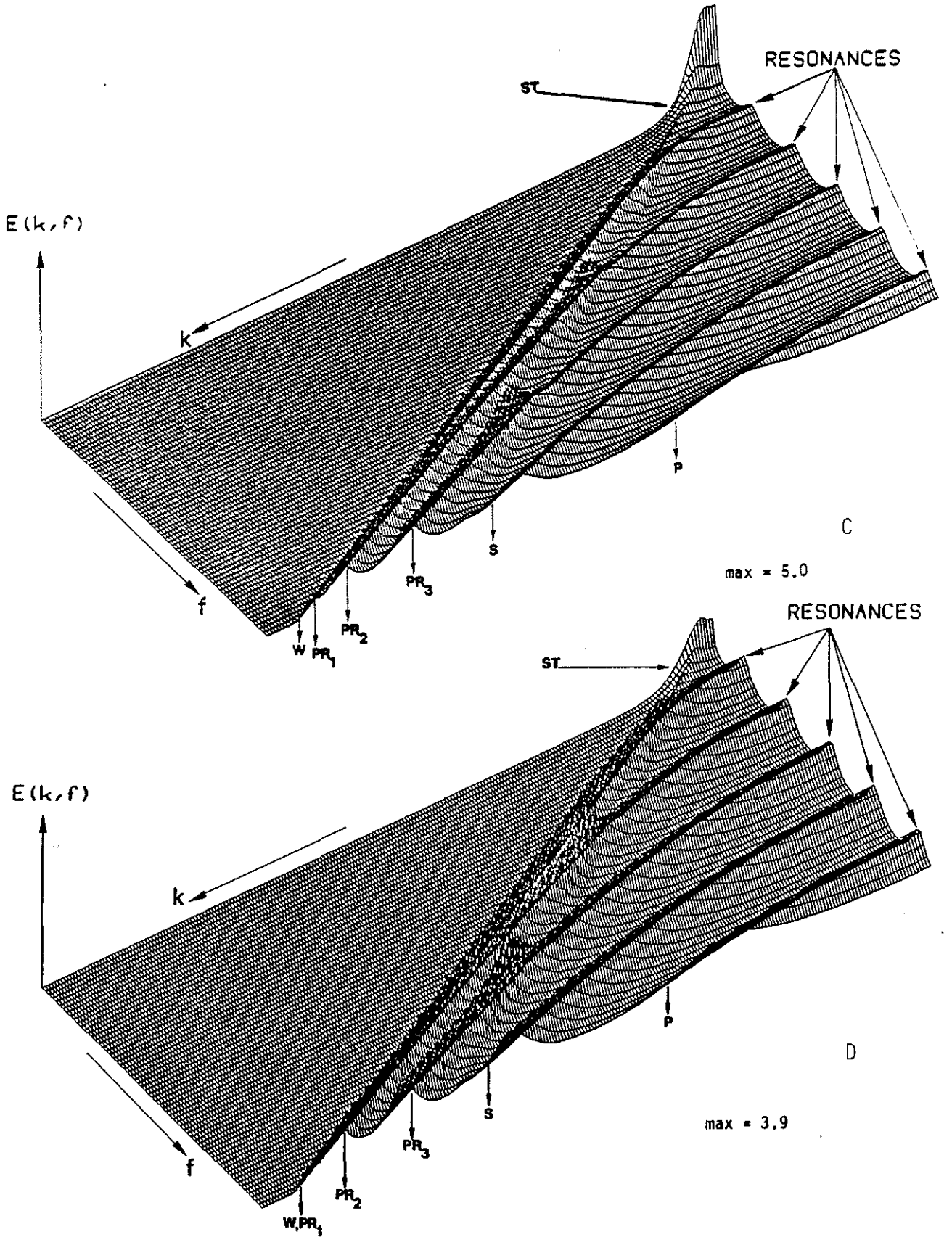

Figure 14: Permeable interface. Spectral energy density diagrams obtained at the center of the borehole (R = 12 cm) in the presence of gas saturated Berea sandstone ($\tilde{\phi} = 19\%$). The permeability is equal to C: 200 md; D: 1 darcy. Each diagram is normalized with respect to its own maximum indicated by max. Compare with Figures 8 A, B and Figures 14 A, B.

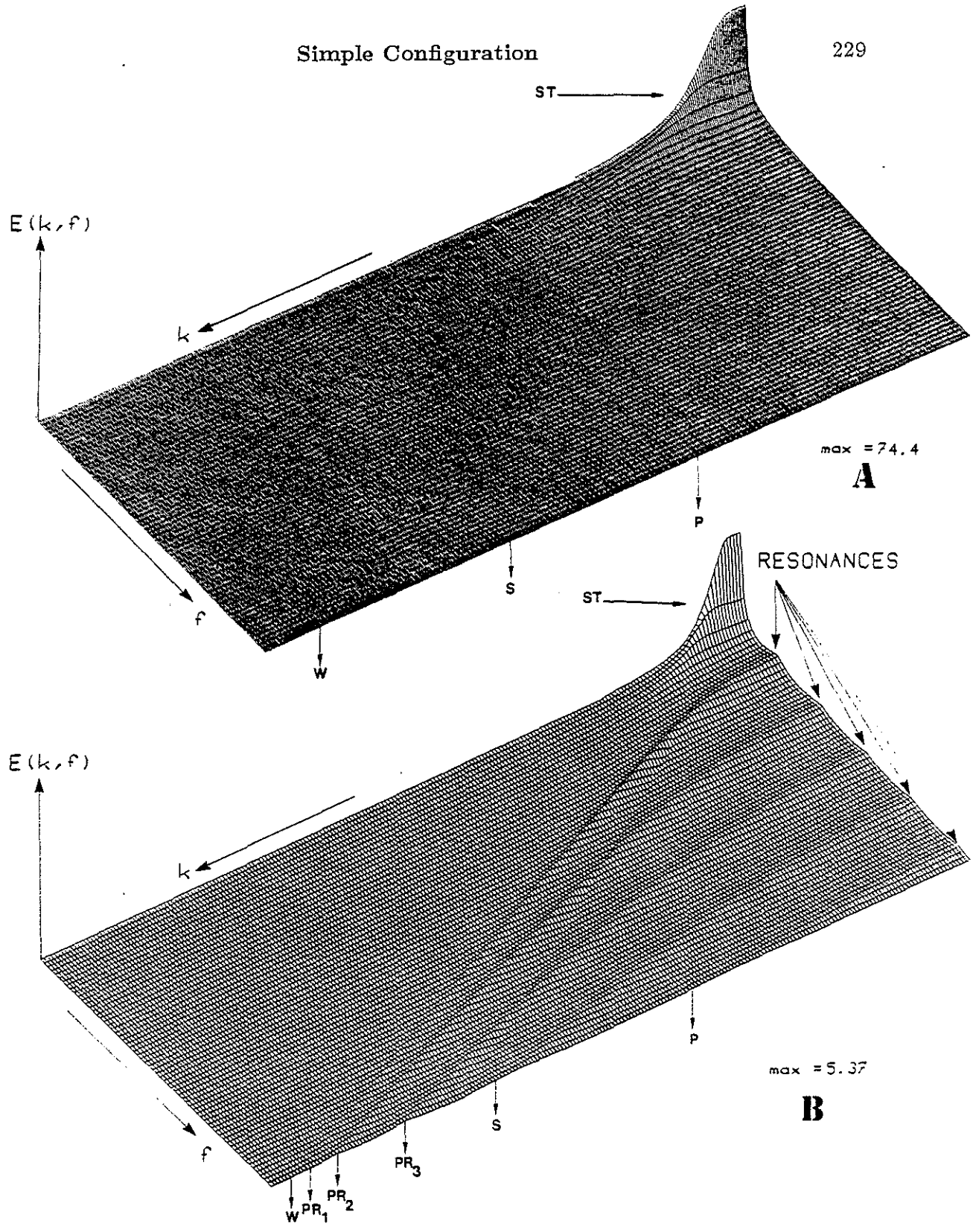

Figure 15: Permeable interface. Spectral energy density diagrams obtained in the presence of gas saturated Berea sandstone ($\tilde{\phi} = 19\%$, $\tilde{k} = 200$ md, R = 12 cm
A: Computation made at the borehole center in the frequency range [0., 5.5] kHz with an axial wavenumber step ten times smaller than usual. The increase in the max value is related to the low frequency Stoneley wave energy. Compare with Figure 14 C.
B: Computation made at the borehole wall with the "usual" frequency range and axial wavenumber step.

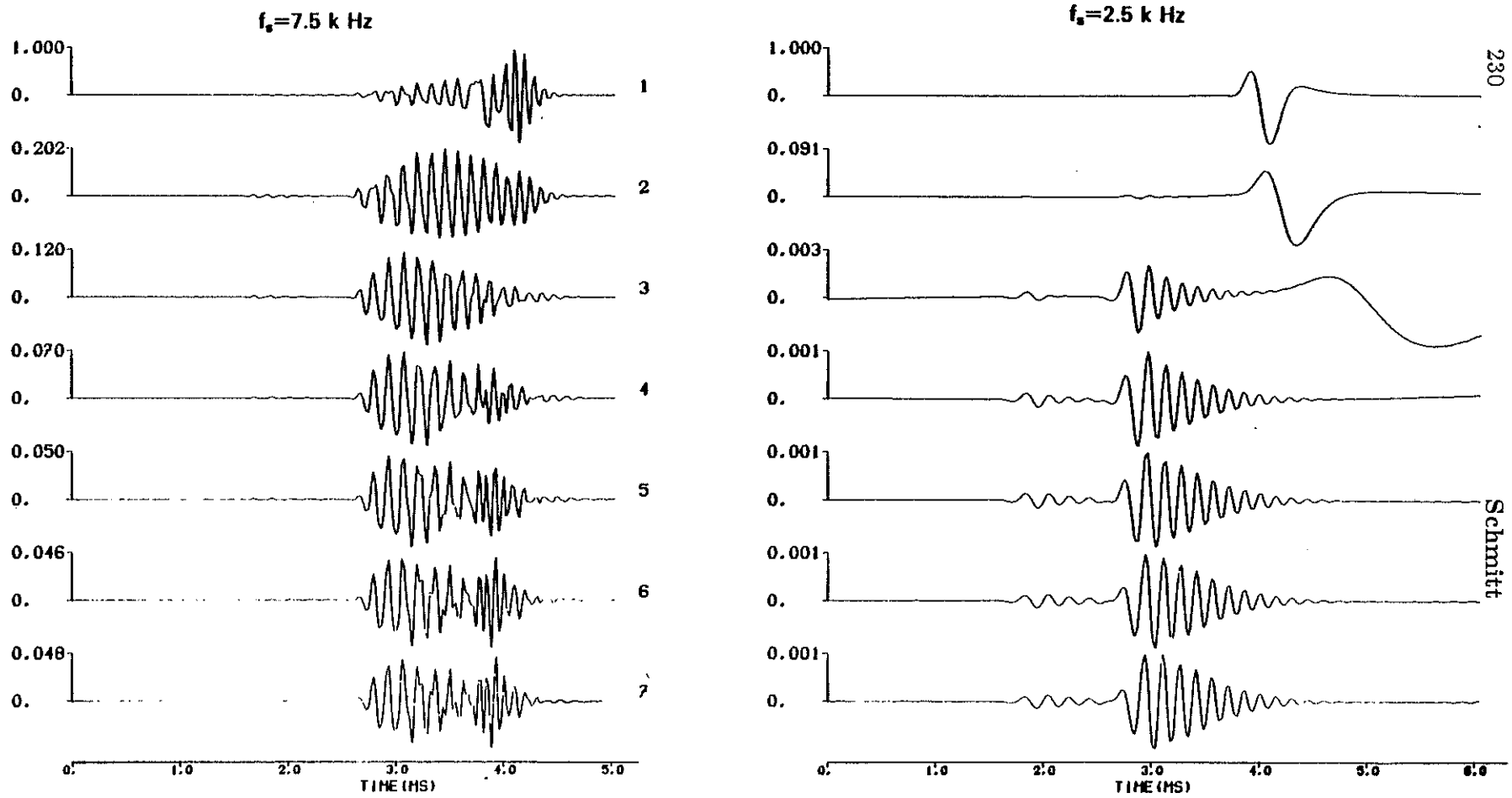

Figure 16: Permeable interface. Permeability effects in the presence of gas saturated Berea sandstone ($\tilde{\phi}$ =19%, R = 12 cm). Iso-offset (5.25 m) comparison of the synthetic microseismograms obtained at the borehole center. f_s denotes the source center frequency. Each series is normalized with respect to its own maximum (1.00). The permeability increases from top to bottom. 1: Elastic, 2: $\tilde{k}$ = 2 md, 3: $\tilde{k}$ = 32.5 md, 4: $\tilde{k}$ = 200 md, 5: $\tilde{k}$ = 500 md, 6: $\tilde{k}$ = 1 darcy, 7: $\tilde{k}$ = 1.5 darcy. Compare with Figure 5.

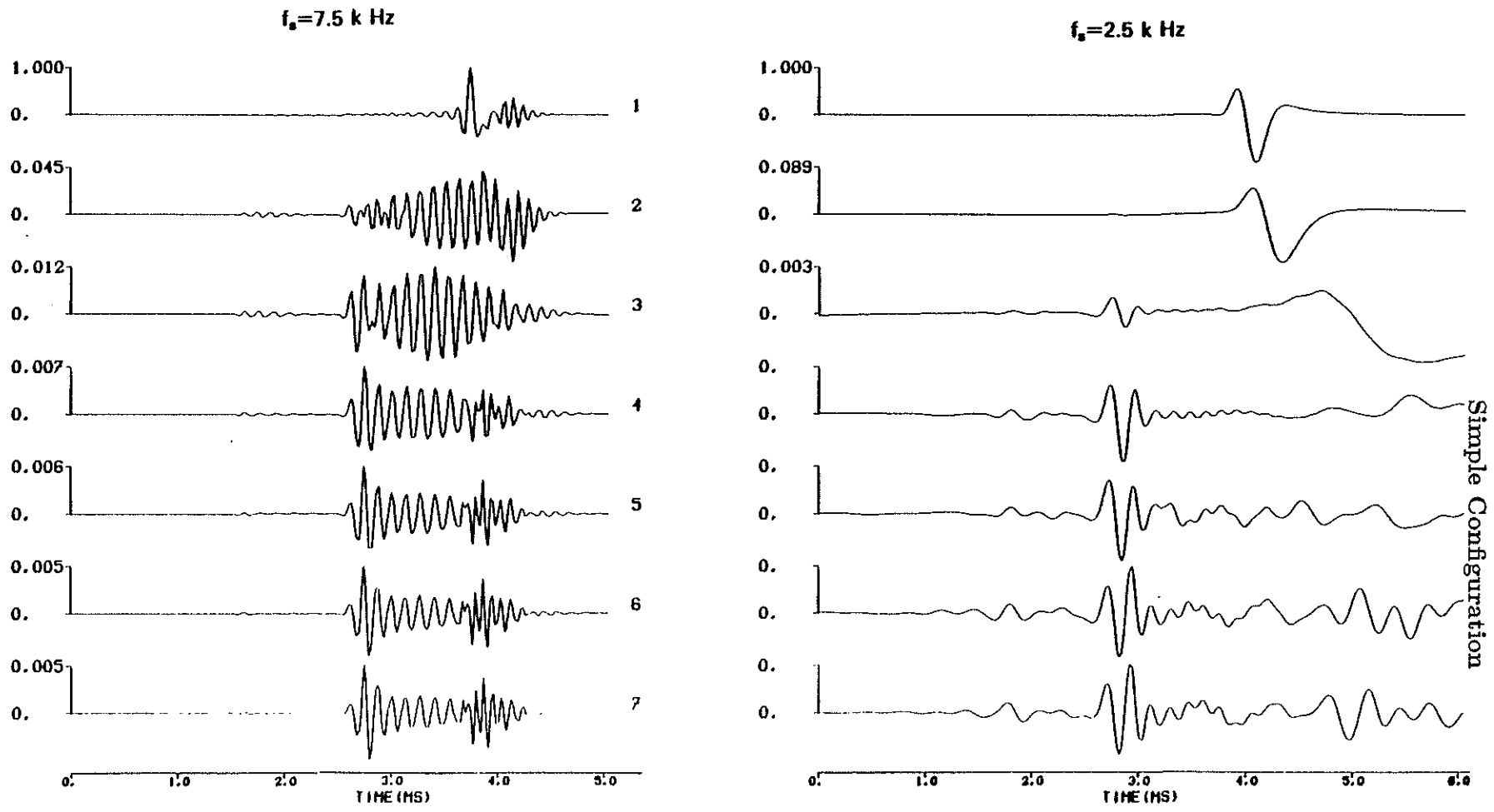

Figure 17: Same as Figure 16 at the borehole wall. Compare with Figure 6.

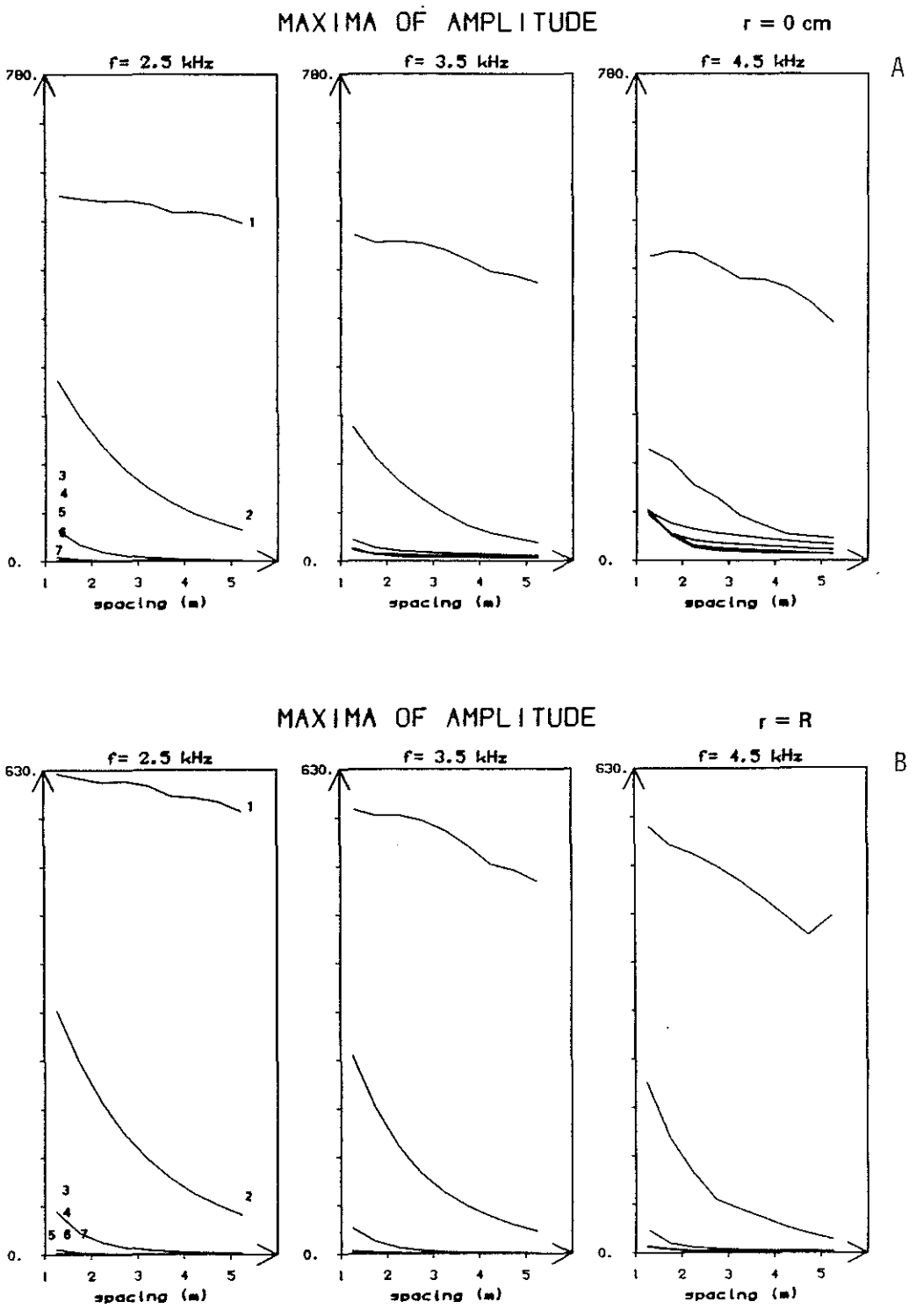

Figure 18: Variation of the maxima of amplitude as a function of the offset of the synthetic microseismograms relative to Figure 16 (A) and Figure 17 (B). f denotes the source center frequency.

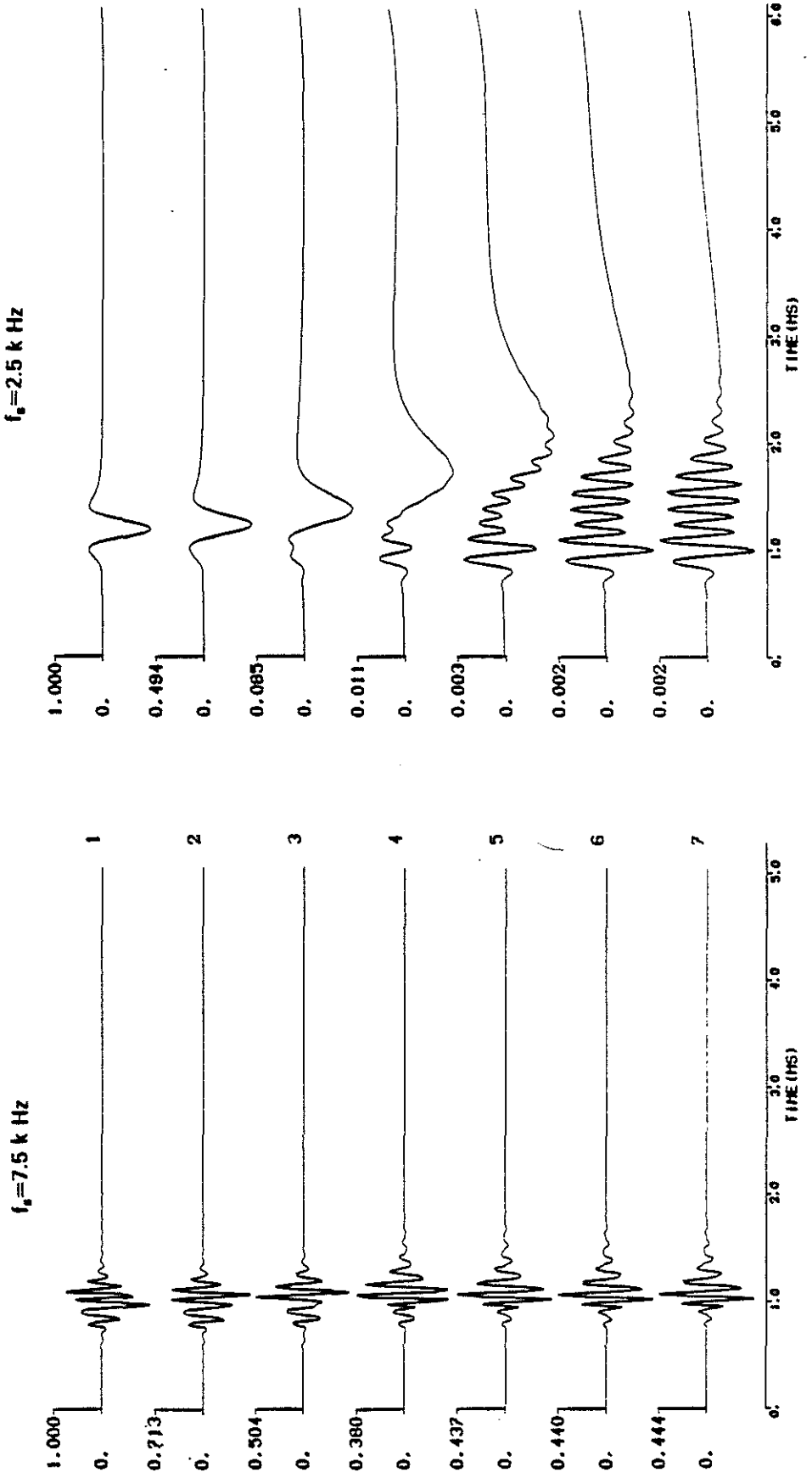

Figure 19: Same as Figure 16 with z = 1.25 m.

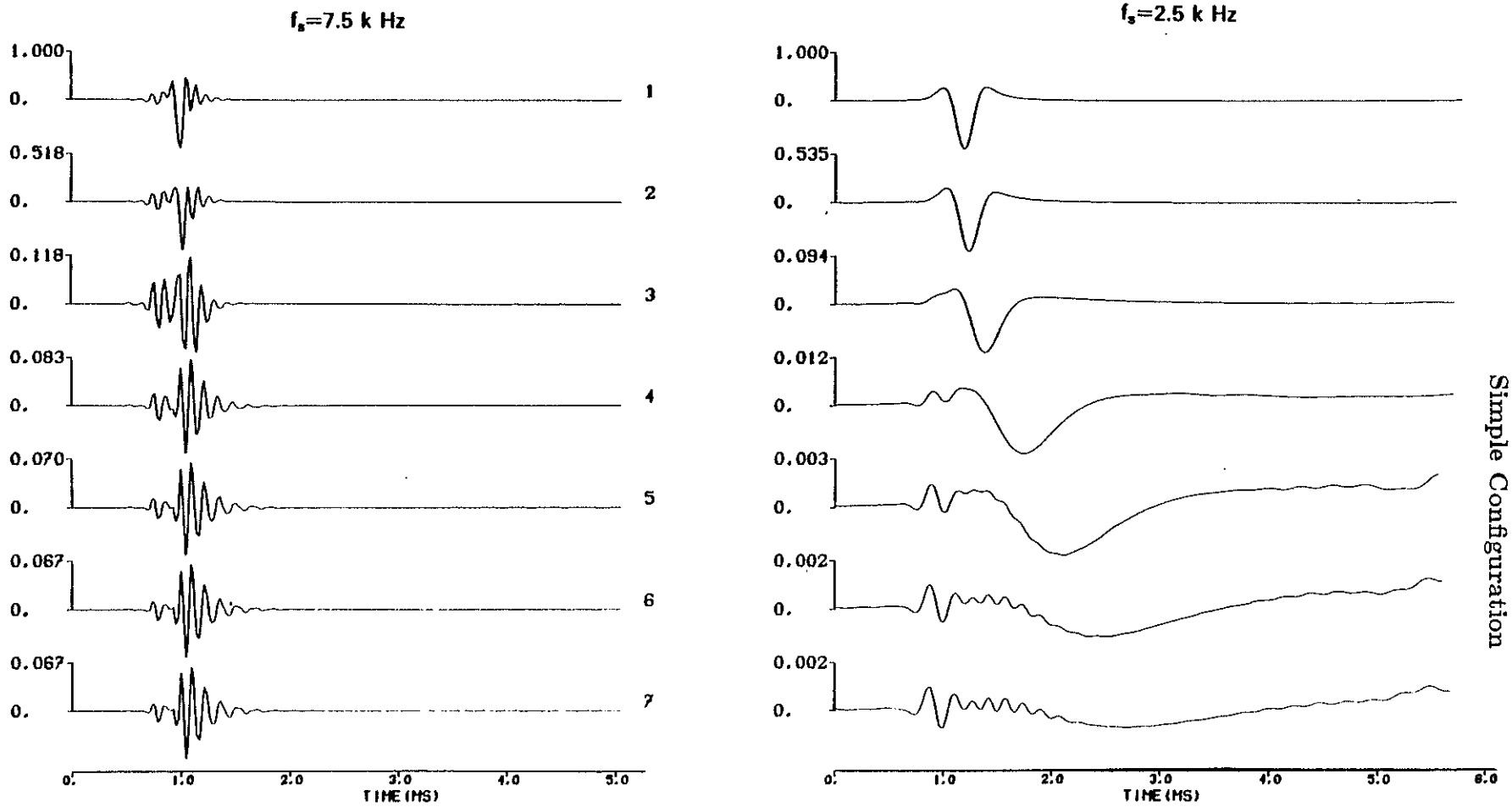

Figure 20: Same as Figure 17 with z = 1.25 m.

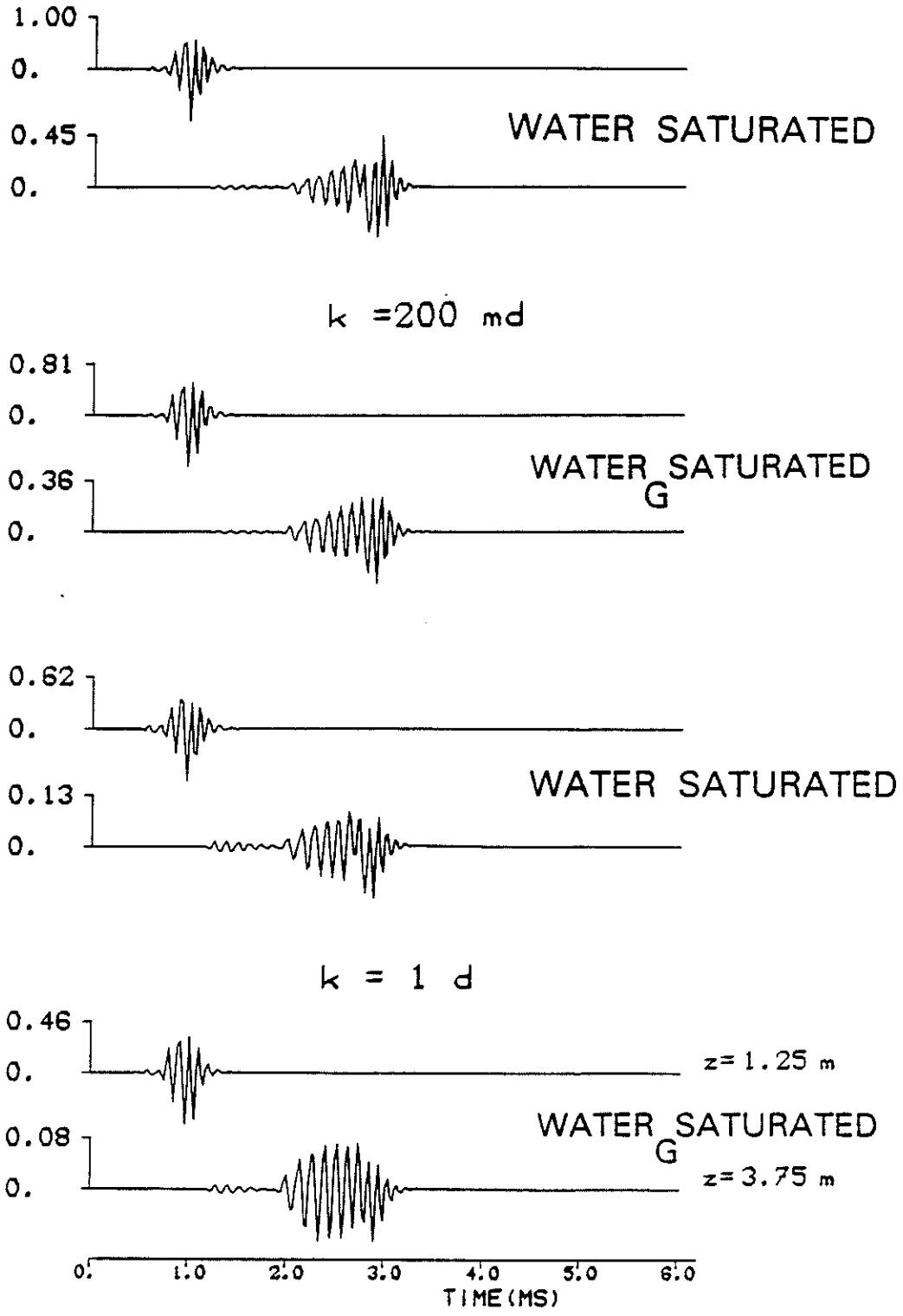

Figure 21: Permeable interface. Permeability and saturant fluid effects in the presence of water and gaseous water (W_G) saturated Berea sandstone ($\tilde{\phi} = 19\%$). R = 12 cm. The source center frequency is equal to 7.5 kHz. A: $\tilde{k} = 200$ md; B: $\tilde{k} = 1$ darcy.

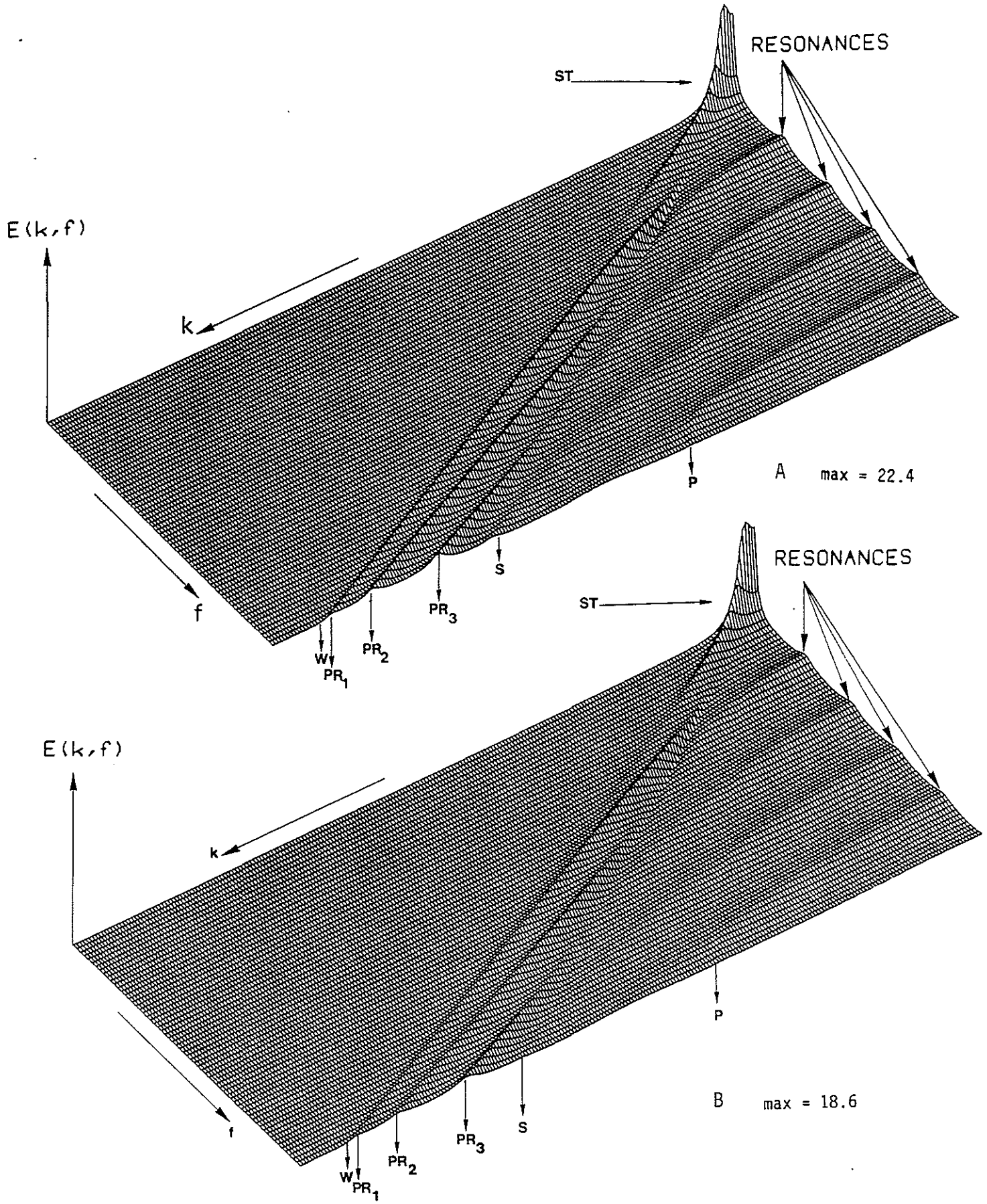

Figure 22: Permeable interface. Spectral energy density diagrams obtained at the borehole center in the presence of gaseous water (W_G) saturated Berea sandstone ($\tilde{\phi}$ = 19%, R =12 cm). A: $\tilde{k}$ = 200 md, B: $\tilde{k}$ = 1 darcy. Compare with Figure 12.

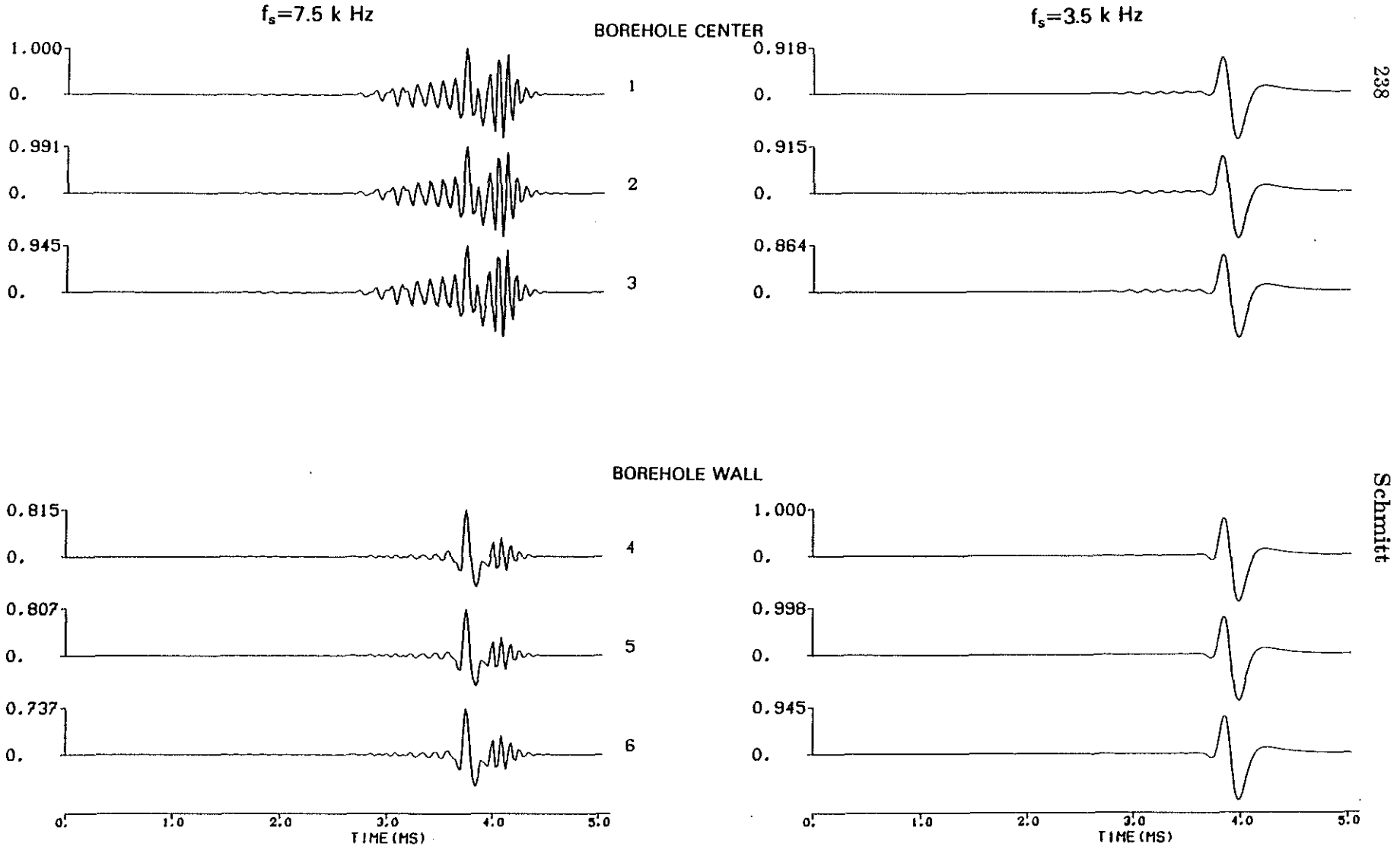

Figure 23: Heavy oil saturated Berea sandstone ($\tilde{\phi} = 19\%$, R = 12 cm). Iso-offset (5.25 m) comparison between the synthetic microseismograms obtained in the presence of the elastic formation (1(4)), the porous formation with an impermeable interface (2(5)), and with a permeable interface (3(6)). f_s denotes the source center frequency. Each series is normalized with respect to its own maximum (1.00).

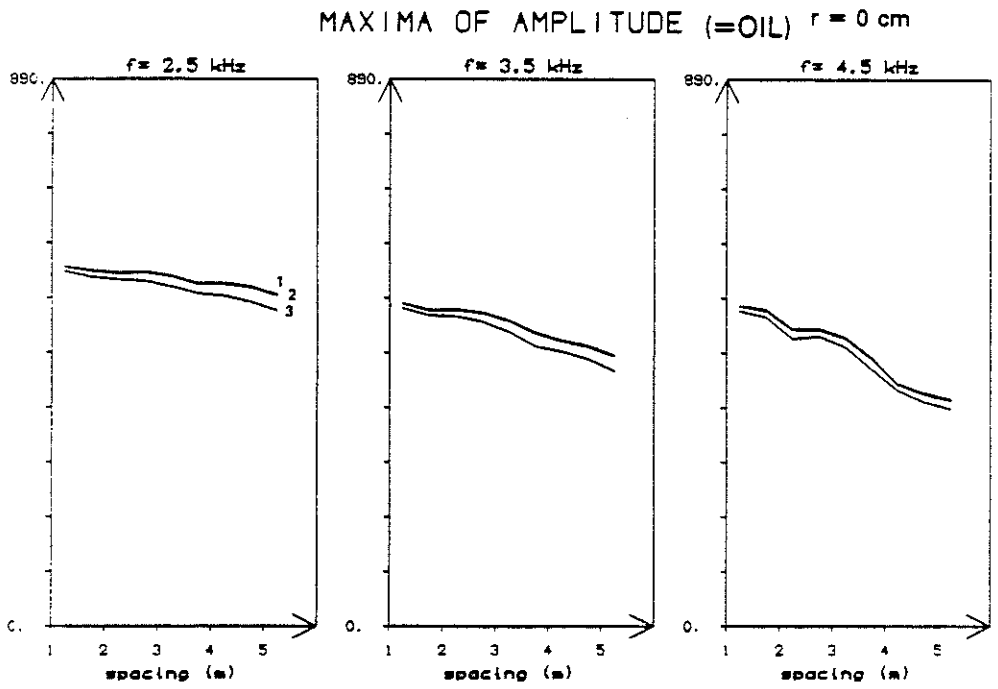

Figure 24: Variation of the maxima of amplitude as a function of the offset of the synthetic microseismograms relative to Figure 23. 1, 2, 3 are the same as in that Figure. f denotes the source center frequency.

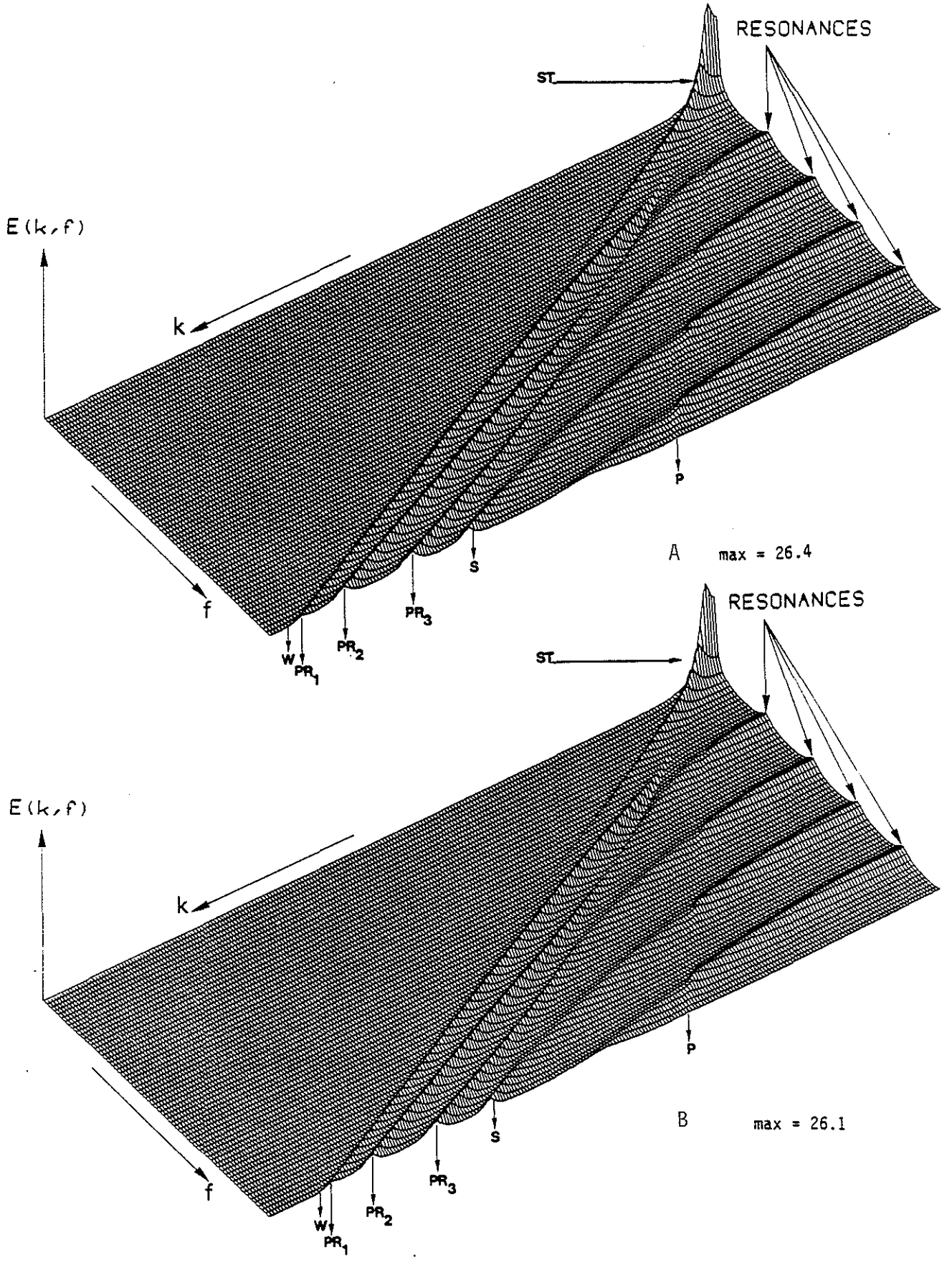

Figure 25: Spectral energy density diagrams obtained at the borehole center in the presence of the equivalent elastic formation (A) and the oil saturated Berea sandstone ($\tilde{\phi}$ = 19%, R = 12 cm) when the interface is permeable. Each diagram is normalized with respect to its own maximum indicated by max.

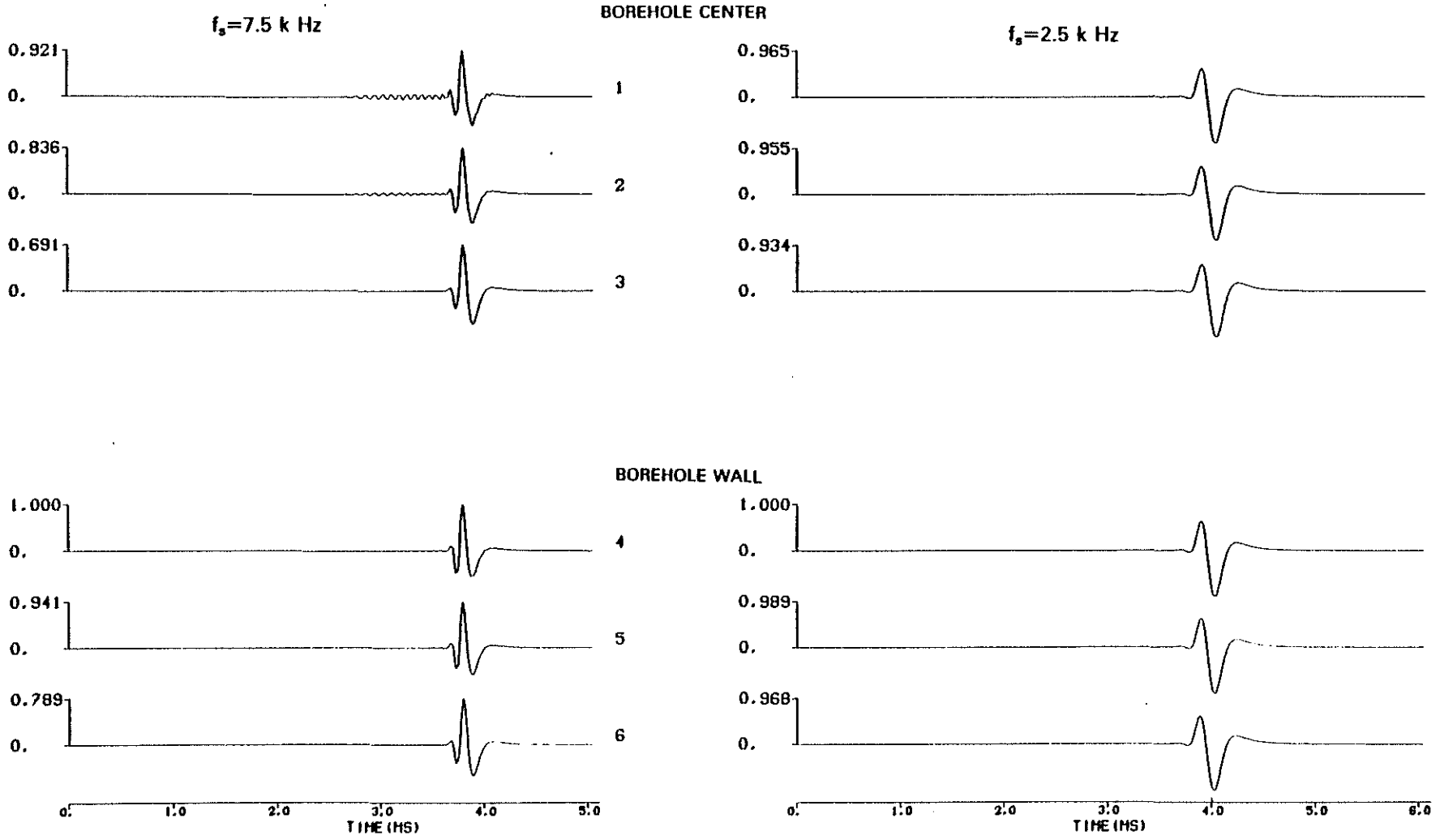

Figure 26: Impermeable interface. Permeability and radius effects in the presence of water saturated Berea sandstone ($\tilde{\phi}$ = 19%, R = 7cm). Iso-offset comparison (5.25 m) of the synthetic microseismograms obtained in the presence of the elastic formation (1(4)), the porous formation with $\tilde{k}$ = 200 md (2(5)) and the porous formation with $\tilde{k}$ = 1 darcy (3(6)). f_s denotes the source center frequency. Each series is normalized with respect to its own maximum (1.00). Compare with Figures 1 and 2.

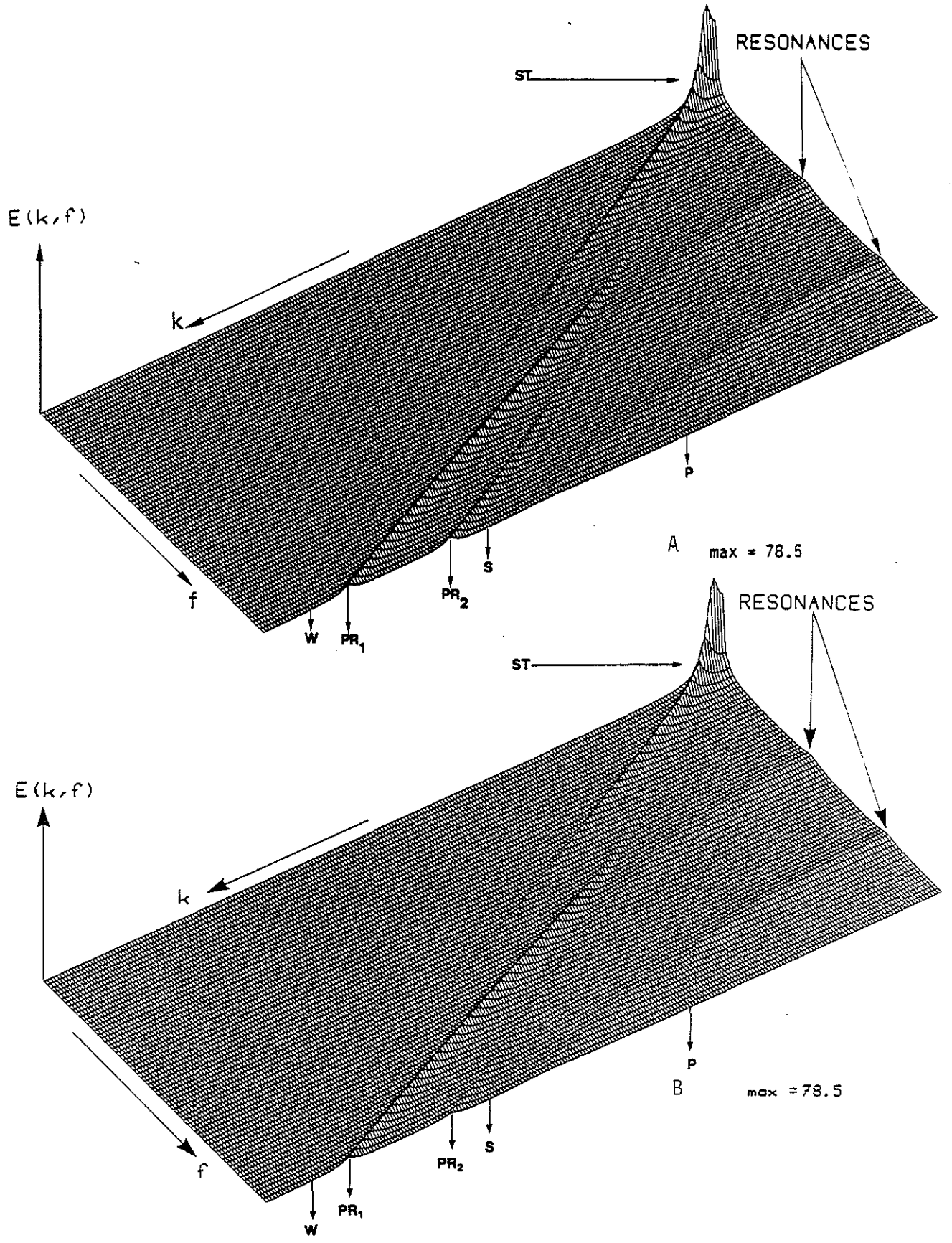

Figure 27: Spectral energy density diagrams obtained at the center of the borehole (R = 7 cm) in the presence of the elastic formation (A) and water saturated Berea sandstone ($\tilde{\phi} = 19\%$, $\tilde{k} = 200$ md) when the interface is impermeable. Each diagram is normalized with respect to its own maximum indicated by max. Compare with Figure 4.

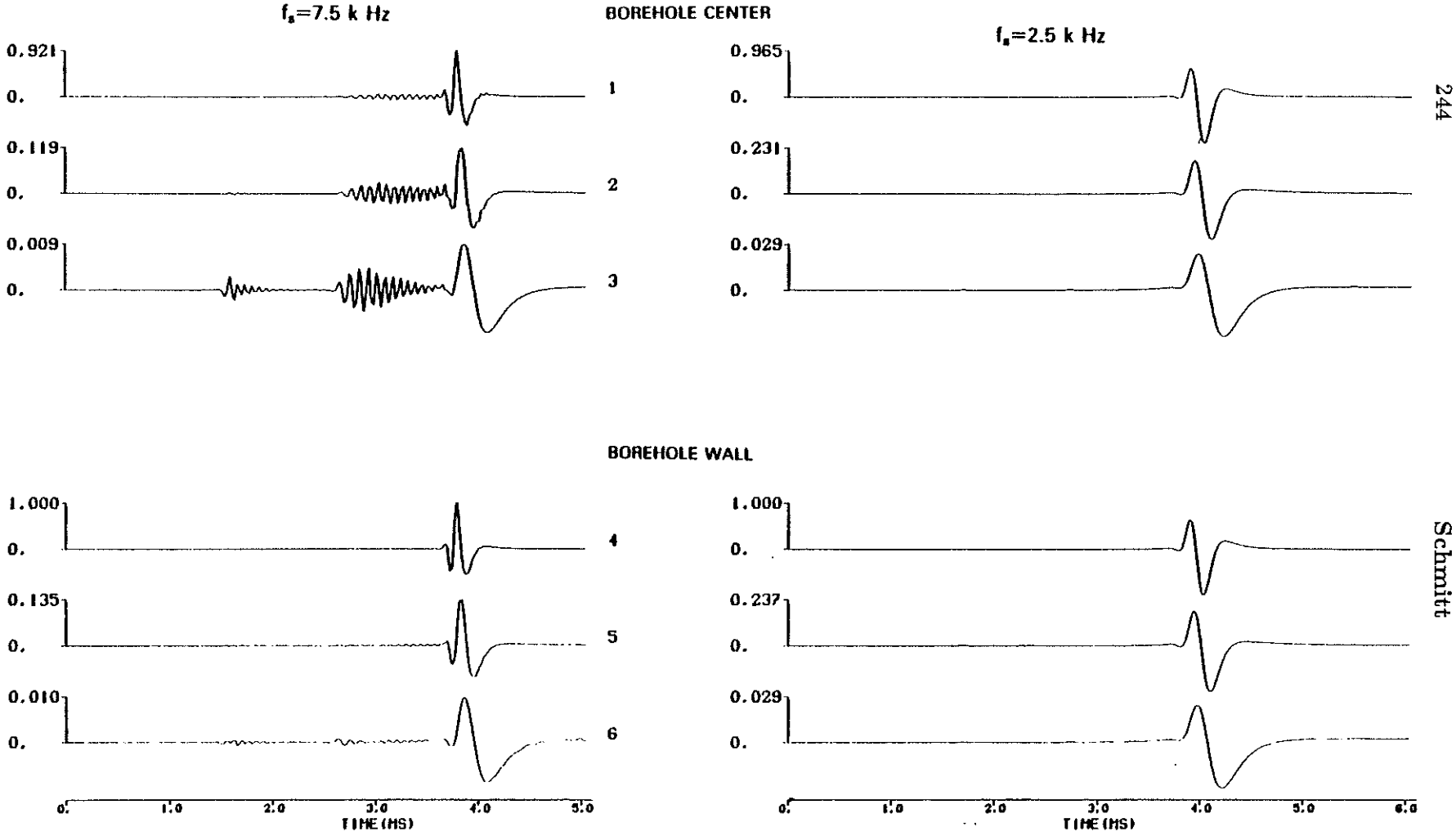

Figure 28: Permeable interface. Permeability and radius effects in the presence of water saturated Berea sandstone ($\tilde{\phi}$ = 19%, R = 7cm). Iso-offset (5.25 m) comparison of the synthetic microseismograms obtained in the presence of the elastic formation (1(4)), the porous formation with $\tilde{k}$ = 200 md (2(5)), and the porous formation with $\tilde{k}$ = 1 darcy (3(6)). f_s denotes the source center frequency. Each series is normalized with respect to its own maximum (1.00). Compare with Figures 9, 10 and 26.

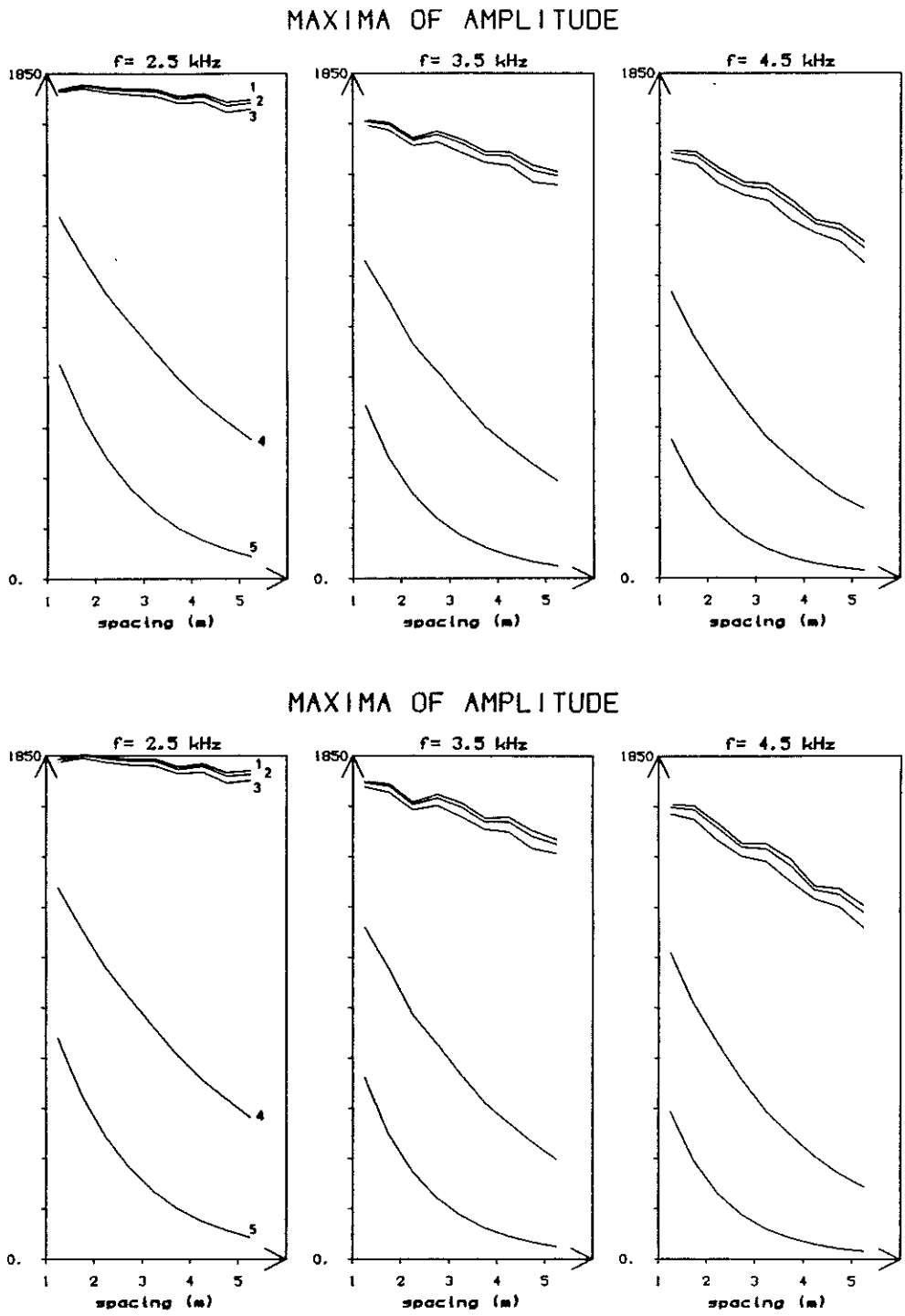

Figure 29: Variation of the maxima of amplitude as a function of the offset of the synthetic microseismograms relative to the Figures 26 and 28. 1: elastic formation, 2: porous formation ($\tilde{k} = 200$ md) with an impermeable borehole wall, 3: porous formation ($\tilde{k} = 1$ darcy) with an impermeable borehole wall, 4: porous formation ($\tilde{k} = 200$ md) with a permeable borehole wall, 5: porous formation ($\tilde{k} = 1$ darcy) with a permeable borehole wall, Compare with Figures 3 and 12.

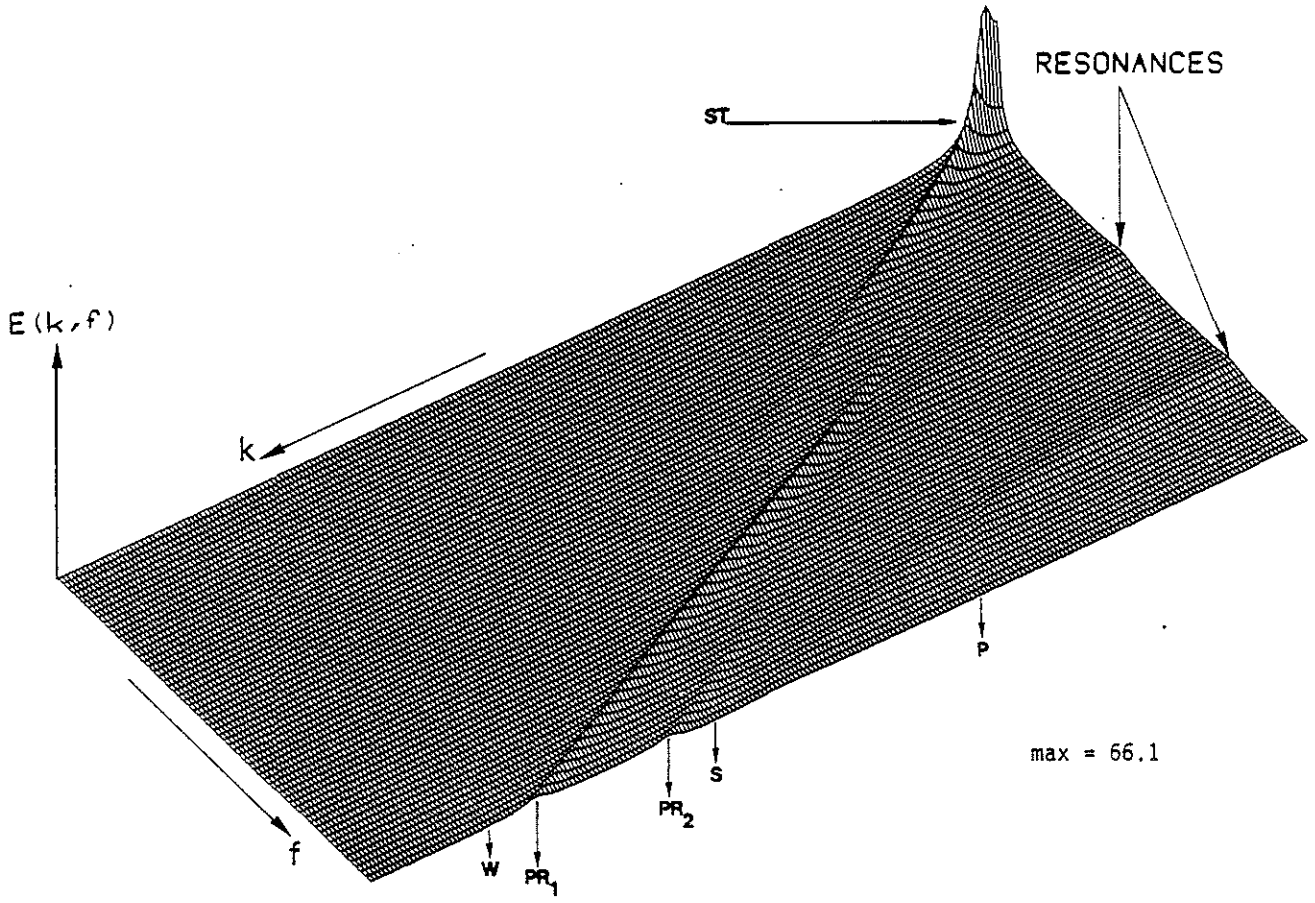

Figure 30: Spectral energy density diagram obtained at the center of the borehole (R = 7 cm) in the presence of water saturated sandstone ($\tilde{\phi} = 19\%$, $\tilde{k} = 200$ md) when the fluid flow is free. Compare with Figures 27.

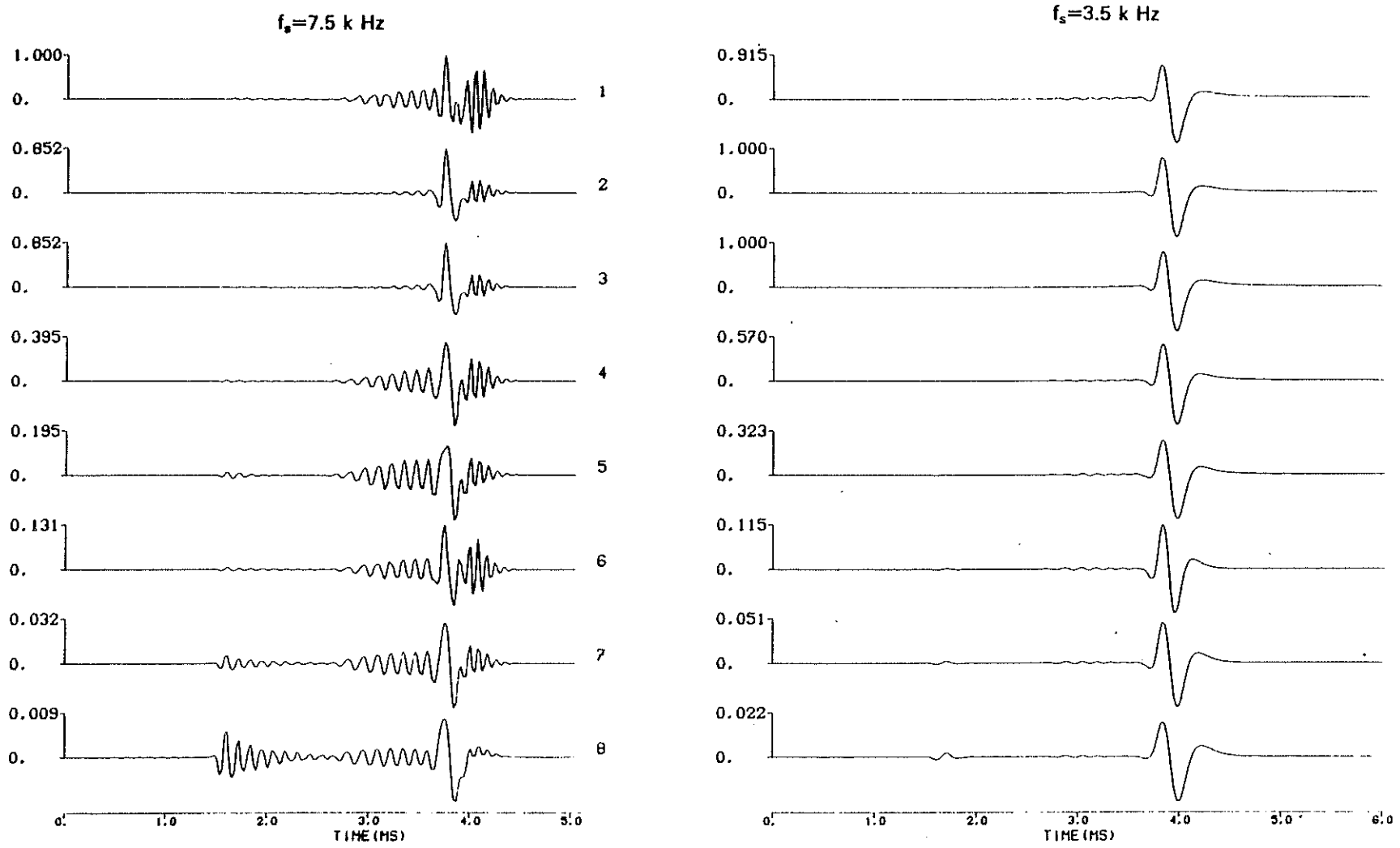

Figure 31: Impermeable interface. Water saturated sandstone ($\tilde{\phi} = 19\%$, $\tilde{k} = 200$ md). R = 12 cm. Radial variation of the wavefield with a 5.25 m offset. f_s denotes the source center frequency. Each series is normalized with respect to its own maximum (1.00). 1= $P_1(r = 0)$; 2= $P_1(r = R)$; 3= - $\sigma_2 + s_2(r = R)$; 4= - $\sigma_2 + s_2(r = R + 6\,\text{cm})$; 5= - $\sigma_2 + s_2(r = R + 12\,\text{cm})$; 6= - $s_2(r = R)/\tilde{\phi}_2$; 7= - $s_2(r = R + 6\,\text{cm})/\tilde{\phi}_2$; 8= - $s_2(r = R + 12\,\text{cm})/\tilde{\phi}_2$.

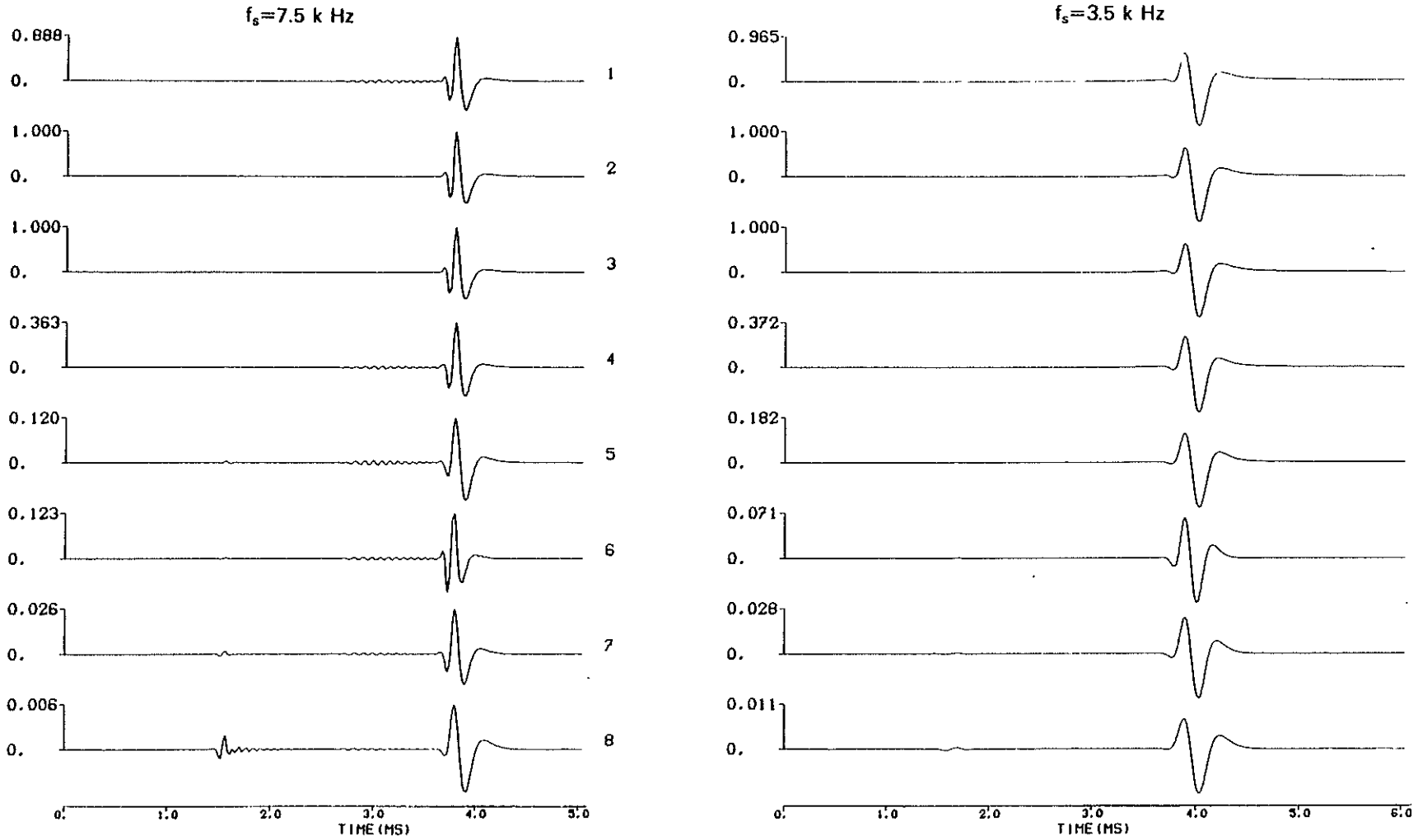

Figure 32: Same as Figure 31 when R = 7 cm.

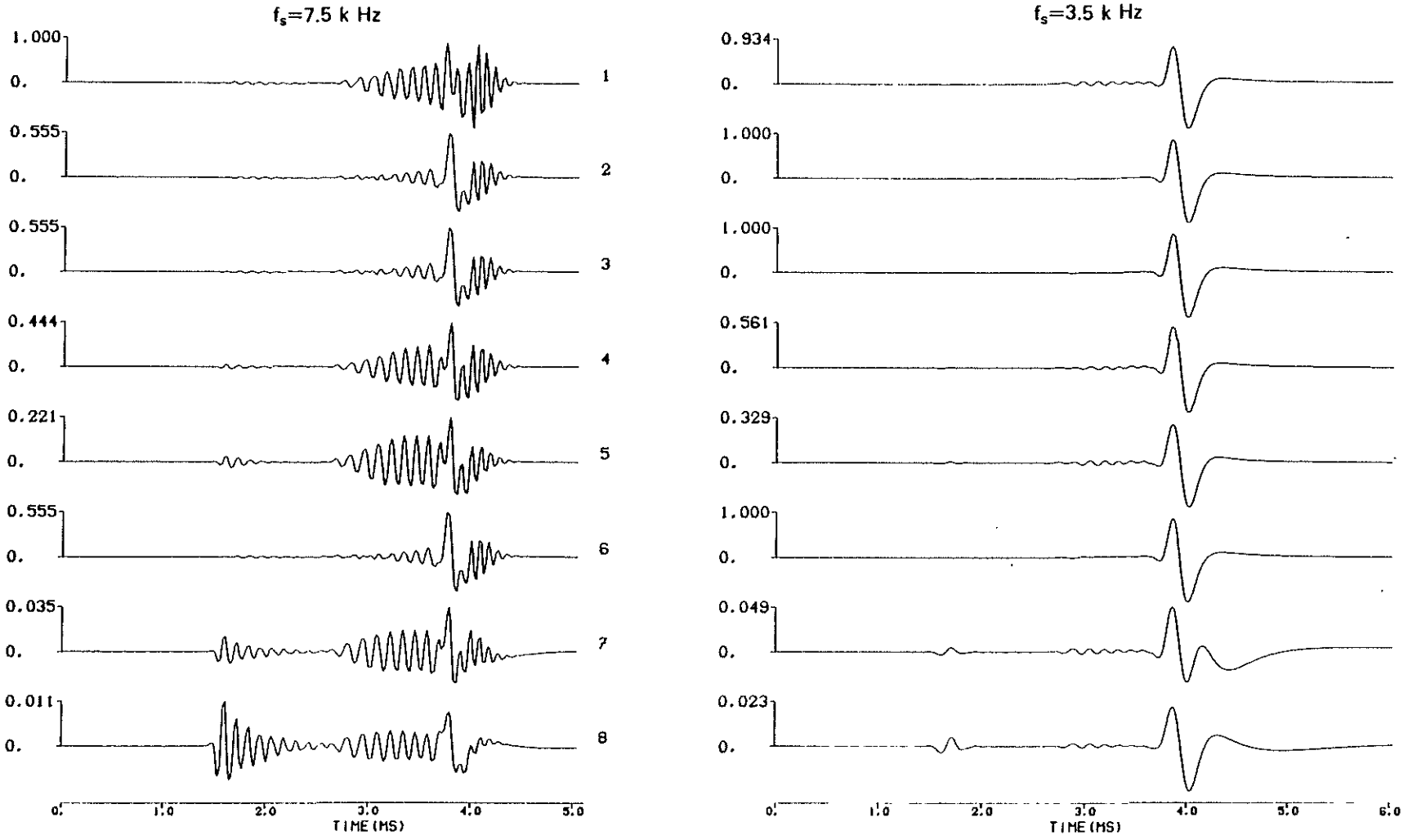

Figure 33: Permeable interface. Water saturated sandstone ($\tilde{\phi}$ = 19%, $\tilde{k}$ = 200 md). R = 12 cm. Radial variation of the wavefield with a 5.25 m offset. f_s denotes the source center frequency. Each series is normalized with respect to its own maximum (1.00). 1= $P_1(r=0)$; 2= $P_1(r=R)$; 3= - $\sigma_2 + s_2(r=R)$; 4= - $\sigma_2 + s_2(r = R + 6\,\text{cm})$; 5= - $\sigma_2 + s_2(r = R + 12\,\text{cm})$; 6= - $s_2(r=R)/\tilde{\phi}_2$; 7= - $s_2(r = R + 6\,\text{cm})/\tilde{\phi}_2$; 8= - $s_2(r = R + 12\,\text{cm})/\tilde{\phi}_2$.

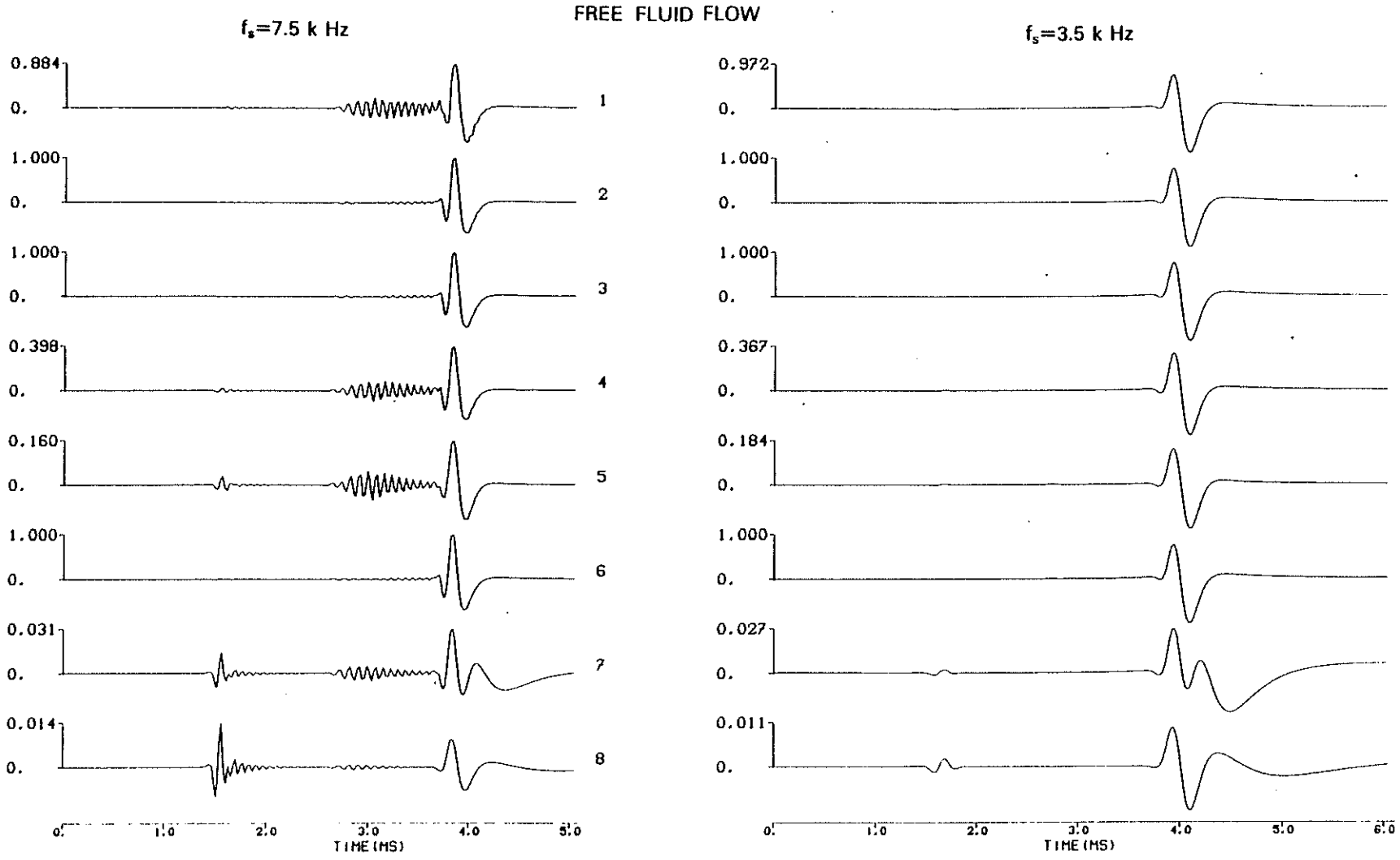

Figure 34: Same as Figure 33 with R = 7 cm.

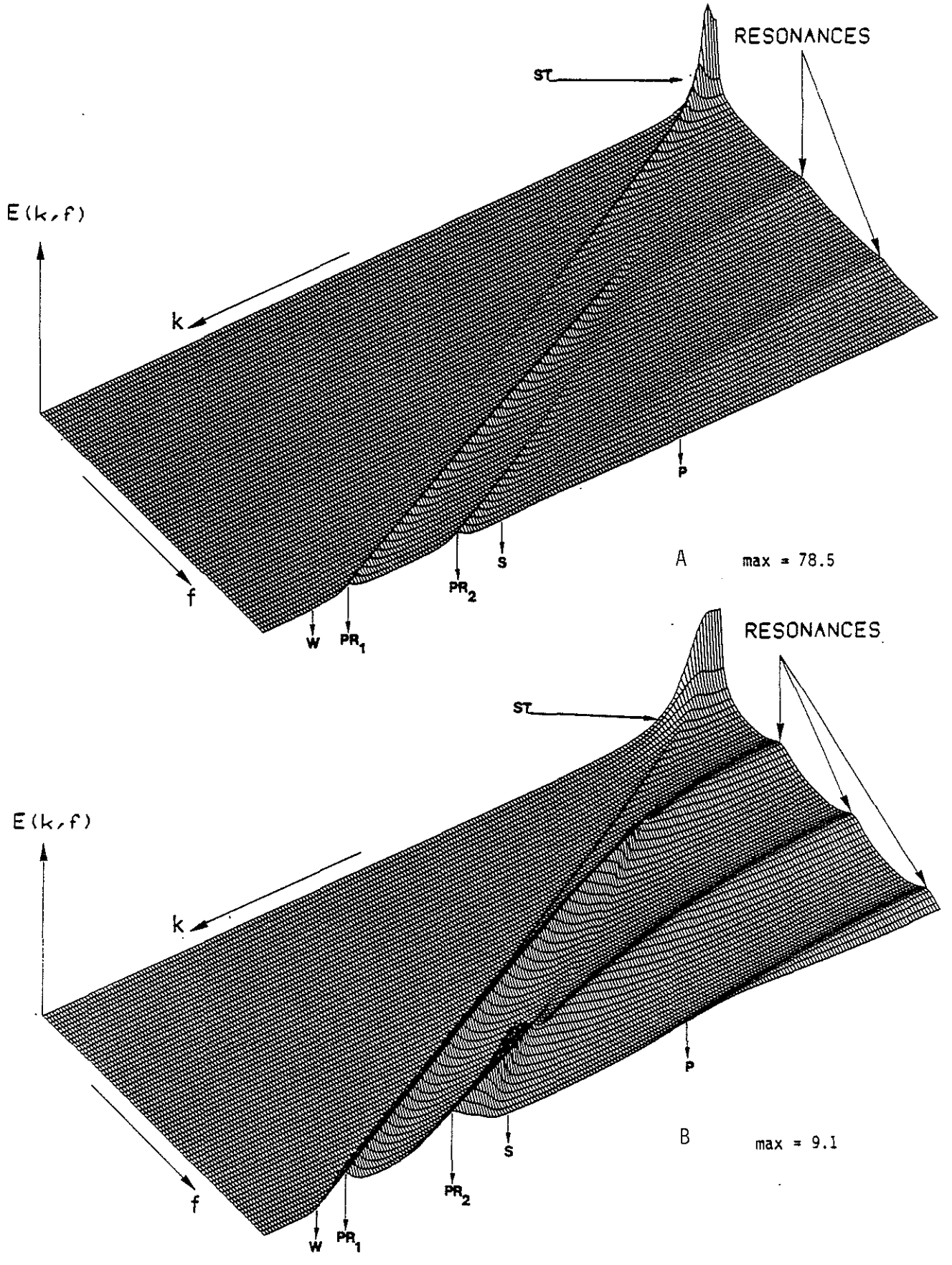

Figure 35: Spectral energy density diagrams obtained at the center of the borehole (R = 7 cm) in the presence of the equivalent elastic formation and gas saturated Berea sandstone ($\tilde{\phi} = 19\%$, $\tilde{k} = 200$ md) when the fluid flow is free. Each diagram is normalized with respect to its own maximum indicated by max. Compare with Figures 8 and 14.

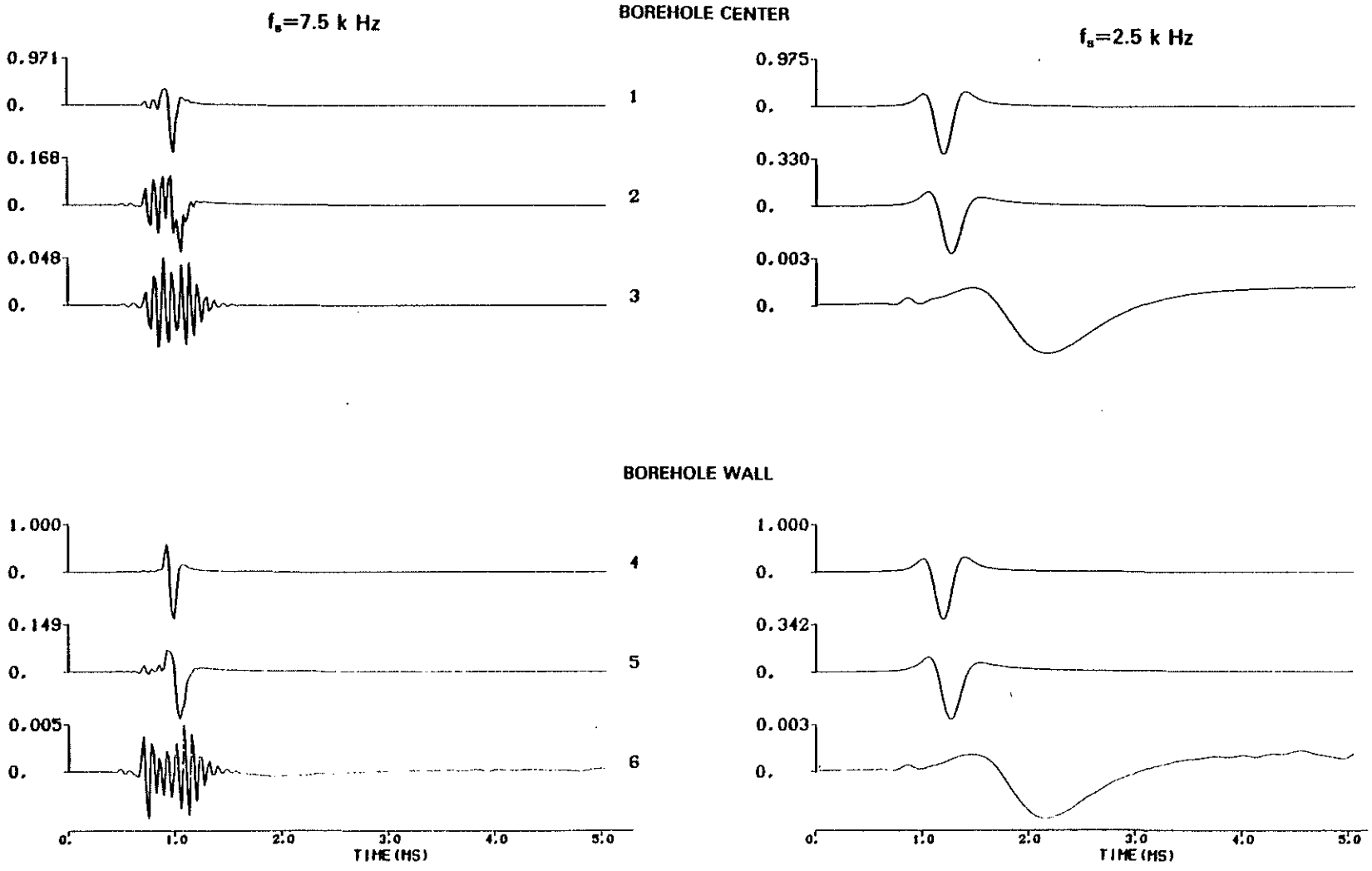

Figure 36: Permeable interface. Permeability and radius effects in the presence of gas saturated Berea sandstone ($\tilde{\phi}$ = 19%, R = 7 cm). Iso-offset (1.25 m) comparison obtained in the presence of the elastic formation (1(4)), the porous formation with $\tilde{k}$ = 2 md (2(4)), and the porous formation with $\tilde{k}$ = 200 md (3(6)). f_s denotes the source center frequency. Each series is normalized with respect to its own maximum.

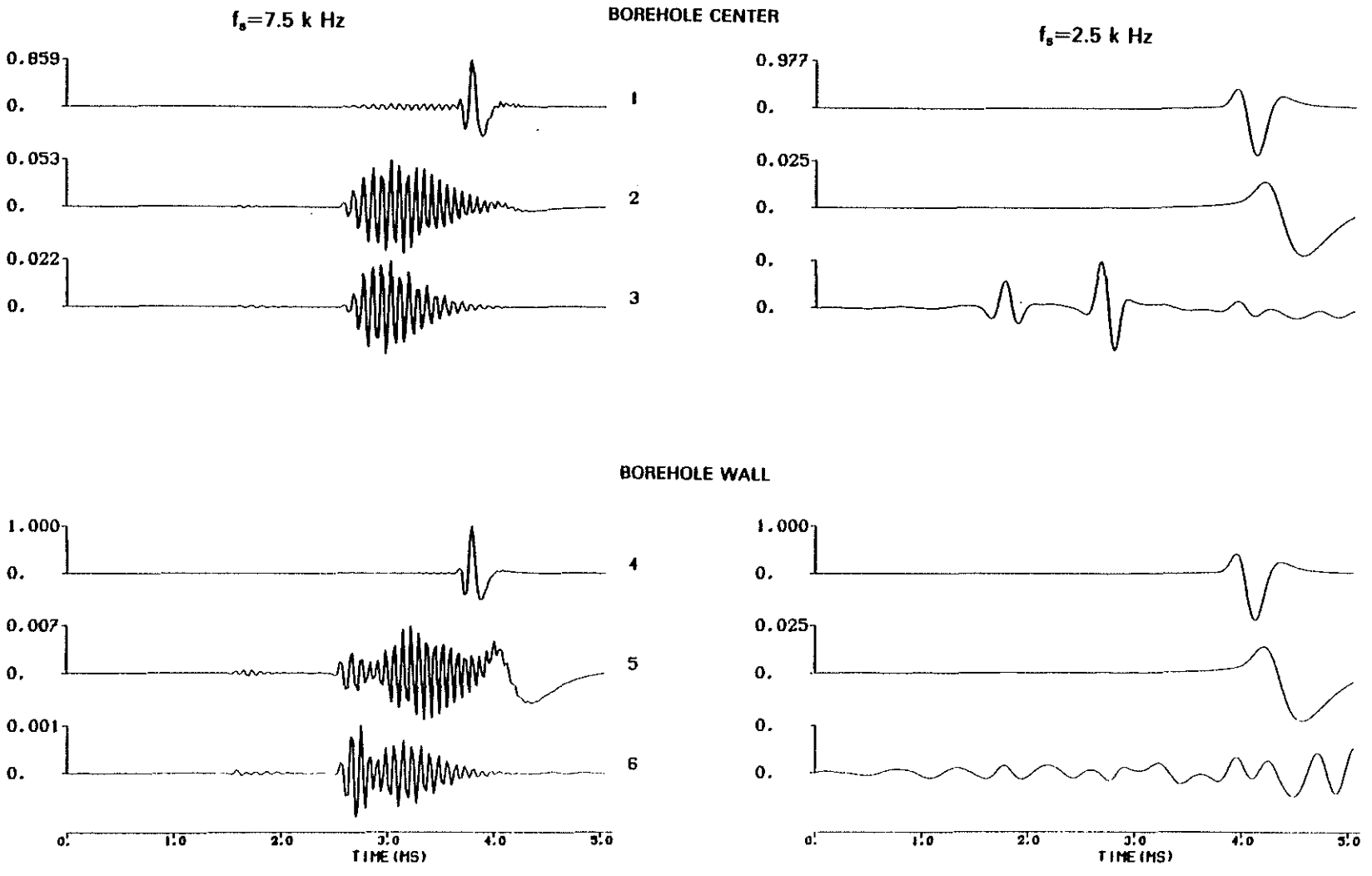

Figure 37: Same as Figure 36 with an offset equal to 5.25 m.

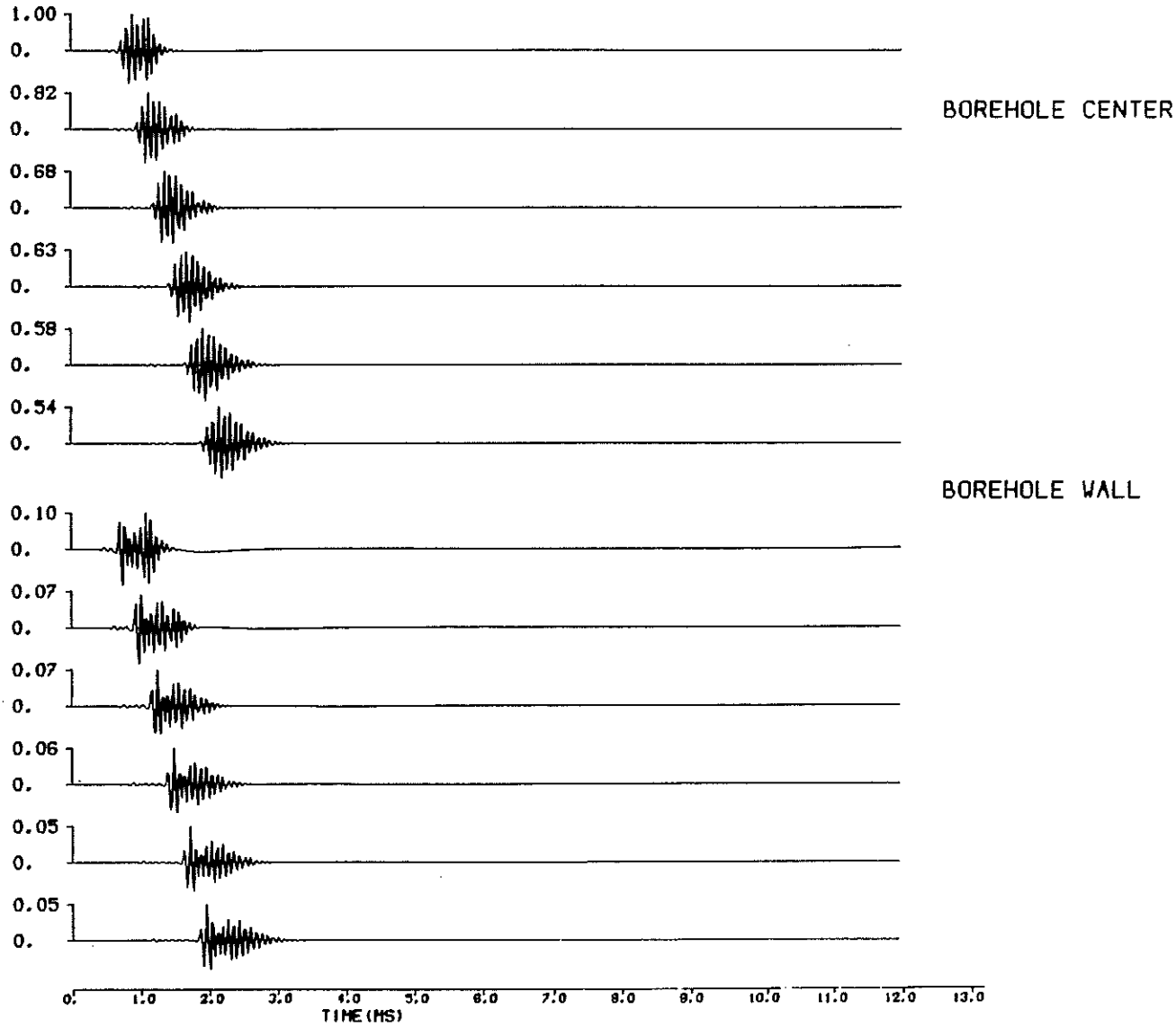

Figure 38: Permeable interface. Synthetic microseismograms obtained in the presence of gas saturated Berea sandstone ($\tilde{\phi} = 19\%$, $\tilde{k} = 200$ md, R = 7 cm). The offset vary from 1.25 m to 3.75 m by steps of 0.5m. The source center frequency is equal to 7.5 kHz. 256 frequencies have been considered so that the frequency step is identical to that used for the previous calculations. Each waveform is normalized with respect to its own maximum.

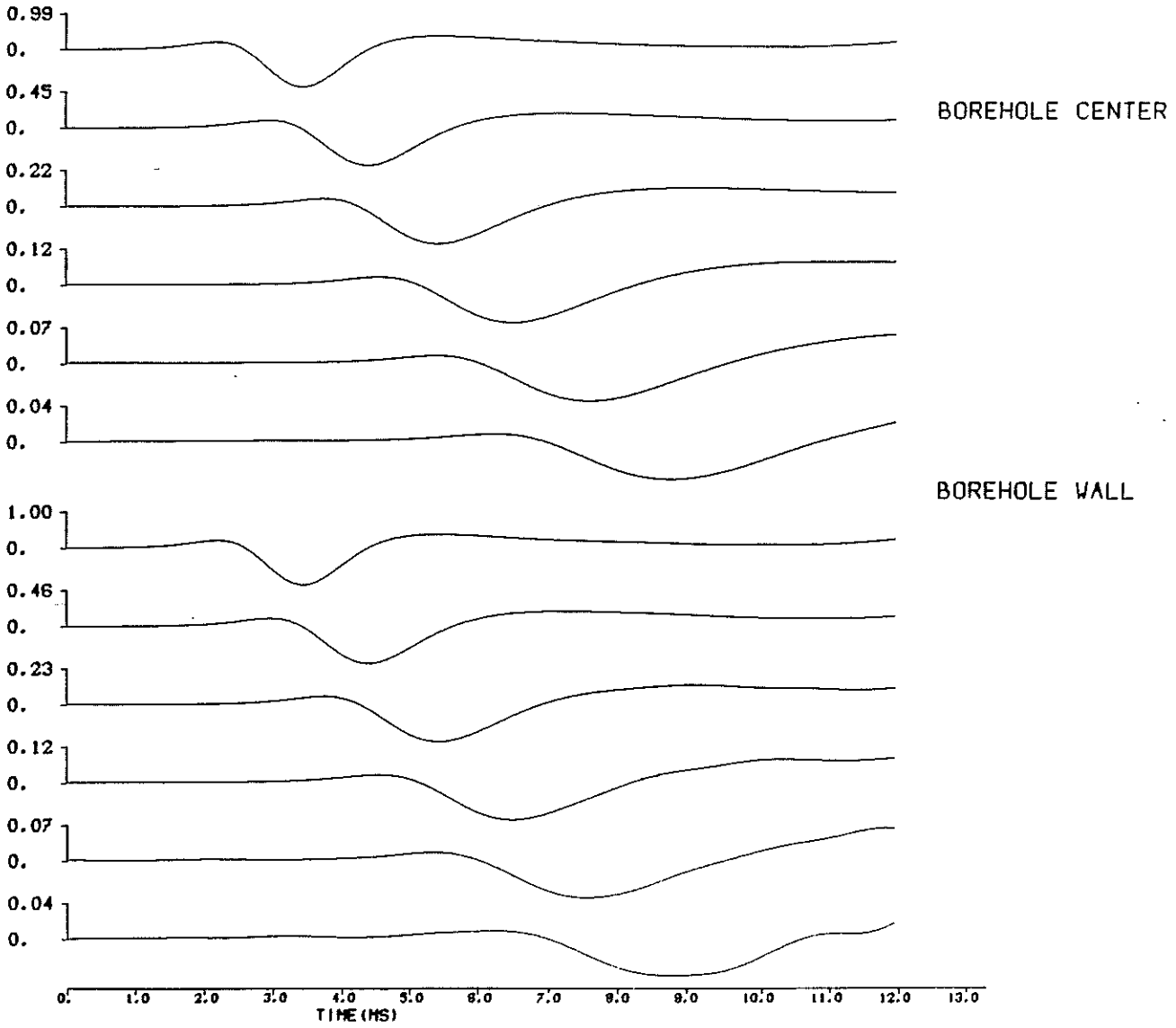

Figure 39: Same as Figure 38 with a source center frequency equal to 0.5 kHz.

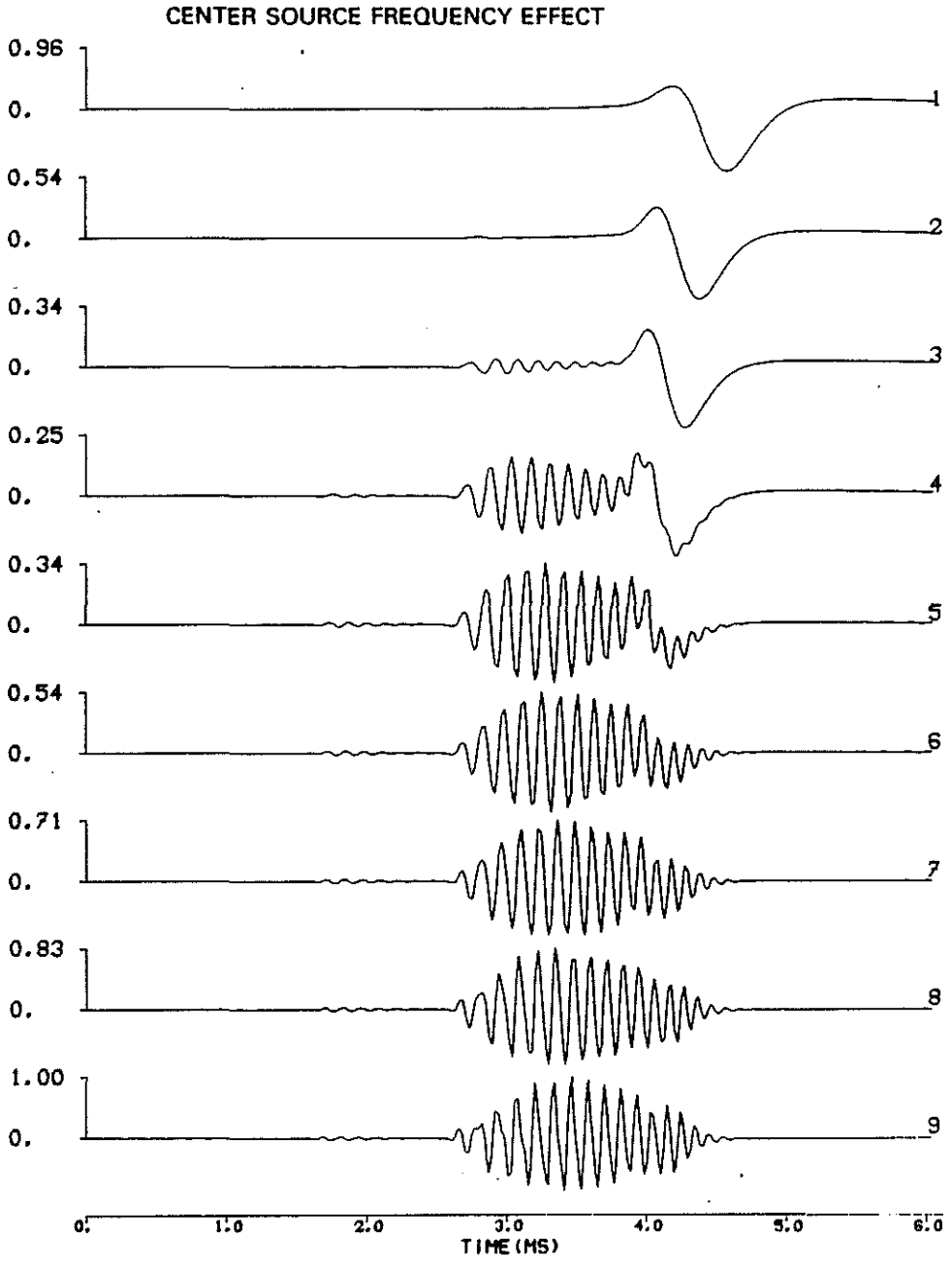

Figure 40 A: Permeable interface. Radius and source center frequency effects in the presence of gas saturated Berea sandstone ($\tilde{\phi} = 19\%$, $\tilde{k} = 2$md). The offset is equal to 5.25 m and the calculations are performed at the borehole center. R = 12 cm. The source center frequency varies in the range [1.5, 7.5] kHz by steps of 750 Hz from top of bottom. Each wavetrains is normalized with respect of its own maximum.

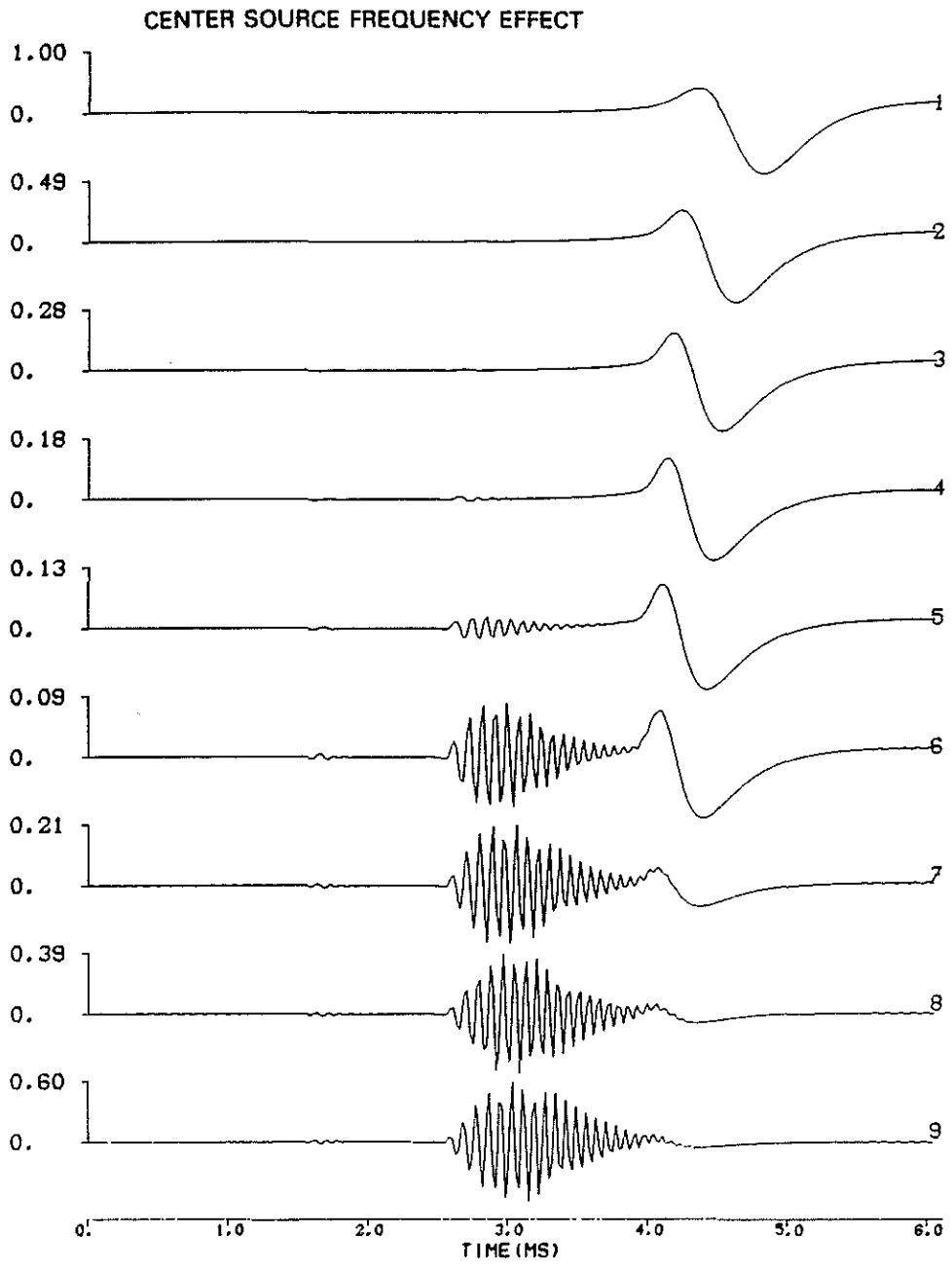

Figure 40 B: Same as Figure A with R = 7 cm.

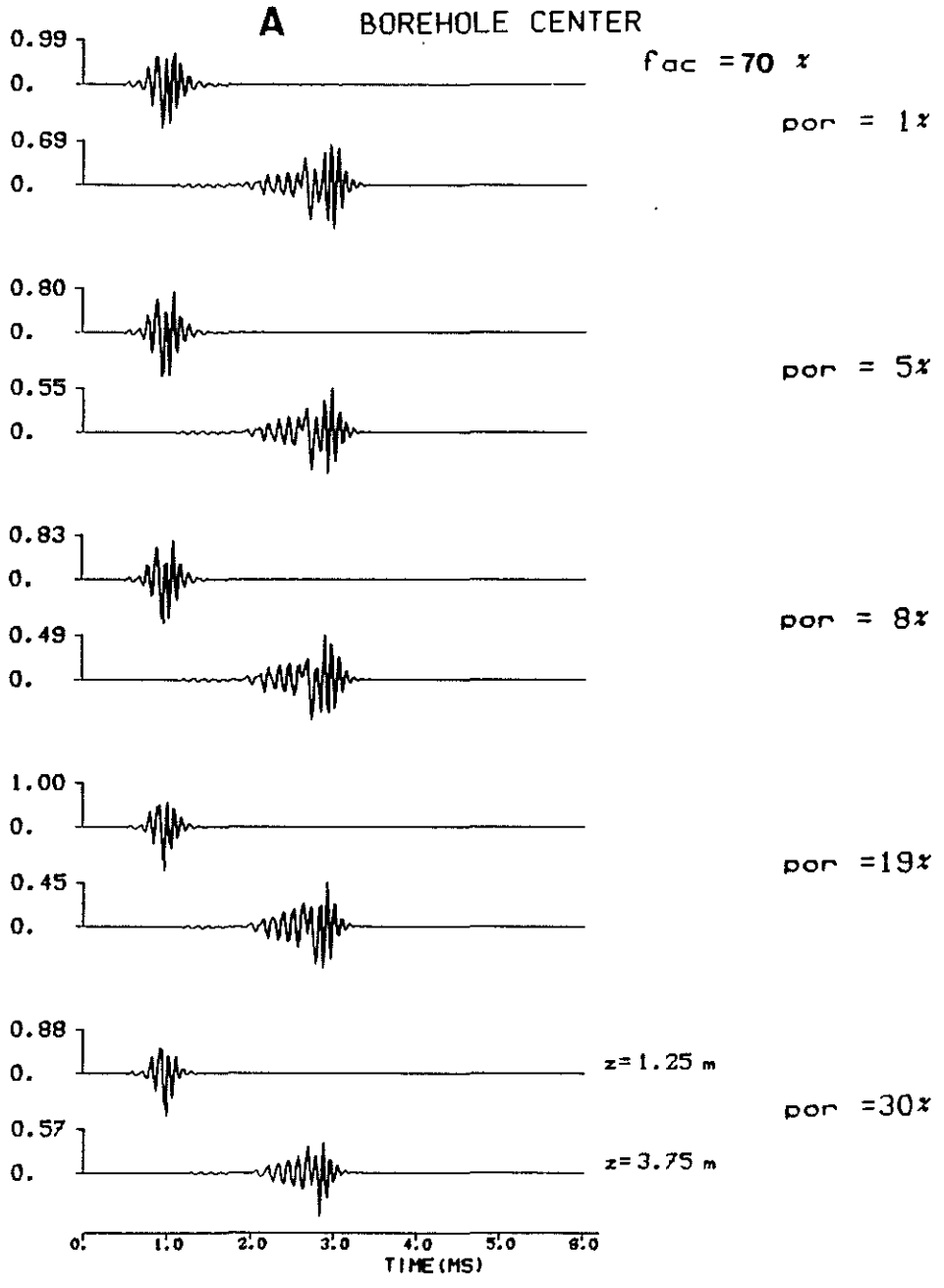

Figure 41 A: Permeable interface. Porosity effects in the presence of water saturated Berea sandstone ($\tilde{k}$ = 200 md, R = 12 cm). por denotes the porosity value. z is the offset. The source center frequency is equal to 7.5 kHz. r = 0 cm. The parameter fac denotes the relative value of the maximum of each series (indicated by 1.00) compared to a 19% equivalent elastic formation.

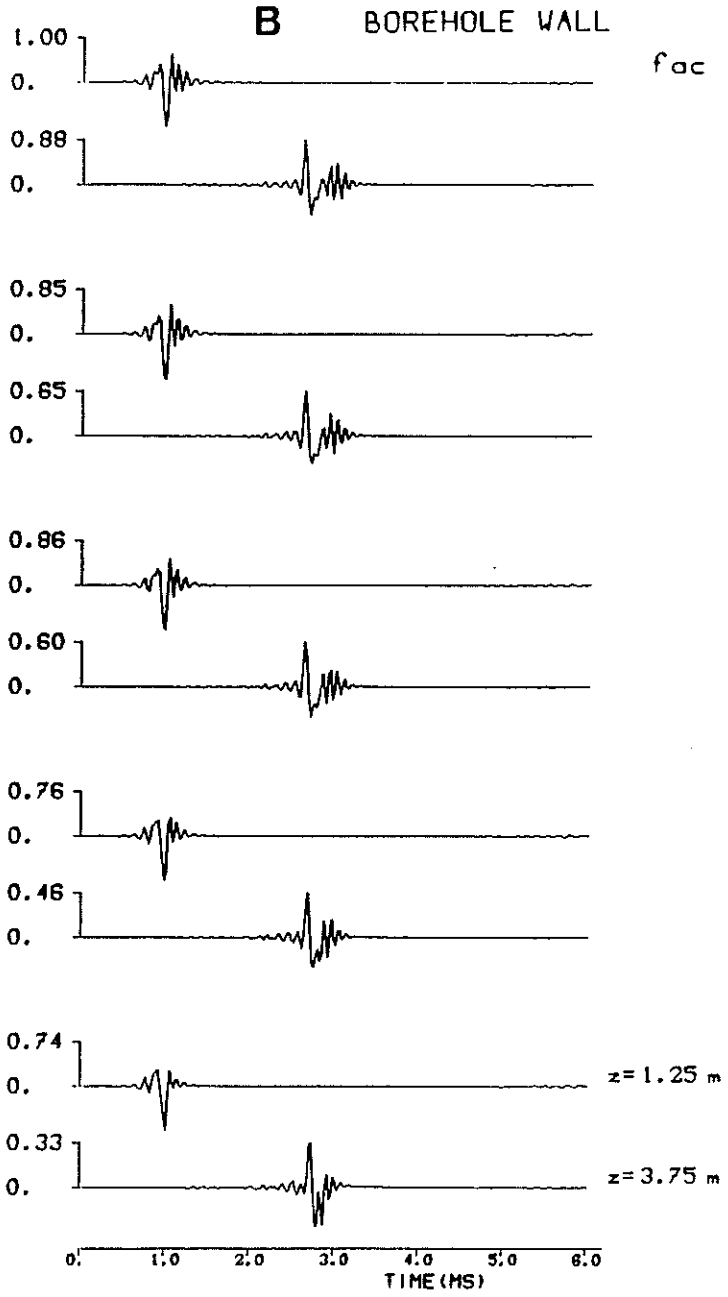

Figure 41 B: Same as Figure A at the borehole wall.

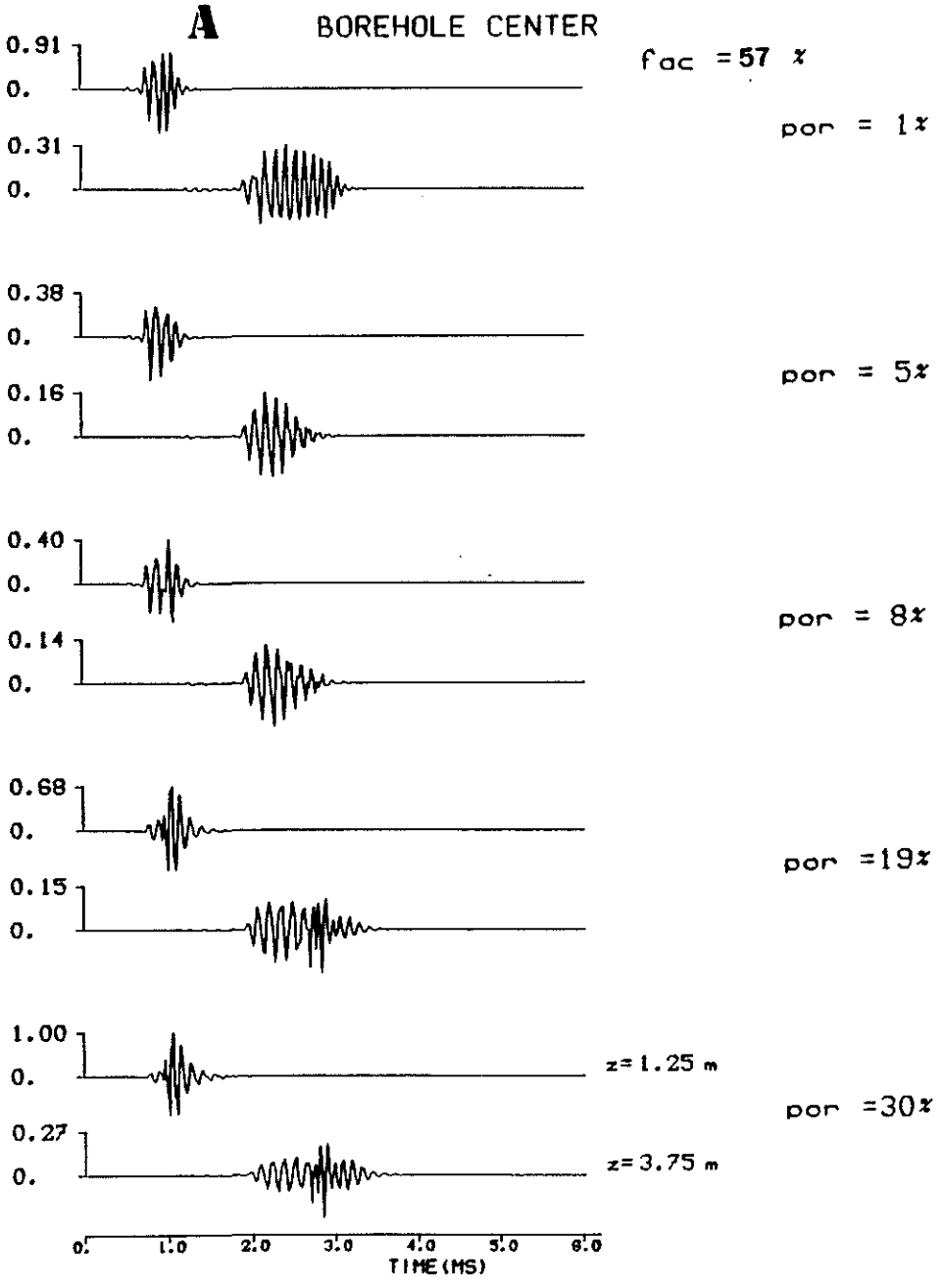

Figure 42: Same as Figure 41 A in the presence of gas saturated Berea sandstone.

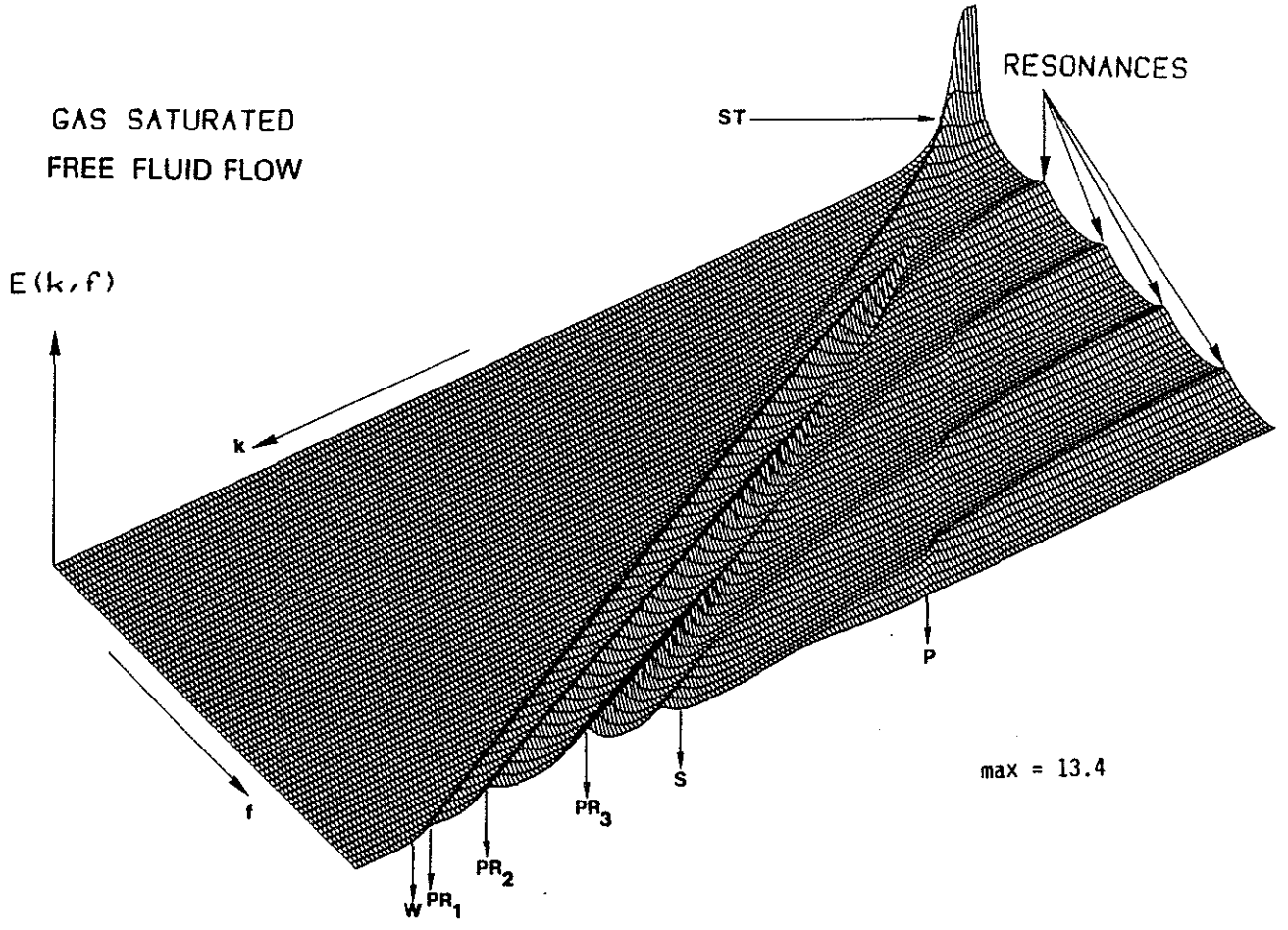

Figure 43: Permeable interface. Spectral energy density diagram obtained at the center of the borehole (R = 12 cm) in presence of gas saturated Berea sandstone ($\tilde{\phi}$ = 1%, $\tilde{k}$ = 200 md).

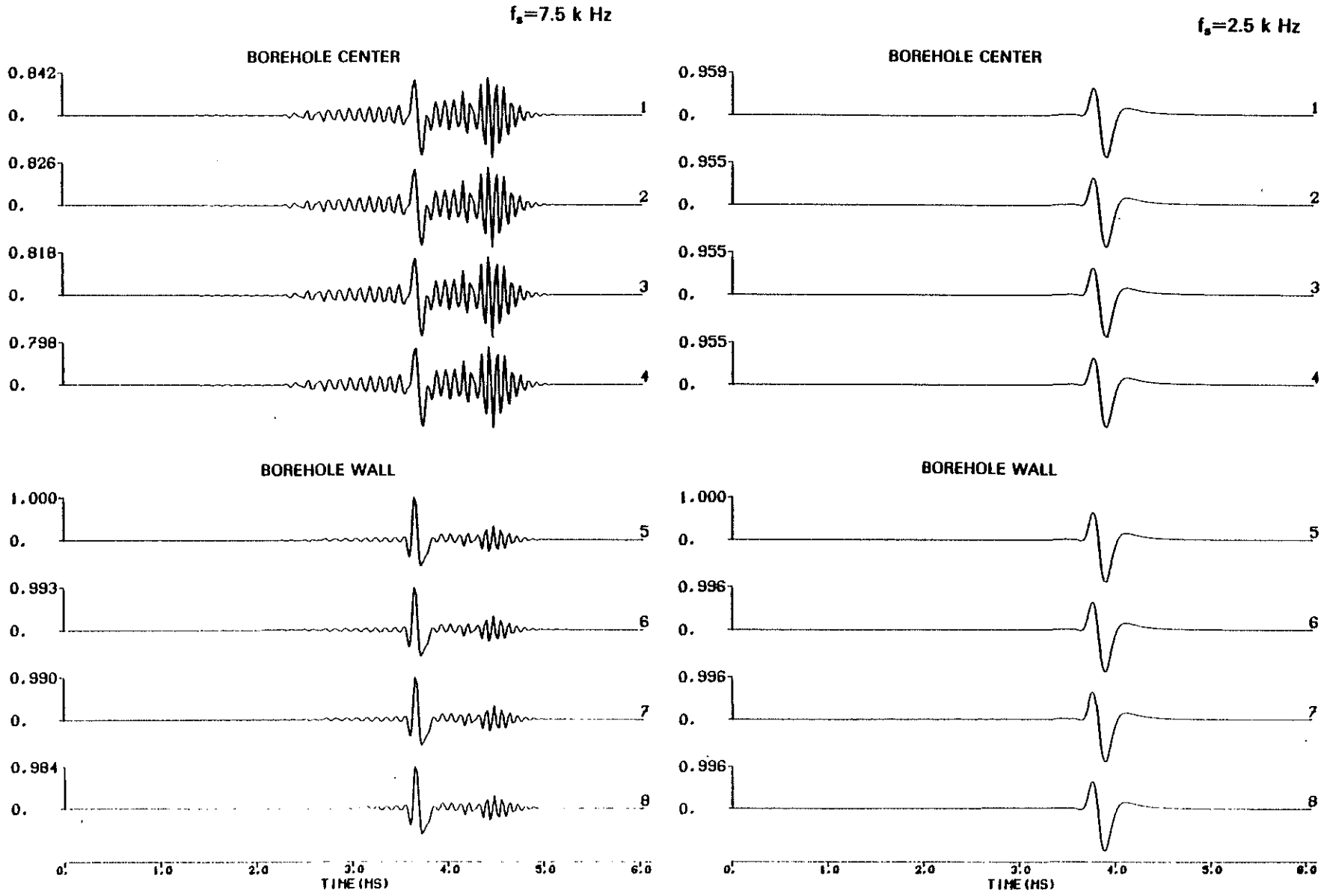

Figure 44: Impermeable interface. Permeability effects in the presence of water saturated Fox Hill sandstone ($\tilde{\phi}$ = 7.4%, R = 10 cm). Iso-offset (5.25 m) comparison of the synthetic microseismograms. f_s denotes the source center frequency. Each series is normalized with respect to its maximum (1.00). 1(5): Elastic, 2(6): $\tilde{k}$ = 1 md, 3(7): $\tilde{k}$ = 10 md, 4(8): $\tilde{k}$ = 32.5 md.

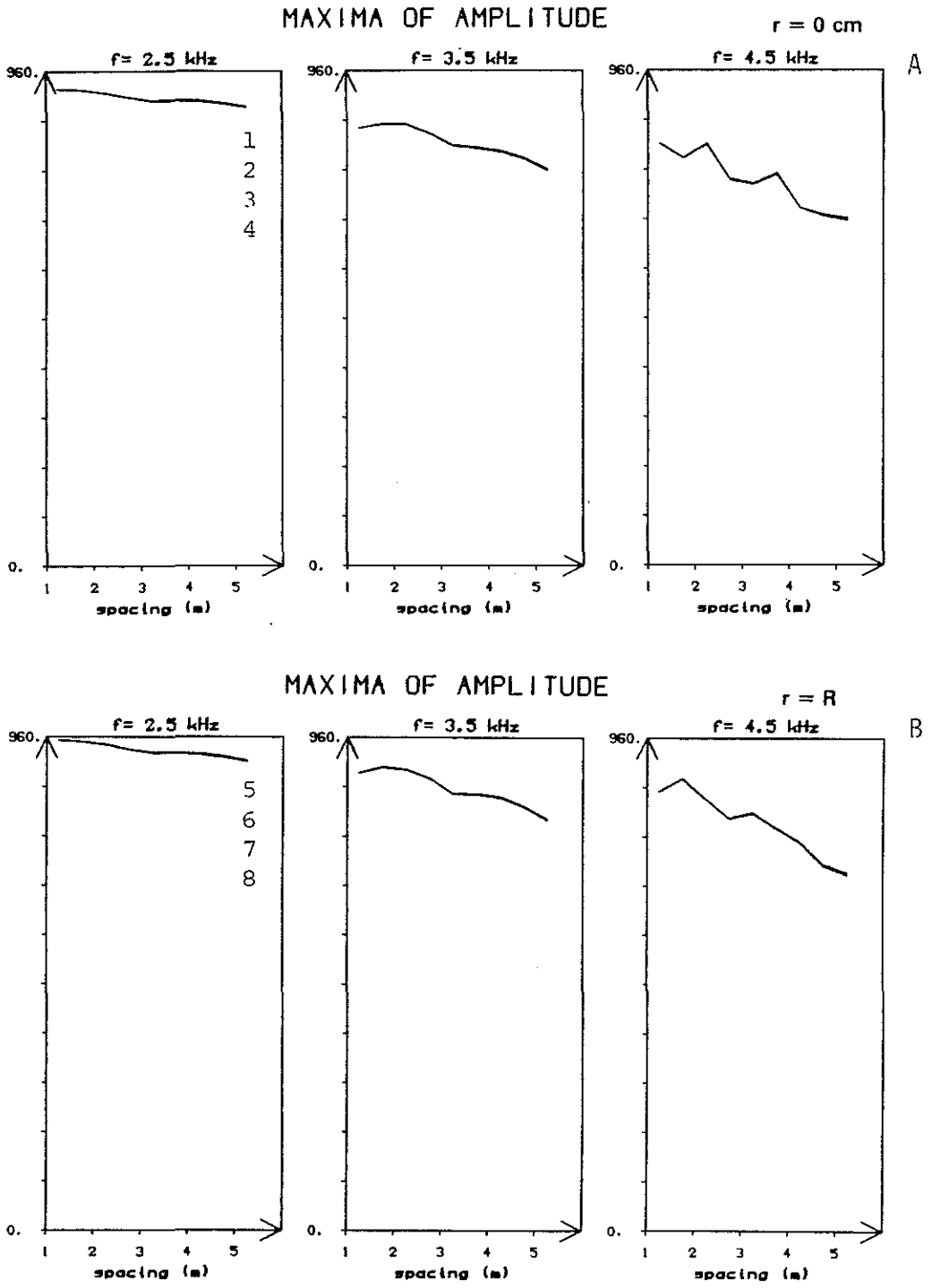

Figure 45: Variation of the maxima of amplitude as a function of the offset of the synthetic microseismograms relative to Figure 44. f denotes the source center frequency.1, 2, 3, 4, 5, 6, 7, 8 see Figure 44.

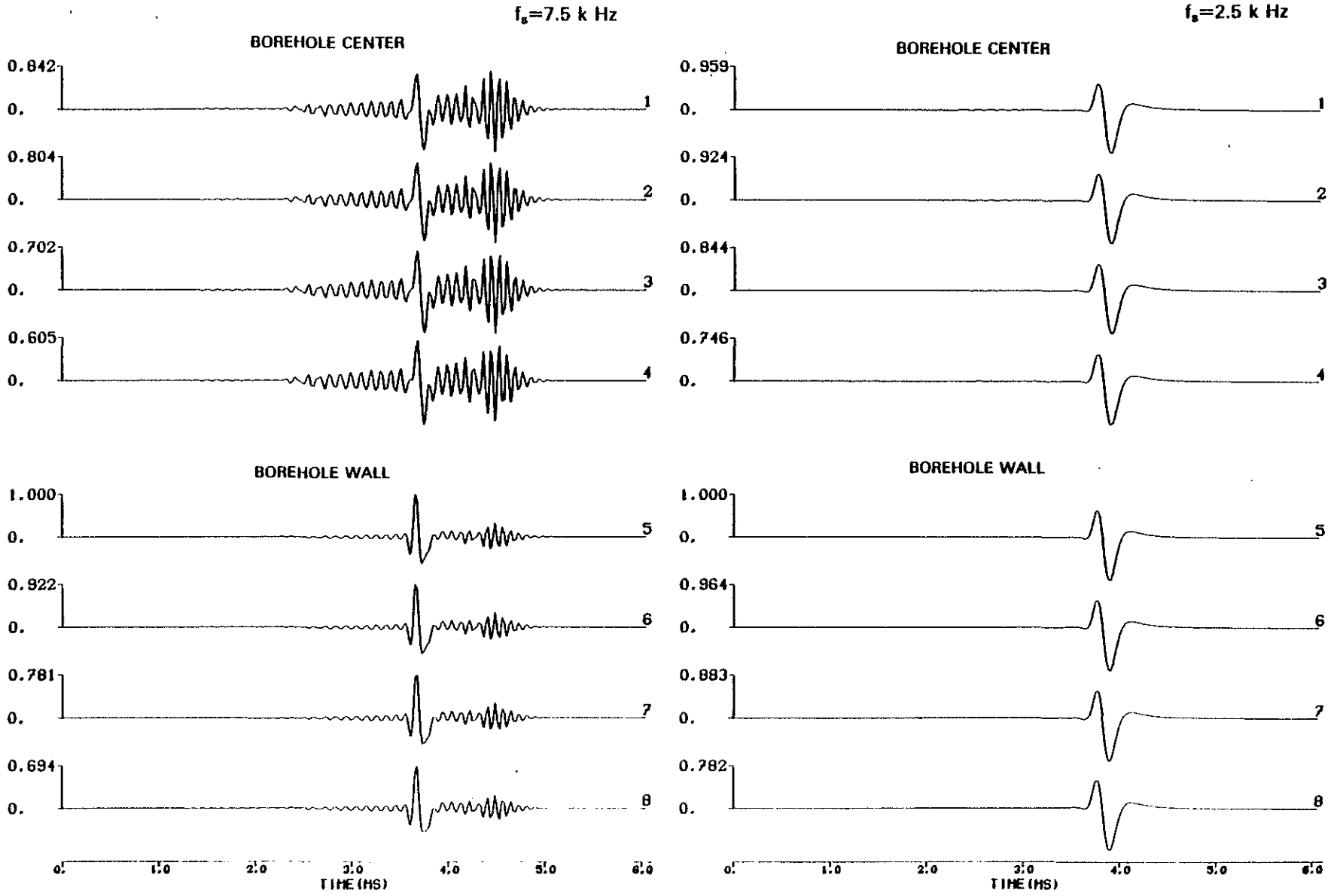

Figure 46: Permeable interface. Permeability effects in the presence of water saturated Fox Hill sandstone ($\tilde{\phi}$ = 7.4%, R = 10 cm). Iso-offset (5.25 m) comparison of the synthetic microseismograms. f_s denotes the source center frequency. Each series is normalized with respect to its maximum (1.00). 1(5): Elastic, 2(6): $\tilde{k}$ = 1 md, 3(7): $\tilde{k}$ = 10 md, 4(8): $\tilde{k}$ = 32.5 md.

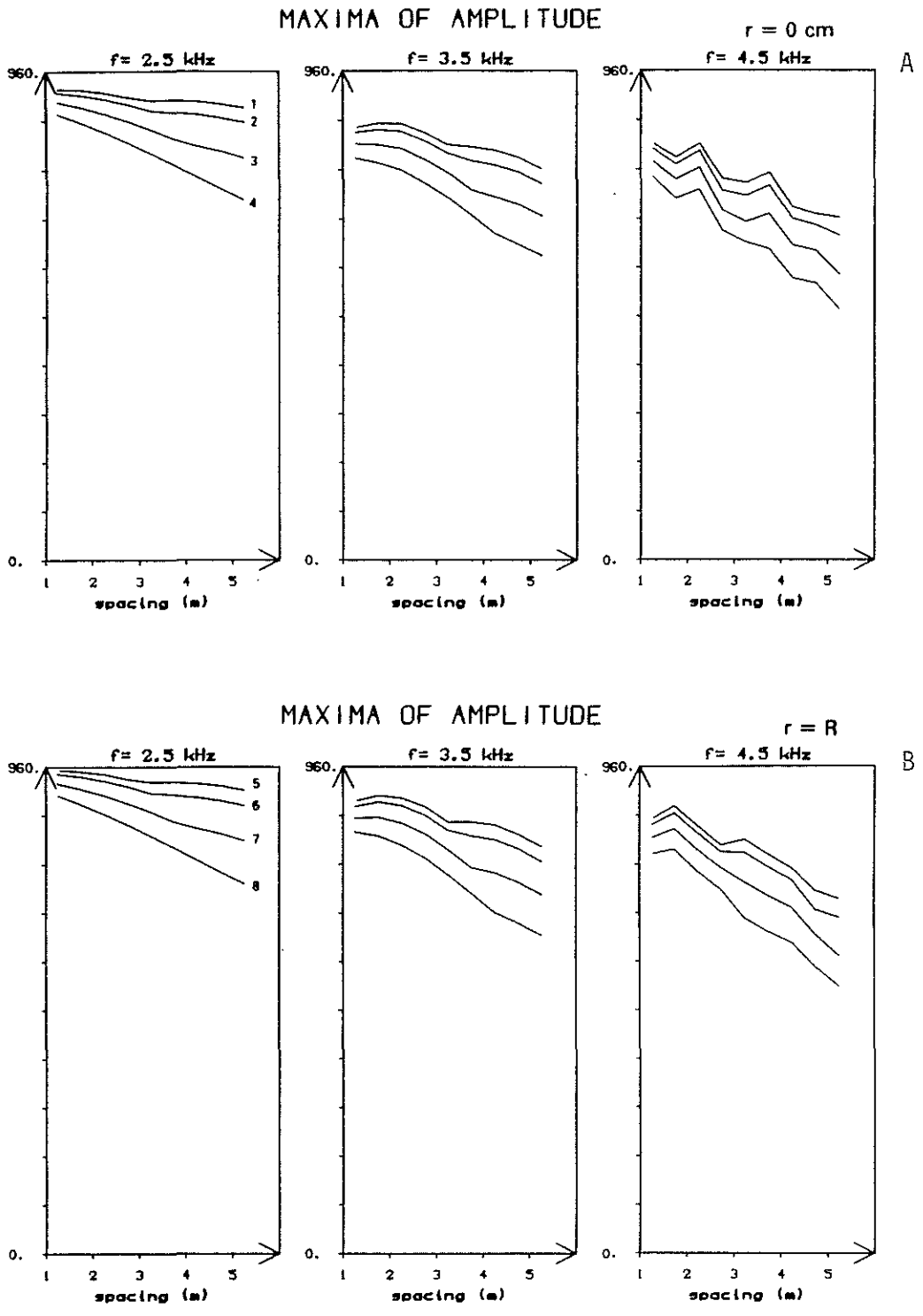

Figure 47: Variation of the maxima of amplitude as a function of the offset of the synthetic microseismograms relative to Figure 46. f denotes the source center frequency.1, 2, 3, 4, 5, 6, 7, 8 see Figure 46.

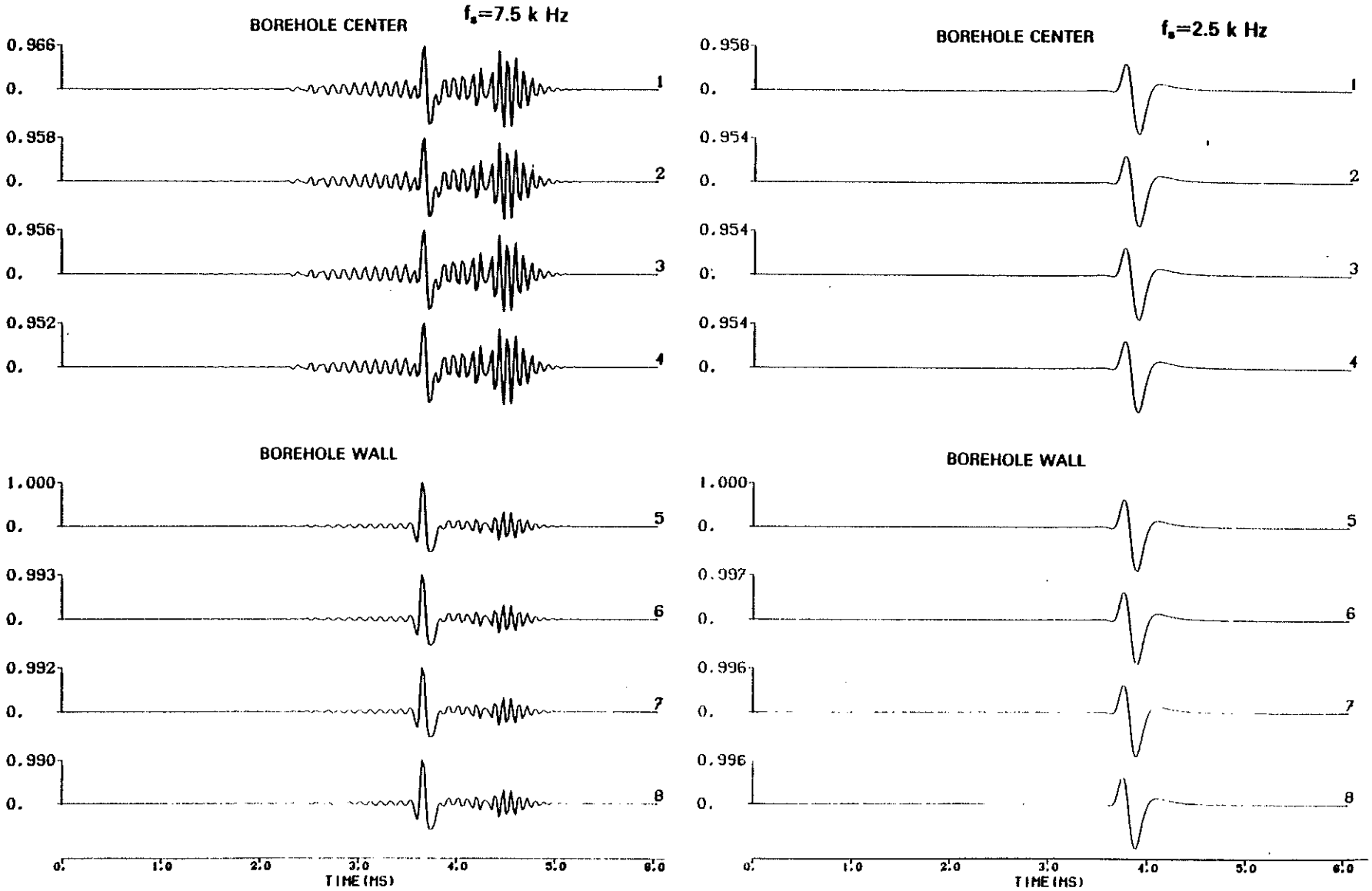

Figure 48: Impermeable interface. Permeability effects in the presence of gas saturated Fox Hill sandstone ($\tilde{\phi}$ = 7.4%, R = 10 cm). Iso-offset (5.25 m) comparison of the synthetic microseismograms. f_s denotes the source center frequency. Each series is normalized with respect to its maximum (1.00). 1(5): Elastic, 2(6): $\tilde{k}$ = 1 md, 3(7): $\tilde{k}$ = 10 md, 4(8): $\tilde{k}$ = 32.5 md.

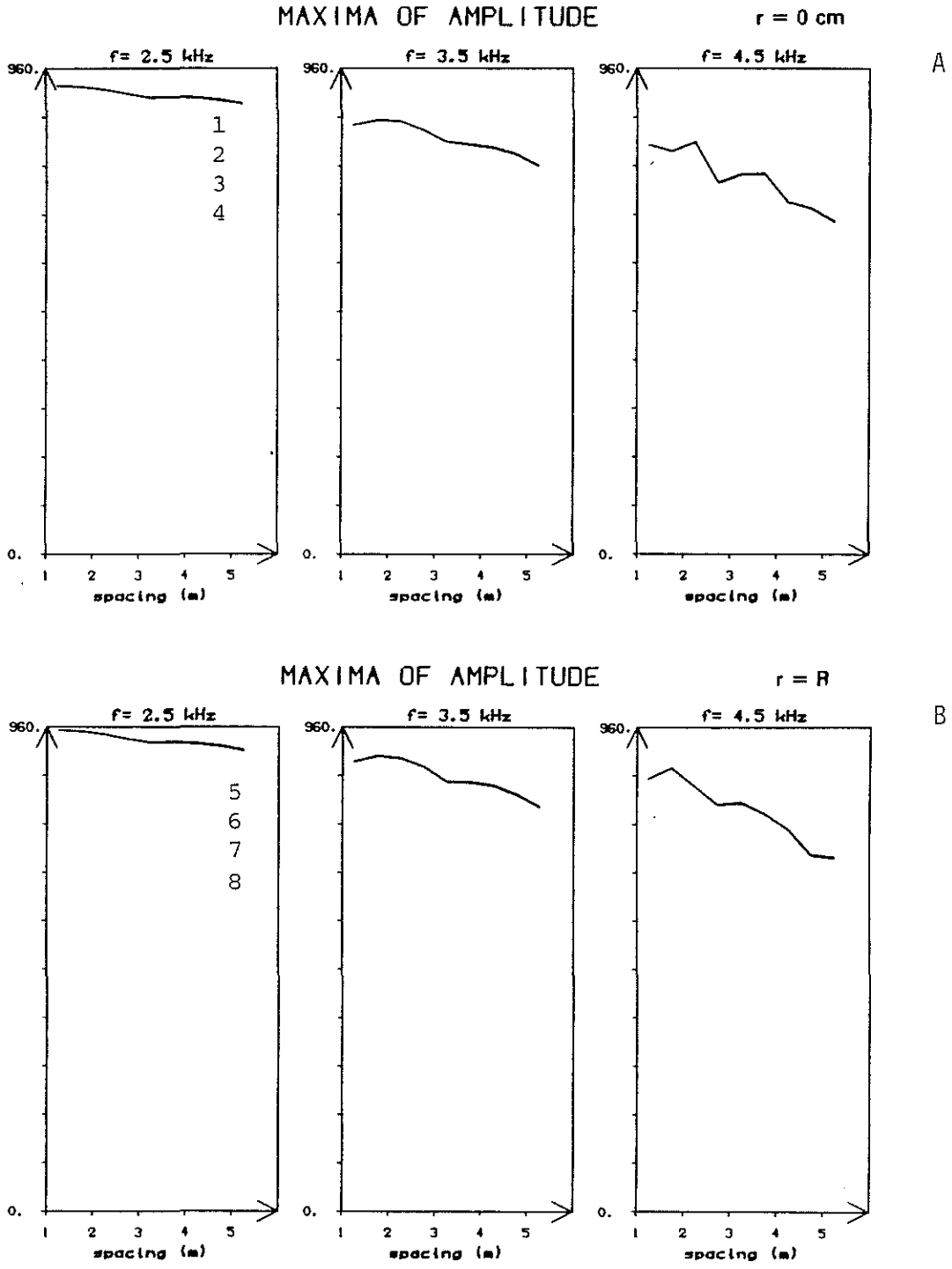

Figure 49: Variation of the maxima of amplitude as a function of the offset of the synthetic microseismograms relative to Figure 48. f denotes the source center frequency.1, 2, 3, 4, 5, 6, 7, 8 see Figure 48.

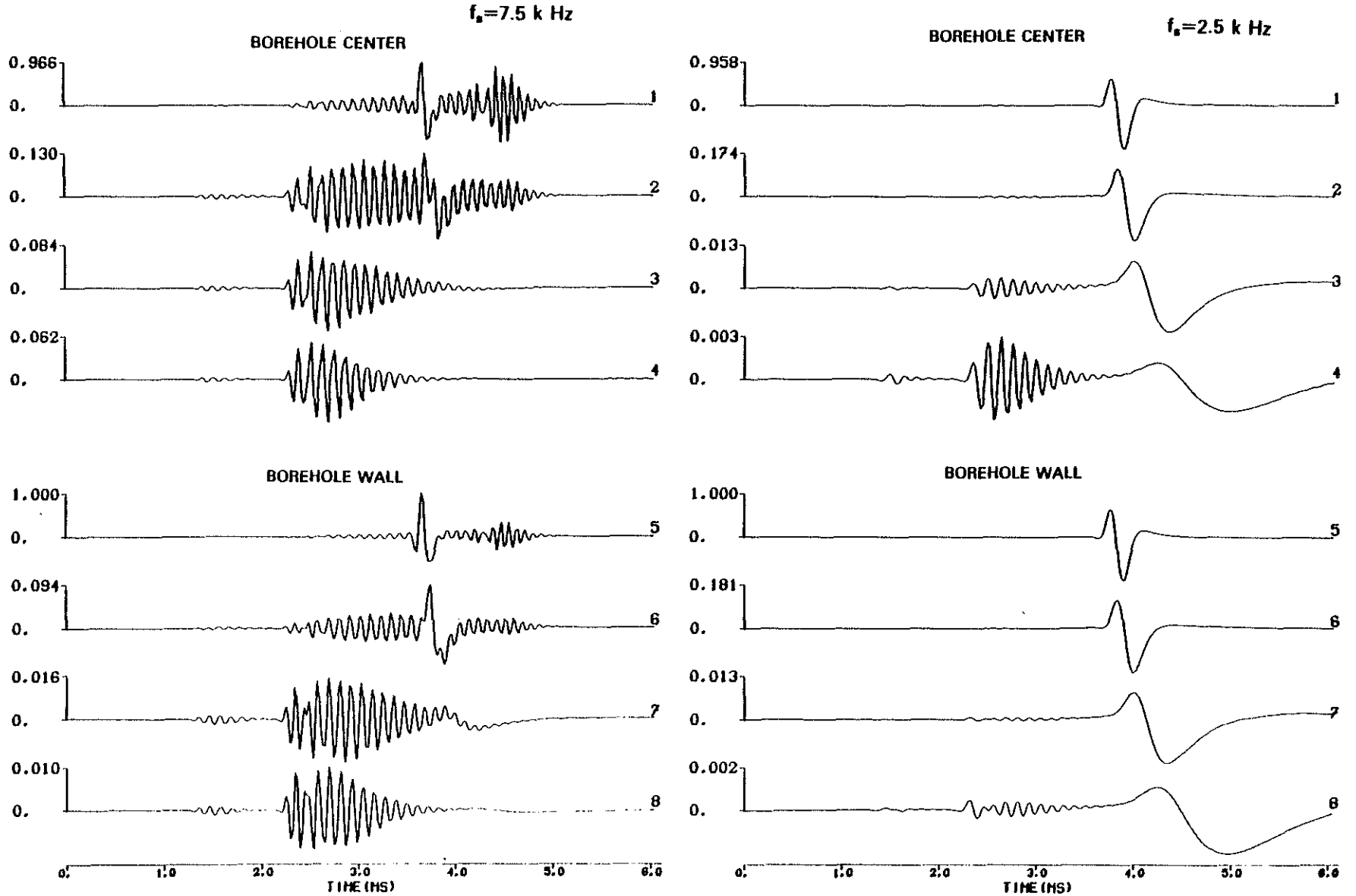

Figure 50: Permeable interface. Permeability effects in the presence of gas saturated Fox Hill sandstone ($\tilde{\phi} = 7.4\%$, R = 10 cm). Iso-offset (5.25 m) comparison of the synthetic microseismograms. f_s denotes the source center frequency. Each series is normalized with respect to its maximum (1.00). 1(5): Elastic, 2(6): $\tilde{k} = 1$ md, 3(7): $\tilde{k} = 10$ md, 4(8): $\tilde{k} = 32.5$ md.

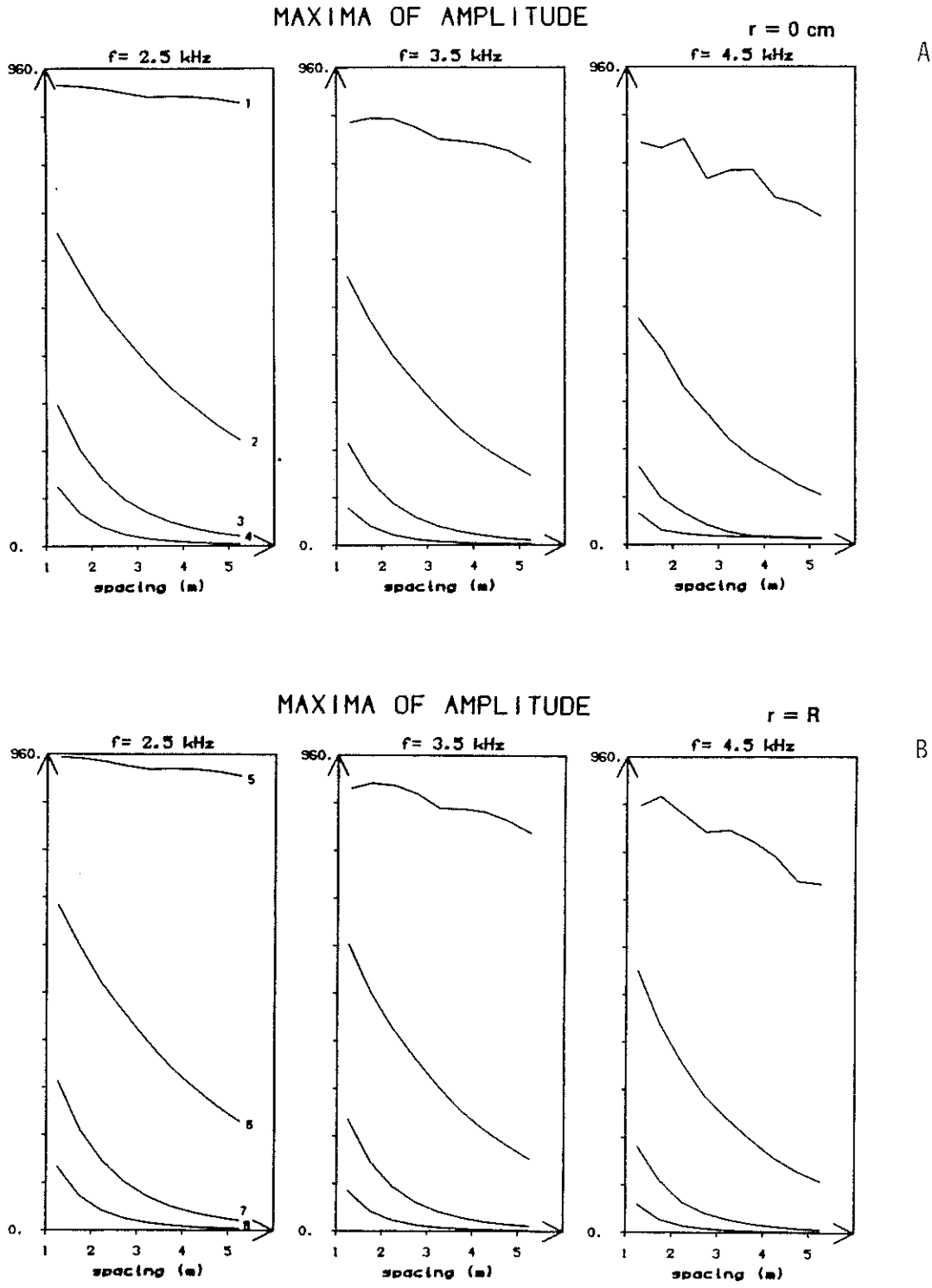

Figure 51: Variation of the maxima of amplitude as a function of the offset of the synthetic microseismograms relative to Figure 50. f denotes the source center frequency.1, 2, 3, 4, 5, 6, 7, 8 see Figure 50.

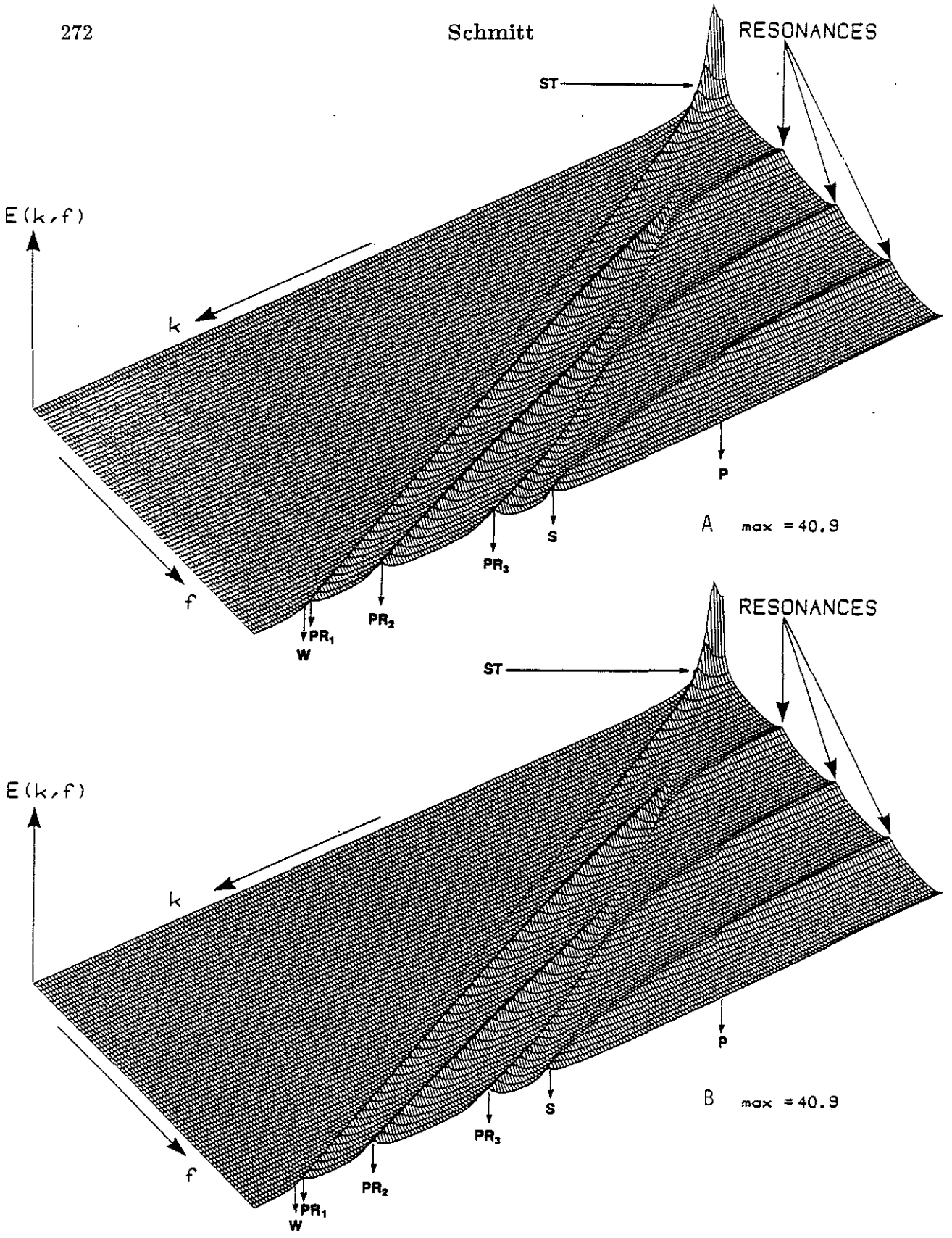

Figure 52: Fox Hill gas saturated formation ($\tilde{\phi} = 7.4\%$, $\tilde{k} = 32.5$ md). Spectral energy density diagrams obtained at the borehole center (R = 10 cm) in presence of the elastic formation (A), the porous formation when the borehole wall is impermeable (B), and when it is permeable (C). Each diagram is normalized with respect to its own maximum.

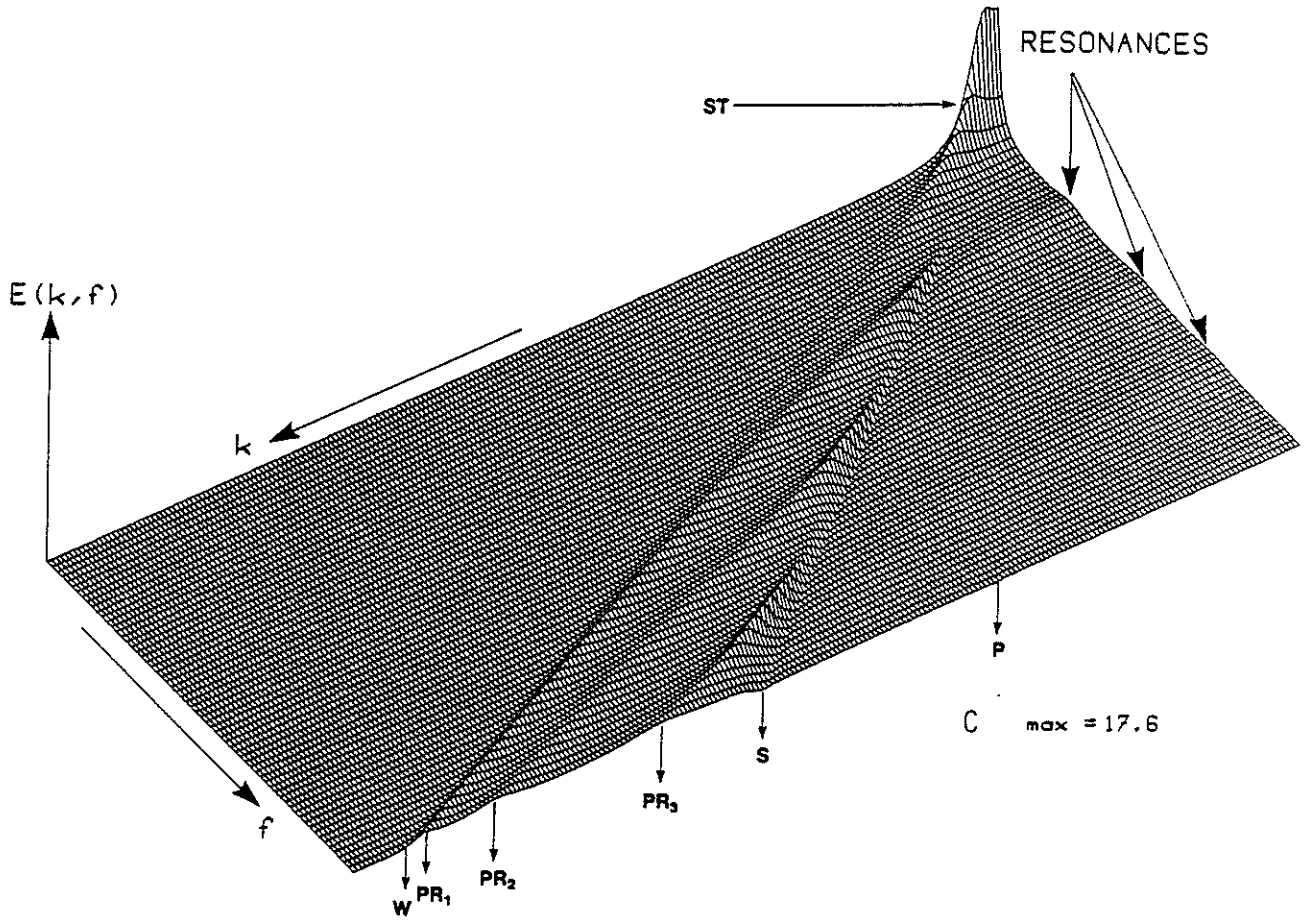
RESONANCES
ST
E(k,f)
k
f
P
C max = 17.6
S
PR3
PR2
PR1
W

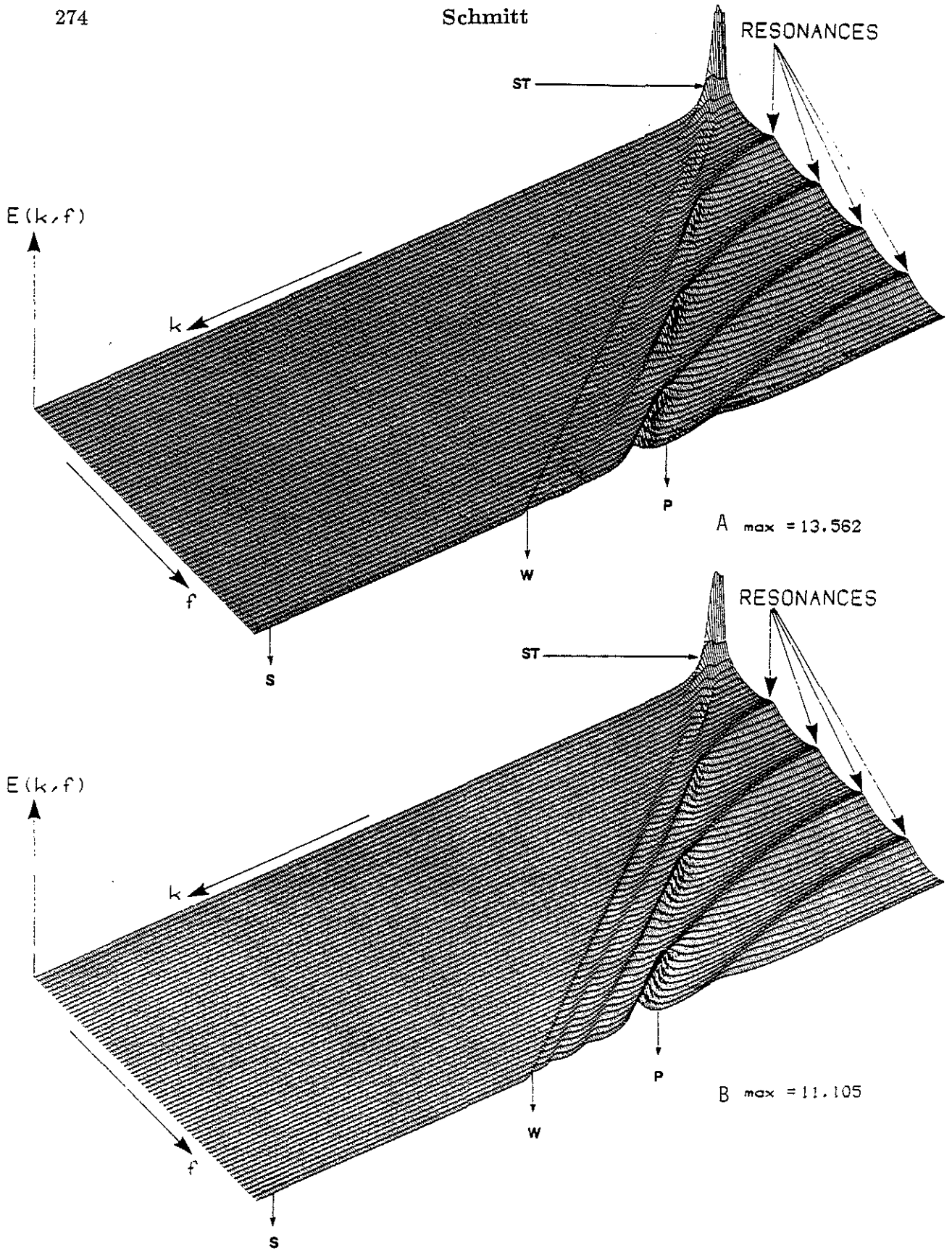

Figure 53: Water saturated slow formation ($\tilde{\phi} = 30\%$, $\tilde{k} = 1$ darcy). Spectral energy density diagrams obtained at the center of the borehole (R = 12 cm) in the presence of the elastic formation (A) and the porous formation when the fluid flow is free (B).

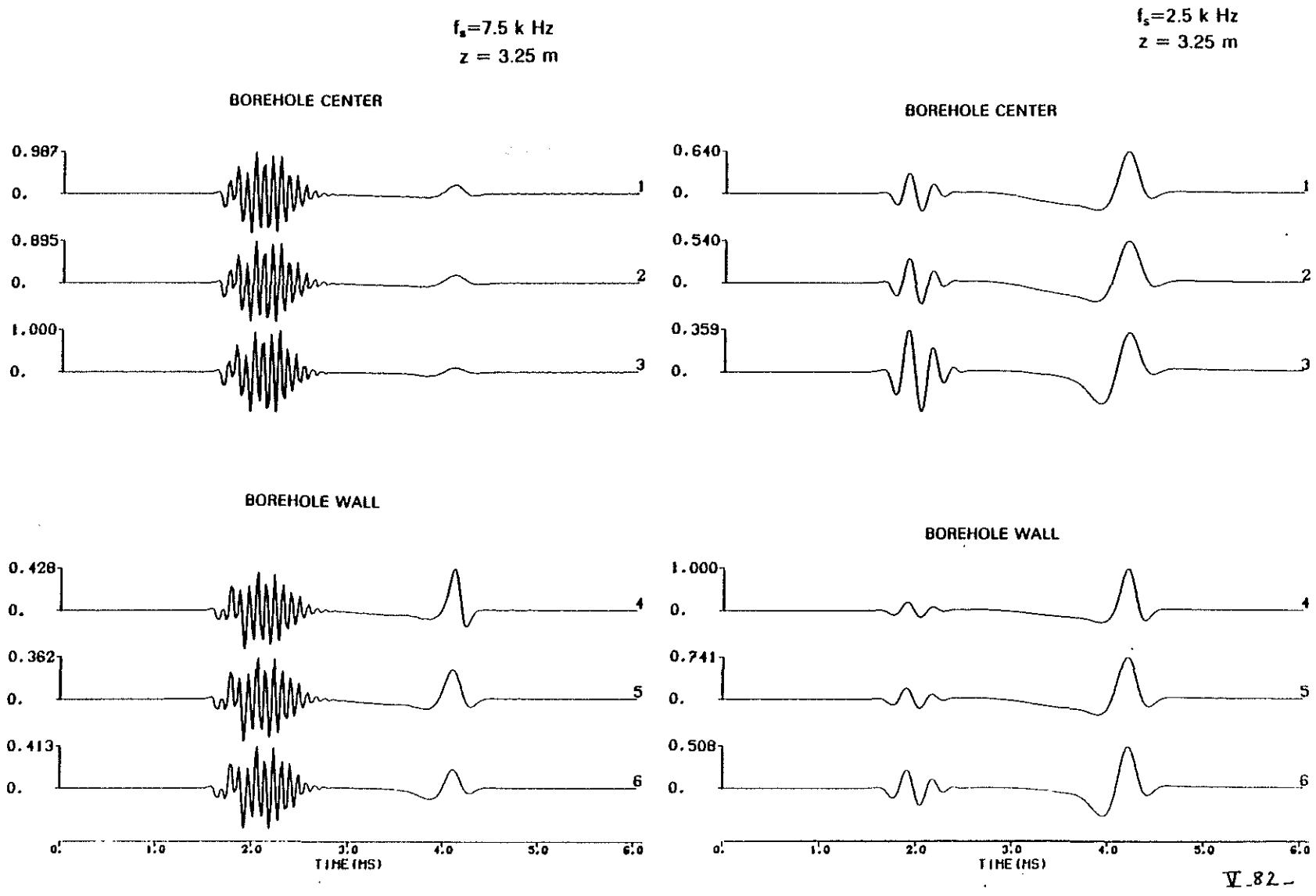

Figure 54: Water saturated slow formation ($\tilde{\phi}$ = 30%, $\tilde{k}$= 1 darcy). Iso-offset (3.25 m) comparison of the synthetic microseismograms obtained at the borehole center in the presence of the elastic formation (1(4)), the porous formation (2(5)) when the interface is impermeable, and when the fluid flow is free (3(6)). f_s denotes the source center frequency. Each series is normalized with respect to its own maximum (1.00).

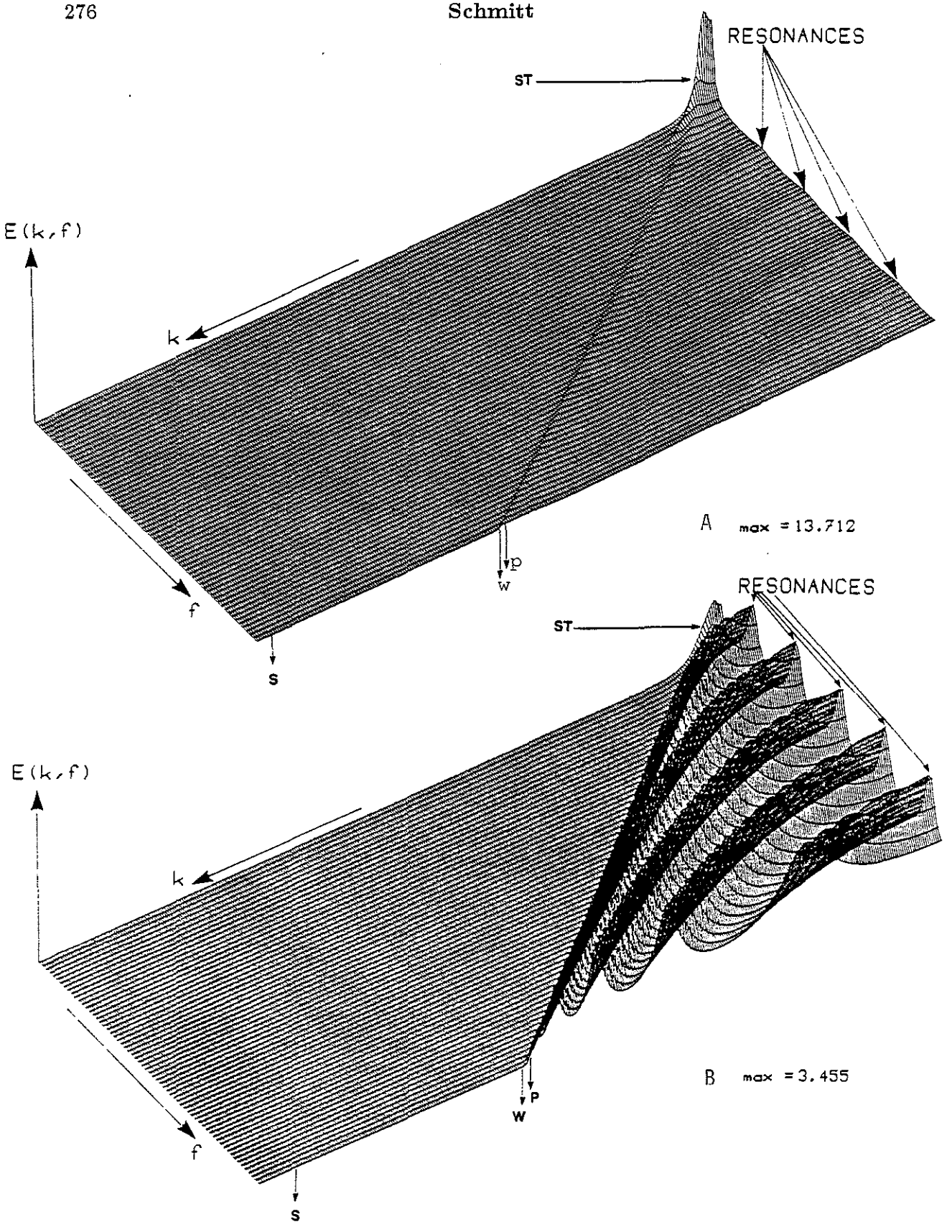

Figure 55: Gas saturated slow formation ($\tilde{\phi}$ = 30%, $\tilde{k}$ = 1 darcy). Spectral energy density diagrams obtained at the center of the borehole (R = 12 cm) in the presence of the elastic formation (A) and the porous formation when the fluid flow is free (B).

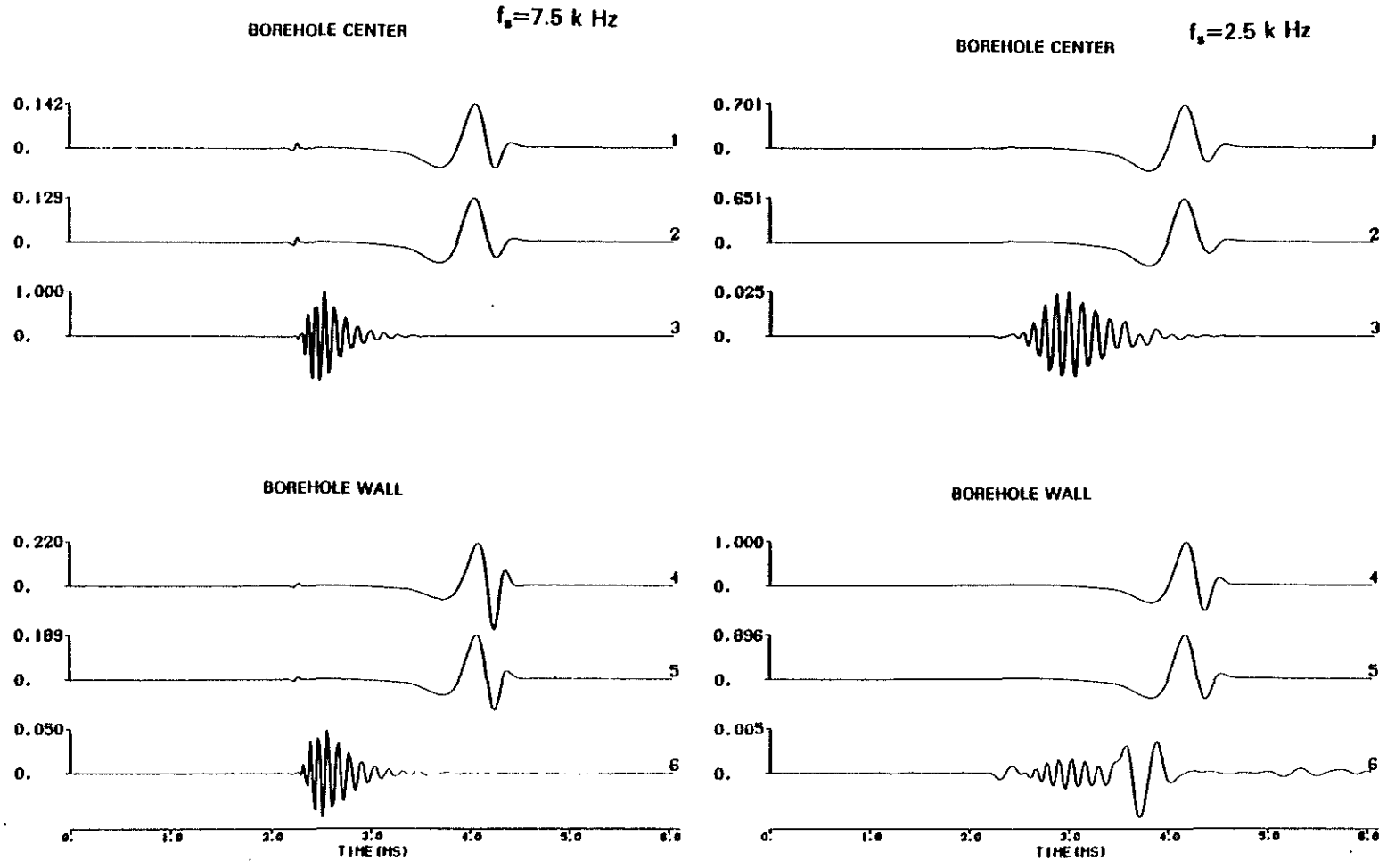

Figure 56: Gas saturated slow formation ($\tilde{\phi}$ = 30%, $\tilde{k}$= 1 darcy). Iso-offset (3.25 m) comparison of the synthetic microseismograms obtained at the borehole center in the presence of the elastic formation (1(4)), the porous formation (2(5)) when the interface is impermeable, and when the fluid flow is free (3(6)). f_s denotes the source center frequency. Each series is normalized with respect to its own maximum (1.00).

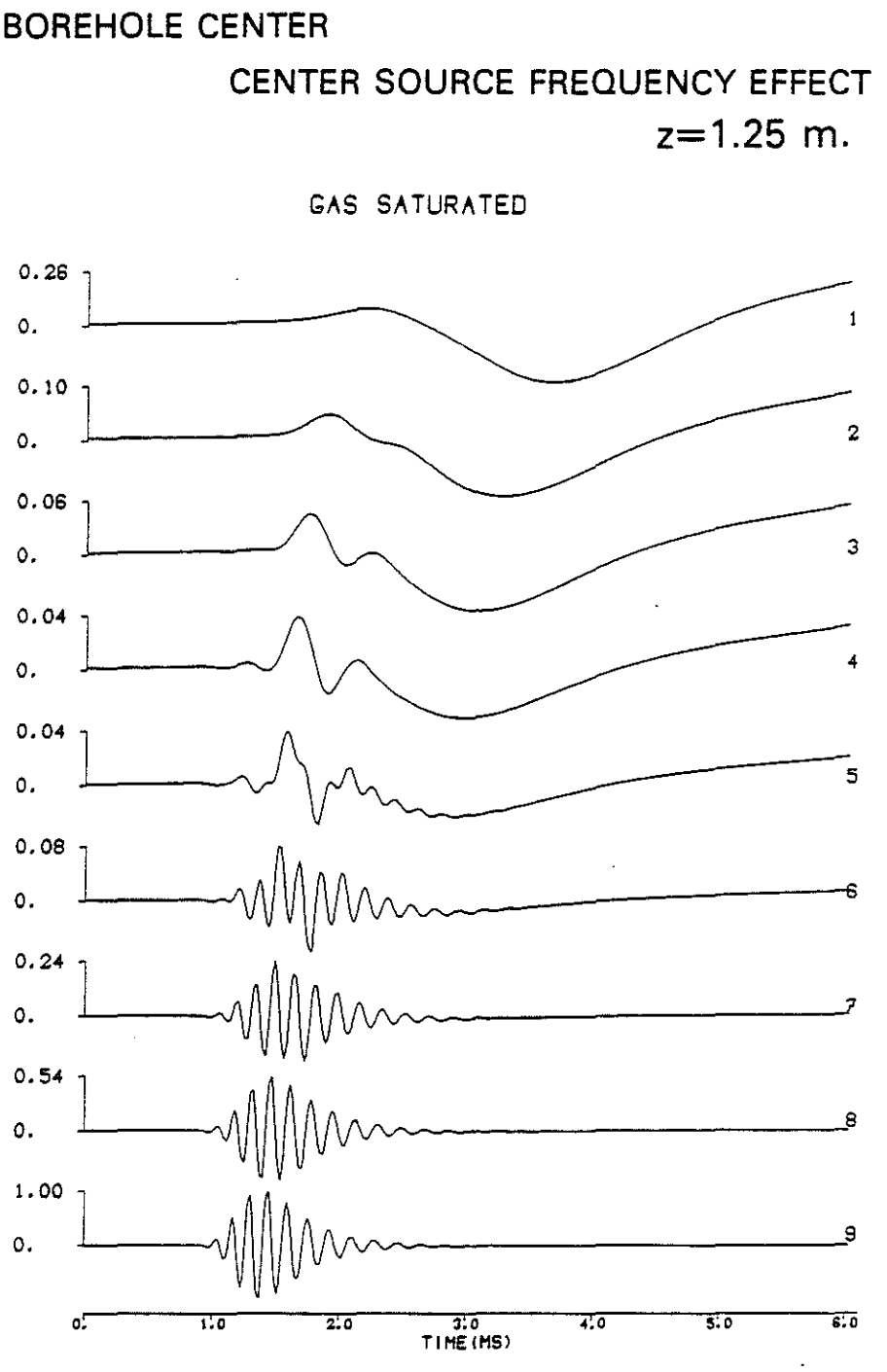

Figure 57: Permeable interface. Gas saturated slow formation ($\tilde{\phi} = 30\%$, $\tilde{k} = 1$ darcy, R = 12 cm). The source center frequency varies in the range [0.7, 3.5] kHz by steps of 350 Hz from top to bottom of the figure. z = 1.25 m. Borehole center. Each waveform is normalized with respect to its own maximum.